A LIQUID-HELIUM-FREE HIGH-STABILITY CRYOGENIC SCANNING TUNNELING MICROSCOPE FOR ATOMIC-SCALE SPECTROSCOPY

by

JASON DOUGLAS HACKLEY

A DISSERTATION

Presented to the Department of Chemistry and Biochemistry
and the Graduate School of the University of Oregon
in partial fulfillment of the requirements
for the degree of
Doctor of Philosophy

March 2015

DISSERTATION APPROVAL PAGE

Student: Jason Douglas Hackley

Title: A Liquid-helium-free High-stability Cryogenic Scanning Tunneling Microscope for Atomic-scale Spectroscopy

This dissertation has been accepted and approved in partial fulfillment of the requirements for the Doctor of Philosophy degree in the Department of Chemistry and Biochemistry by:

Andy H. Marcus	Chairperson
George V. Nazin	Advisor
Jeffrey A. Cina	Core Member
Stephen Gregory	Institutional Representative

and

J. Andrew Berglund	Dean of the Graduate School

Original approval signatures are on file with the University of Oregon Graduate School.

Degree awarded March 2015

DISSERTATION ABSTRACT

Jason Douglas Hackley

Doctor of Philosophy

Department of Chemistry and Biochemistry

March 2015

Title: A Liquid-helium-free High-stability Cryogenic Scanning Tunneling Microscope for Atomic-scale Spectroscopy

This dissertation provides a brief introduction into scanning tunneling microscopy, and then Chapter III reports on the design and operation of a cryogenic ultra-high vacuum scanning tunneling microscope (STM) coupled to a closed-cycle cryostat (CCC). The STM is thermally linked to the CCC through helium exchange gas confined inside a volume enclosed by highly flexible rubber bellows. The STM is thus mechanically decoupled from the CCC, which results in a significant reduction of the mechanical noise transferred from the CCC to the STM. Noise analysis of the tunneling current shows current fluctuations up to 4% of the total current, which translates into tip-sample distance variations of up to 1.5 picometers. This noise level is sufficiently low for atomic-resolution imaging of a wide variety of surfaces. To demonstrate this, atomic-resolution images of Au(111) and NaCl(100)/Au(111) surfaces, as well as of carbon nanotubes deposited on Au(111), were obtained. Other performance characteristics such as thermal drift analysis and a cool-down analysis are reported. Scanning

tunneling spectroscopy (STS) measurements based on the lock-in technique were also carried out and showed no detectable presence of noise from the CCC. These results demonstrate that the constructed CCC-coupled STM is a highly stable instrument capable of highly detailed spectroscopic investigations of materials and surfaces at the atomic-scale.

A study of electron transport in single-walled carbon nanotubes (SWCNTs) was also conducted. In Chapter IV, STS is used to study the quantum-confined electronic states in SWCNTs deposited on the Au(111) surface. The STS spectra show the vibrational overtones which suggest rippling distortion and dimerization of carbon atoms on the SWCNT surface. This study experimentally connects the properties of well-defined localized electronic states to the properties of their associated vibronic states.

In Chapter V, a study of PbS nanocrystals was conducted to study the effect of localized sub-bandgap states associated with surface imperfections. A correlation between their properties and the atomic-scale structure of chemical imperfections responsible for their appearance was established to understand the nature of such surface states.

This dissertation includes previously published and co-authored material.

CURRICULUM VITAE

NAME OF AUTHOR: Jason Douglas Hackley

GRADUATE AND UNDERGRADUATE SCHOOLS ATTENDED:

University of Oregon, Eugene
University of California, Irvine

DEGREES AWARDED:

Doctor of Philosophy, Chemistry, 2015, University of Oregon
Bachelor of Science, Chemical Engineering, 2009, University of California, Irvine
Bachelor of Science, Chemistry, 2009, University of California, Irvine

AREAS OF SPECIAL INTEREST:

Ultra-high Vacuum
Scanning Tunneling Microscopy
Closed-cycle Cryostat
Surface Science

PROFESSIONAL EXPERIENCE:

Graduate Research Assistant, Department of Chemistry and Biochemistry, University of Oregon, Eugene, OR, 2010-2015

Graduate Teaching Assistant, Department of Chemistry and Biochemistry, University of Oregon, Eugene, OR, 2009-2010, 2013-2015

PUBLICATIONS:

Hackley, J. D., Kislitsyn, D. A., Beaman, D. K., Ulrich, S. & Nazin, G. V. High-stability cryogenic scanning tunneling microscope based on a closed-cycle cryostat. *Rev. Sci. Instrum.* **85,** 103704 (2014).

Kislitsyn, D. A., Hackley, J. D. & Nazin, G. V. Vibrational Excitation in Electron Transport through Carbon Nanotube Quantum Dots. *J. Phys. Chem. Lett.* **5,** 3138–3143 (2014).

Kislitsyn, D. A., Gervasi, C. F., Allen, T., Palomaki, P. K. B., Hackley, J. D., Maruyama, R., Nazin, G. V. Spatial Mapping of Sub-Bandgap States Induced by Local Nonstoichiometry in Individual Lead Sulfide Nanocrystals. *J. Phys. Chem. Lett.* 3701–3707 (2014).

ACKNOWLEDGMENTS

I would first and foremost like to thank my parents for raising me to be who I am, loving me through the best and worst of times, never giving up on me, and always encouraging me to work hard and do good things. I love you mom and dad! Nor would I be who I am without my siblings and extended family; thank you for your unconditional love and companionship over all the years. I would also like to thank my boss, Dr. George Nazin, for his wealth of patience and for allowing me to be part of this amazing and one-of-a-kind project. Thank you to my committee members for believing in me and giving me the opportunity to continue. It has also been a pleasure to work alongside Dmitry Kislitsyn, who, most thankfully, among other good qualities, was our resident coding guru. Big thanks to Dr. Daniel Beaman for his help in designing and fabricating critical components of the project. The guys in our machine shop (Kris Johnson, John Boosinger, Jeffrey Garman, and the ever-entertaining mad-genius David Senkovich) were a tremendous help; without their expertise, I can't imagine how much longer the project would have taken to complete. Let me not forget to mention our electronics expert, Cliff Dax, who probably saved my life at least once (literally!), and gave us much insight and instruction on proper instrument setup/wiring.

I would also like to thank the University of Oregon for their support over the last 5 and a half years. Go Ducks!

This investigation and construction of the CCC UHV STM was supported in part by the U.S. National Science Foundation under Grant No. DMR-0960211, along with funding provided by the Oregon Nanoscience and Micro-technologies Institute under Grant No. 16716. With funding on collaborative projects coming from Sony Corporation, and Voxtel Nano.

Finally, and most importantly, thank you to my amazing and beautiful wife for her constant encouragement and love, my two fun-loving children who always brought me back to reality, and my Lord and Savior Jesus Christ for equipping me and sustaining me through it all!

This work is dedicated to my loving wife and our two little blessings.

"And I set my mind to seek and explore by wisdom concerning all that has been done under heaven" (Ecclesiastes 1:13, NASB).

TABLE OF CONTENTS

Chapter Page

LIST OF FIGURES

CHAPTER I

INTRODUCTION

1.1. Background

More than forty years ago, Binnig and Rohrer invented the scanning tunneling microscope (STM) in a 27-month period while at IBM and published their first papers in 1982.[1–4] Since then, the STM has proven to be an invaluable tool in nanoscience as it allows the investigator an unprecedented glimpse of an atom, molecule, nanoparticle, surface, or defect site—to probe local phenomena at the nanoscale. Scanning tunneling microscopy is an art-form that allows one to reach out and "touch" atoms.[5]

The STM is regularly used to perform surface topography scans (in constant current, or constant height modes) to reveal the real-space structure of a material,[6] scanning tunneling spectroscopy (STS, measurements which obtain current vs. voltage spectra, I/V, or also differential conductance spectra, dI/dV) to measure the local density of states (LDOS) [REF???], and second-order differential conductance (d^2I/dV^2) for inelastic electron tunneling spectroscopy (IETS) to measure vibrational spectra of adsorbates.[7,8] As discussed in a recent review, the STM has matured since its inception and is now routinely used to measure spatially resolved electromagnetic properties, atomically resolve

surface chemistry, perform high-resolution optical microscopy and spectroscopy, and visualize spatial structure in electronic, magnetic, and bosonic materials.[9]

Typically, high-performance STMs are operated at cryogenic temperatures in an ultra-high vacuum (UHV) environment, although, STMs may also achieve quality results in ambient conditions, as well as in gaseous[10] or liquid[11] environments, with experiments ranging from a few tens of mK[12,13] to nearly 1000 K.[14] The aforementioned qualities make the STM well-suited for use in a variety of research fields, especially those areas involved in nanotechnology.[9]

The STM can obtain atomic resolution images when its tip (commonly W, Pt-Ir, or Ag in our case) comes into close proximity (usually 5 to 10 Angstroms) with the sample surface (metallic or semiconducting), and when a single atom of the tip (meaning, the tip is atomically sharp) is closer to the surface than the other bulk atoms of the tip (Fig. 1.1). The sharp tip will produce atomic resolution due to the tunneling probability decreasing exponentially with distance; that is, as the tunneling barrier width increases, conductance across the tunneling junction decreases about one order of magnitude for every 0.1 nm increase in gap distance.[1]

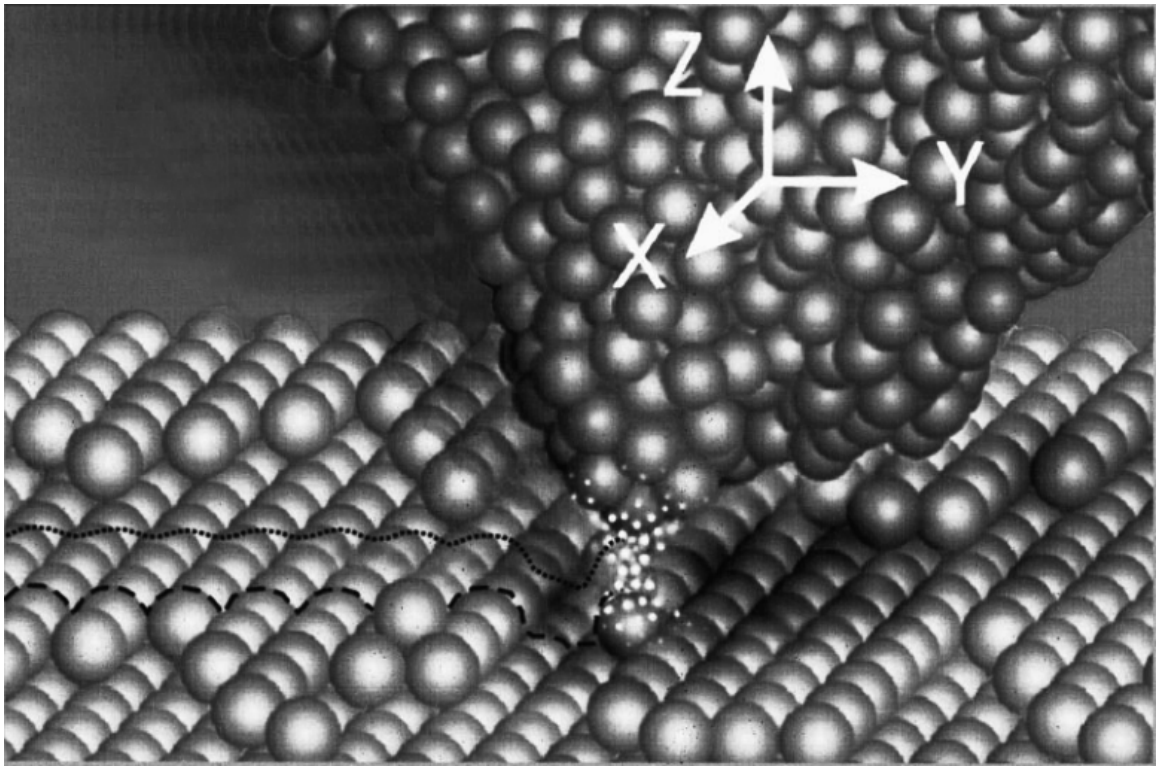

Figure 1.1. Cartoon schematic showing one atom of the tip is closer to the sample surface than the bulk atoms of the tip. The image also idealizes the narrow conduction channel for current flow. (Image from[5] modified by author.)

Attaching the STM tip to piezoelectric motors offers the fine-control necessary for atomic resolution. In the first STM created by Binnig and Rohrer, the louse-type,[2] the three spatial dimensions (x, y, and z) of the STM scanner are individually controlled by their own piezoelectric motors (Fig. 1.2.(a)). While another more recent type of STM, the Pan-type,[15] used in this dissertation, scanning is conducted by a single piezotube having electrical connections which apply perpendicular voltages that cause the scan tube to bend in the x- or y-directions (or a combination of the x- and y-directions), and to expand or contract in the z-direction (Fig.

1.2.(b, c)). By controlling the voltages applied to the scanner piezoelectric motors, the tip raster scans the surface in the x-y plane while the tip height over the surface is controlled by the *z*-motor and STM current feed-back loop.

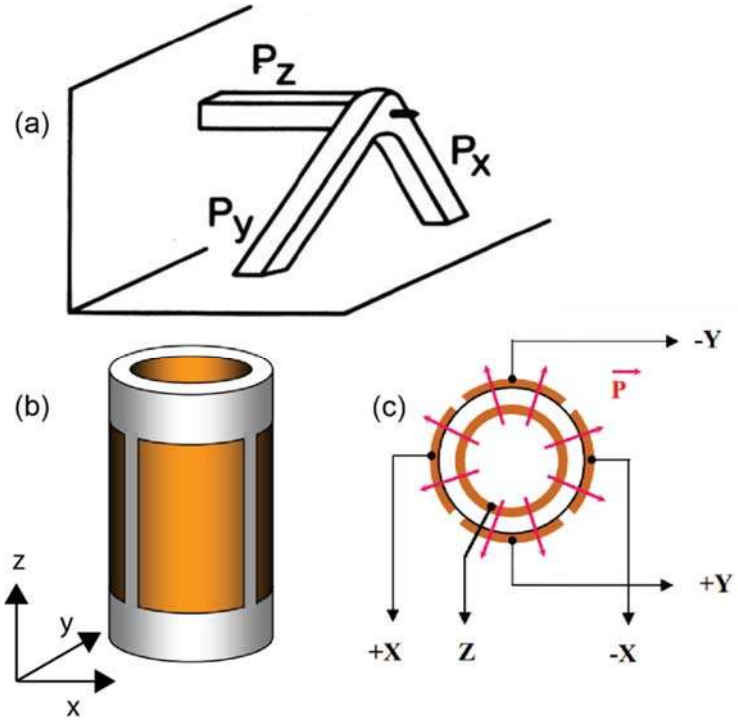

Figure 1.2. Types of Scanners. (a) The traditional tripod style of scanner showing that a STM tip was attached to three mutually exclusive piezoelectric motors.[2] (b) The newer type of scanner made of a tubular piezoelectric crystal (shown in white) whereby perpendicular voltages are applied to the tube electrodes (shown in gold) such that the tube flexes for x-y tip motion, and stretches/contracts to accommodate height change while scanning. The STM tip (not shown) is attached to the end of the piezo tube such that the tip and tube axes are parallel. (c) Diagram showing the polarization vector and position of electrodes on (b) for scanner control. Images (b) and (c) from[16] with (b) modified by author.

The fine-control of the z-direction piezoelectric motor is used to move the tip sufficiently close enough to the sample such that the electronic wavefunctions of the separate tip and sample states overlap in the vacuum barrier. Even though the wavefunctions overlap, there is no net current across the tunneling junction until a bias is applied to the tunneling junction. By convention, a tunneling junction with a positive bias means electrons are promoted such that they flow from the occupied states of the tip, across the tunneling barrier, and into the unoccupied states of the sample, or vice versa for negative bias; current is typically in the 1 to 1000 pA range, and bias is typically from a few millivolts up to around 10 V, although our experiments rarely use bias voltages higher than 5 V. The current across the tunneling junction is collected by the STM with the R9 software developed by RHK.

The STM described in this dissertation has room temperature scanning capabilities of 6.3 micrometers of total lateral (x, y) fine-scan motion, and about 1 micrometer of total fine-scan motion in the z-direction; at liquid helium temperatures, the aforementioned values are about one-fourth the room temperature motion. Chapter III will discuss the performance of the CCC STM in greater detail.

1.2. Motivation for Research

Personally, the main motivation for conducting this line of investigation was to do what had not yet been done; to push the

boundaries of understanding by solving a problem which had not yet been solved. Accordingly, the main question to be asked in is whether it is feasible to couple a CCC to a STM? Meaning, could atomic-scale results for STM and STS experiments be obtained with a liquid-helium "refrigerator" mounted on top of our STM? The idea seems like a logical step in the evolution of the two technologies, although it has yet to be completed and successfully reported in literature. Sometime over 6 years ago ARS, Inc. improved their commercially available CCC product line to the point that CCC vibrations were no more than 5 nm at the cold-finger (see Chap. III). Before then it was commonly believed that coupling a CCC to a STM could not produce atomic-resolution results due to mechanical vibrations. Combined with the newly available ARS, Inc. CCC (CS202PF-X20B) and the inherent rigidity of the Pan STM,[15] the research described in set out to investigate the feasibility of mating the new CCC design to a Pan STM with the aim of resolving atomic-scale electronic features and conducting atomic-scale spectroscopy.

Practically, the main motivation behind this dissertation is the projected scarcity (see Chap. III) and cost of helium since it must be mined from the earth. Unless humans find a new reservoir of helium, helium costs will increasingly become a more significant part of research budgets, possibly driving small-budget research groups out of business. Since the advent of the STM until now, STMs have traditionally used either flow- or bath-type cryostats to obtain cryogenic temperatures. One

major drawback to the flow- or bath-type cryostats is the cryogen (usually liquid helium, or liquid nitrogen) used to cool the experiment is boiled off and exhausted to atmosphere; cryogen is consumed on every low-temperature experiment conducted. It is possible to use a helium liquefier to collect the exhaust gas from the flow- and bath- type cryostats, such that the cryogen can be recompressed and purified for reuse. These types of recapture systems can be cost-prohibitive, since larger-scale liquefiers require a trained worker to operate and monitor the process, such as the one previously operated at the University of Oregon from circa 1970 to 1990.[17] As the price of helium continues to climb, helium liquefiers may become more attractive.

The drawback of using a CCC on a STM is the baseline cryogenic temperature is a few degrees Kelvin higher than the liquid helium temperature of 4.2 K. In our case, the lowest stable temperature obtained was ~11.5 K, although most experiments were conducted near 15 to 16 K due to temperature creep of the CCC.

The secondary benefit to having a CCC coupled to a STM is that we can remain on a subject of interest (nanoparticle, molecule, particular surface site, etc.) with very little thermal drift (0.18 A/h, refer to Chap. III) and we can remain at the site indefinitely (over 30 days so far).

The CCC STM will find its niche in research groups in that it can operate at cryogenic temperatures seemingly indefinitely without consuming cryogen (and, thus, grant money). Of course, the initial

hardware cost for the CCC is greater compared to a standard flow-type cryostat, but the initial hardware cost could be recovered after approximately one year of CCC STM experiments (as a quick estimate: our CCC hardware purchase price was ~$40,000, assuming *not* having to spend $1,000 per dewar of liquid helium per experiment, conducting one experiment per week while assuming 40 weeks of up-time, and allowing for 12 weeks of down-time and maintenance, hence 1 year).

The scientific community will benefit greatly from a nano-scale instrument capable of cryogenic measurements that uses very little, if any, helium, and which also facilitates long-term experiments with minimal thermal drift. The design, construction, and performance of the first ever STM coupled to a closed-cycle cryostat is described in this dissertation.

1.3. Overview of Dissertation

Chapter I provides a brief background of STM, discusses the motivation of the dissertation, and also contains a dissertation outline. Chapter II will provide a brief background of STM along with the basic theoretical background of tunneling. Chapter III was previously published in *Review of Scientific Instruments* with D. A. Kislitsyn, D. K. Beaman, S. Ulrich, and G. V. Nazin and describes the construction, design, and performance of the CCC STM. Chapter IV continues with the discussion of the CCC STM performance in a previously published paper

in the *Journal of Physical Chemistry Letters* with D. A. Kislitsyn, and G. V. Nazin and demonstrates the capability of the CCC STM to resolve vibrational excitations in electron transport through carbon nanotube quantum dots. Chapter V continues the discussion of the CCC STM performance in a previously published paper in the *Journal of Physical Chemistry Letters* with D. A. Kislitsyn, C. F. Gervasi, T. Allen, P. K. B. Palomaki, R. Maruyama, and G. V. Nazin and demonstrates the ability of the CCC STM to spatially resolve sub-bandgap states within individual lead sulfide nanocrystals. Chapter VI discusses future prospects of the research described in and concludes this dissertation.

CHAPTER II

SCANNING TUNNELING MICROSCOPY

2.1. Theory of Electron Tunneling

Electron tunneling is quantum mechanical effect whereby a particle with energy less than a potential barrier, non-destructively penetrates one side of a potential barrier, and then exits the other side of the barrier with its initial energy intact. This effect is not observed in classical mechanics. Classically, if a human being throws a tennis ball at a brick wall, the ball will not penetrate the wall and exit the other side. Quantum mechanically, though, the electron's energy is below the energy level of the wall (barrier), yet it still burrows (tunnels) through the wall with no loss in energy. That is, the electron does not have enough energy to overcome the barrier, yet, with a small but finite probability, it may still be found on the opposite side of the barrier continuing unabated on its path.

In an effort to understand how tunneling takes place in a STM, it will help to look at the one-dimensional model of tunneling as presented in [1]. By convention, electrons tunnel through the barrier in the *z*-direction, while the STM tip raster scans the x- and y-directions. Classically, an electron having energy E while moving through a potential $V(z)$ can be described by the equation

$$\frac{p_z^2}{2m} + V(z) = E, \tag{2.1.1}$$

with momentum p, and electron mass m. Quantum mechanically an electron is described by its wavefunction $\psi(z)$ such that the electron state can be determined using the Schrodinger equation,

$$\left[-\frac{\hbar^2}{2m}\frac{d^2}{dz^2} + V(z)\right]\psi(z) = E\psi(z). \tag{2.1.2}$$

The specific (eigen) solutions for the equation in the classically allowed regions (where $E > V$) are

$$\psi(z) = \psi(0)e^{\pm ikz} \tag{2.1.3}$$

and where k is the wave vector

$$k = \frac{\sqrt{2m(E-U)}}{\hbar}. \tag{2.1.4}$$

Moving in either the positive or negative direction, the electron has a constant momentum such that

$$p_z = \hbar k = \sqrt{2m(E-U)}. \tag{2.1.5}$$

In the regions that are forbidden classically, that is, where the energy of the electron is lower than the potential barrier energy, the solution to the Schrodinger equation is a decaying function where

$$\psi(z) = \psi(0)e^{-\kappa z}, \tag{2.1.6}$$

with decay constant

$$\kappa = \frac{\sqrt{2m(U-E)}}{\hbar}. \tag{2.1.7}$$

Equation 2.1.6 is a solution for an electron penetrating the barrier in the positive z-direction where the probability density for the electron at z is

$$|\psi(z)|^2 \propto |\psi(0)|^2 e^{-2\kappa z}. \tag{2.1.8}$$

Therefore, inside the forbidden region there is a nonzero probability of finding the electron. While an electron moving in the negative z-direction has the solution

$$\psi(z) = \psi(0)e^{\kappa z}. \tag{2.1.9}$$

Hence, an electron can penetrate the potential barrier and tunneling can take place. Showing that an electron has a small but finite probability of tunneling through the vacuum barrier of the STM junction.

2.2. Bardeen's Approximation and STM Imaging

The first theoretical model to describe experimental results of STM tunneling was provided by Tersoff and Hamann[2] as they applied a modified version of Bardeen's transfer Hamiltonian method[3] to the STM junction. In Bardeen's paper he expanded on the original tunneling experiments of Giaver,[4] and Nicol et al,[5] who made qualitative sense of their data assuming that the density of states was the relevant factor in electron tunneling. Bardeen made sense of the tunneling current using Fermi's Golden Rule for the probability of a transition, namely, that an

electron would transfer from the tip to the sample, or vice versa. The expression for a transition with probability w is

$$w = \frac{2\pi}{\hbar}\left|M_{\mu\nu}\right|^2 \rho_f, \tag{2.2.1}$$

with matrix elements $M_{\mu\nu}$, and energy density of final states ρ_f, while assuming $M_{\mu\nu}$ to be a constant. For positive bias of the tunneling junction, ω represents the rate at which tip electrons tunnel into available states of the sample. Bardeen continued his treatment with the implication that for the small energy differences involved, $M_{\mu\nu}$ is independent of energy.[3]

Tersoff and Hamann showed the tunneling current I can be determined using first-order perturbation theory, due to the weak coupling between the sample and tip,[6] such that

$$I = \frac{2\pi e}{\hbar}\sum_{\mu\nu} f(E_\mu)\left[1 - f(E_\nu + eV)\right] \times \left|M_{\mu\nu}\right|^2 \delta(E_\mu - E_\nu), \tag{2.2.2}$$

with Fermi function *f(E)*, applied voltage V, tunneling matrix elements $M_{\mu\nu}$ between the tip and sample state wavefunctions (ψ_μ and ψ_ν, respectively), and energy E_μ being the energy of ψ_μ when no tunneling events are taking place. The above equation can be simplified in the case of small voltages and low temperatures (when the Fermi function behaves as a step function) such that

$$I = \frac{2\pi e^2 V}{\hbar}\sum_{\mu,\nu}\left|M_{\mu\nu}\right|^2 \delta(E_\nu - E_F)\,\delta\left(E_\mu - E_F\right). \tag{2.2.3}$$

Now, as per Bardeen,[2,3] if the wavefunctions for each separate electrode are known, then one can calculate the tunneling matrix

$$M_{\mu\nu} = -\frac{\hbar^2}{2m}\int d\vec{S} \cdot (\psi_\mu^* \nabla\psi_\nu - \psi_\nu \nabla\psi_\mu^*)\,, \tag{2.2.4}$$

where the integral is over a separation surface located somewhere within the vacuum region between the two electrodes; it is not necessary to know precisely where the separation surface is drawn.[1]

Continuing on with their model, Tersoff and Hamann[7] modeled the STM probe as locally spherical at the tip, such that Equation 2.3 above simplified to

$$I \propto \sum_\nu |\psi_\nu(\vec{r}_0)|^2\, \delta(E_\nu - E_F), \tag{2.2.5}$$

with the surface local density of states (LDOS) of the sample defined as

$$\rho_\nu(\vec{r}_0, E_F) \equiv \sum_\nu |\psi_\nu(\vec{r}_0)|^2\, \delta(E_\nu - E_F), \tag{2.2.6}$$

where σ is in ohms^{-1}, distances are in atomic units, energy in units of eV, and $\rho_\nu(\vec{r}_0, E_F)$ is the LDOS of the tip surface. Therefore, in the constant current topography mode (used in this dissertation), the scanned images are related to contour scans of constant surface (sample) LDOS.

2.3. Scanning Tunneling Spectroscopy

Continuing on with the work of Bardeen, Tersoff, and Hamann, Chen[1] shows that to understand STM spectroscopy results, one can start with Equation 2.2.2 above. At a bias voltage V, the tunneling current can be determined by summing over the relevant states. For the temperature range of typical STM experiments, the electrons in the tip and sample states obey the Fermi distribution. Thus, the tunneling current becomes

$$I = \frac{4\pi e}{\hbar}\int_{-\infty}^{\infty}[f(E_F - eV + \epsilon) - f(E_F - \epsilon)] \times \rho_\mu\,(E_F - eV + \epsilon)\,\rho_\nu(E_F + \epsilon)|M|^2 d\epsilon \tag{2.3.1}$$

respectively, and the Fermi distribution is

$$f(E) = \frac{1}{1 + \exp\left(\frac{E - E_F}{k_B T}\right)}. \tag{2.3.2}$$

The Fermi distribution can then be approximated as a step function if $k_B T$ is smaller than the energy resolution of the measurement, such that the tunneling current becomes

$$I = \frac{4\pi e}{\hbar}\int_{0}^{eV} \rho_\mu\,(E_F - eV + \epsilon)\,\rho_\nu(E_F + \epsilon)\left|M_{\mu\nu}\right|^2 d\epsilon. \tag{2.3.4}$$

Drawing on Bardeen's above assumption that the tunneling matrix $M_{\mu\nu}$ is constant in the range of measurements, one can see that the STM tunneling current is a convolution of the tip and sample density of states as follows,

$$I \propto \int_0^{eV} \rho_\mu \left(E_F - eV + \epsilon\right) \rho_\nu (E_F + \epsilon) d\epsilon. \tag{2.3.5}$$

We can now simplify the above equation by assuming that a metallic tip has a constant LDOS in the relevant energy interval such that

$$\frac{dI}{dV} \propto \rho_\nu (E_F + eV). \tag{2.3.6}$$

Thus, differential conductance (dI/dV) is a direct measurement of the sample local density of states.

2.4. Bridge to Chapter III

Equipped with the above elementary principles of quantum tunneling as applied to STM, we set out to prove the operational feasibility of coupling a CCC to an STM. With the main thrust of the work being the construction of a novel CCC UHV STM. The novel system was characterized by conducting topography scans on atomically clean and atomically flat surfaces of Au(111), NaCl(100)/Au(111), and carbon nanotubes (CNTs) deposited onto Au(111); conducting scanning tunneling spectroscopy (dI/dV) on CNTs; analyzing thermal drift of the tip piezoelectric motors; carrying out noise analysis of the tunneling

current as a result of cryostat vibrations; and, finally, the cool-down performance of the CCC was also characterized. These details are discussed in Chapter III.

CHAPTER III

A HIGH-STABILITY CRYOGENIC SCANNING TUNNELING MICROSCOPE BASED ON A CLOSED-CYCLE CRYOSTAT

This work was previously published with coauthors Jason D. Hackley, Dmitry A. Kislitsyn, Daniel K. Beaman, Stefan Ulrich, and George V. Nazin, in the *Review of Scientific Instruments* 85, 103704 (2014), doi: 10.1063/1.4897139, © 2014 AIP Publishing LLC.

3.1. Introduction

Now in its fourth decade of existence, scanning tunneling microscopy (STM)[1] has become an essential tool that has provided unique insights into the atomic structures of a wide variety of surfaces and nanoscale systems. Scanning Tunneling Spectroscopy (STS)[1] is one of the important capabilities of STM that provides atomic-resolution information about the electronic structures of sample surfaces. STM experiments probing the spatially-dependent spectroscopic properties of surfaces at the atomic scale typically require ultra-high vacuum (UHV) conditions and cryogenic temperatures: UHV enables preparation and use of well-defined atomically clean surfaces, while low-temperatures

greatly enhance the mechanical stability of the STM junction, freeze the motion of weakly-bound adsorbates, and improve the spectroscopic resolution of STM by reducing the thermal broadening of spectroscopic features. The majority of STM systems intended for high-performance STS experiments have so far been constructed coupled to a variety of different cryostats, such as continuous-flow[2-4] or bath-cryostats.[5-7] So far, operation of all of these cryostats relied on the use of cryogens, with the best operating conditions achievable with liquid helium. The dramatic increase of liquid helium costs over the past decade[8] has led to a situation where using liquid-helium for STM instruments is becoming prohibitively expensive. Near-future projections predict further price increases by up to 50%.[8] Development of a cryogen-free STM operating at near liquid-helium temperatures is thus important for sustaining the current level of activity of STS-based studies in a variety of research fields.

In this communication, we present a novel cryogenic UHV-STM instrument that, for the first time, achieves temperatures as low as 16 K by using a closed-cycle cryostat (CCC).[9] The cryostat is based on the Gifford-McMahon (GM) design, which uses recirculating helium-gas thus obviating the need for liquid helium. The use of a CCC for STM is counterintuitive due to the inherent noise of CCCs: GM cold-heads, in particular, incorporate moving parts located in close proximity of the cold finger where instrumentation is typically mounted. Another variation of

CCC, pulse-tube based refrigerators also display significant mechanical vibrations.[10] By using a novel CCC, which is thermally linked to the STM system through helium exchange gas confined inside a volume confined by highly flexible rubber bellows, we have achieved a significant reduction of the mechanical noise transferred from the CCC to the STM.

The performance of the new STM is comparable to the established designs based on the continuous flow- or bath-cryostats. Noise analysis of the tunneling current shows current fluctuations up to 4% of the total current, which translates into tip-sample distance variations of up to 2 picometers. This noise level is sufficiently low to allow atomic-resolution imaging of most surfaces typically studied with STM, as demonstrated in this manuscript using Au(111) and NaCl(100)/ Au(111) surfaces, as well as carbon nanotubes deposited on Au(111). With the need for conservation of liquid helium removed, we are able to actively stabilize the temperature of the scanner using a heater controlled by a feedback mechanism. This enables temperature stability on the scale of +/-1 milli-Kelvin, which leads to extremely low lateral and vertical (tip-sample distance) drift rates. Thermal drift analysis showed that under optimized conditions, the lateral stability of the STM scanner can be as low as 0.18 Å/hour. STS measurements (based on the lock-in technique) with the new STM show no detectable presence of noise from the closed-cycle cryostat.

3.2. System Design

3.2.1. STM/Scan Head

Despite the mechanical separation of the STM chamber from the CCC, residual mechanical noise appearing as spikes of up to 5 nanometers can still be present on the cryostat cold-finger mounted on the STM chamber side.[11] These vibrations have a low frequency of 2.4 Hz, which makes it imperative for the STM scanner assembly (including the sample and sample holder) to be as rigid as possible. The Pan-style design[6] was therefore chosen for the STM scanner, as it is one of the most rigid designs developed so far. The scan-head was designed in cooperation with RHK Technology, Inc., which has pioneered the commercial development of Pan-style STM scanners.[12]

The STM scanner, constructed by RHK Technology, incorporates a set of piezo-drive positioners, which, in addition to the coarse approach capability realized by a Pan-style Z-positioner, allow lateral coarse-positioning of the sample using a combined XY piezo-drive positioner.[13] The total range of all three positioners covers a volume of 8 mm x 4.5 mm x 4.5 mm. The positioners are assembled onto a rigid gold-coated molybdenum housing (Figure 3.1). Molybdenum was chosen because in addition to high stiffness, it possesses good thermal conductivity and a low thermal expansion coefficient that is a good match for other components of the system. The body of the scanner was designed to accommodate an additional set of piezo motors for positioning of optics

for Scanning Tunneling Luminescence experiments.[14-17] The constructed STM scanner is highly immune to external vibrations and is capable of atomic-resolution imaging (of graphite surfaces) in ambient conditions with minimal vibrational isolation (for example, a rubber pad placed under the scanner was found to be sufficient). For optimal vibrational isolation, our STM is suspended on stainless steel springs, and is eddy-current damped by eight samarium-cobalt magnets attached to the STM body (Figure 3.1). Each spring consists of two sections connected with a ceramic/stainless-steel coupler acting as an electrical and thermal break. The natural frequency of the hanging STM is 1.7 Hz, below the fundamental noise frequency generated by the CCC.

3.2.2. Radiation Shields

To achieve near-liquid helium temperatures, our design incorporates two nested thermal radiation shields constructed from gold-plated oxygen-free high-conductivity copper (Figure 3.1).[3] The two radiation shields are mounted to two cooling stages of the CCC: the outer thermal shield is attached to the first cooling stage (not shown), which during experiment is at 25-35 K; and the inner radiation shield is attached to the second cooling stage (Cold Finger in Figure 3.1), and is typically at ~15 K. The target temperature is typically maintained a fraction of a degree above the minimal attainable temperature using a

heater wound on the cold finger. The heater is regulated using the feedback control loop of the temperature controller.

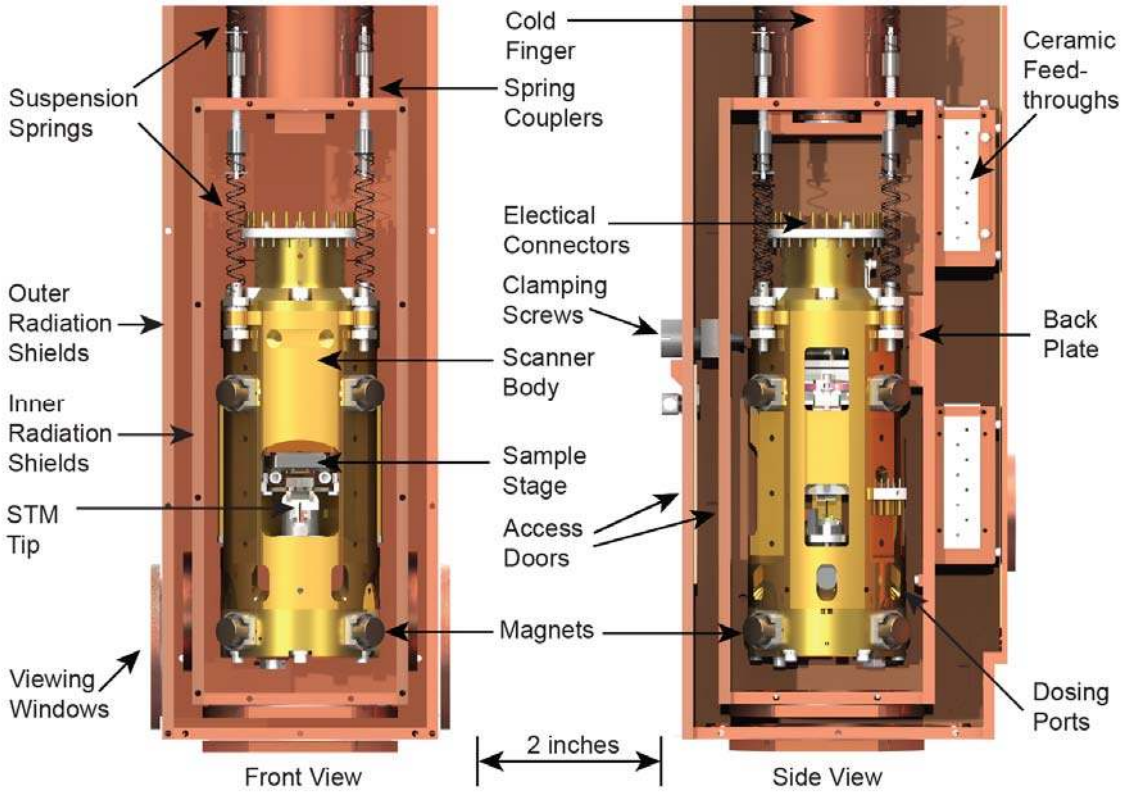

Figure 3.1. STM scanner suspended inside the thermal radiation shields. Left: front view of STM in shields with front-facing shields removed. Right: side view of STM in shields with side-facing shields removed. The inner radiation shield is mounted directly to the cold tip, which is the second cooling stage of the cold finger. The outer radiation shields mount directly to the first cooling stage of the cold finger (not shown). Springs extend approximately four inches above the area shown.

The STM body is cooled via a bundle of fine copper wires (0.005 in) connected to the top of the inner radiation shield via a sapphire piece

(sapphire was chosen in order to avoid direct electrical contact). Additional cooling is provided by electrical connections (0.005 in copper wires) connected to electrical feedthrough panels mounted on the backside of the inner shield (Figure 3.1). The feedthrough panels were made from Shapal,[18] which has high thermal conductivity thus providing efficient thermal anchoring of electrical connections to the inner shield. Electrical connections from the inner shield feedthrough panels to the outside were made using stainless steel wires to minimize the thermal leak. To minimize the thermal load on the feedthrough panels, the stainless steel wires are thermally anchored at the outer thermal shield. During cool down, two spring-loaded screws mounted on the inner radiation shield are used to clamp the STM scanner to the back plate of the inner radiation shield (Figure 3.1). The screws are released upon reaching the target temperature, so that the STM scanner hangs free, with the scanner temperature about 1.3 K higher than that of the inner radiation shield.

Each radiation shield incorporates a set of windows (sapphire for the inner shield and fused silica for the outer shield), which allow fine-scale observation of the STM junction and sample, as well as monitoring tip- or sample exchange. The radiation shields, as well as the STM scanner, were designed and constructed with line-of-site openings for in-situ evaporation/dosing directly into the STM junction by using thermal evaporators or gas sources mounted in the UHV system.

3.2.3. Cooling System

To achieve cryogenic temperatures, we used a CCC manufactured by Advanced Research Systems, Inc.[9] The main components of the CCC are: 1) the GM cryocooler [DE202PF, Figure 3.2(a)]; 2) a low-vibration interface (DMX-20) incorporating a UHV-compatible cold finger to which the STM radiation shields are mounted [Figure 3.2(a)]; 3) a water-cooled compressor (ARS-2HW, not shown) that supplies compressed helium to the cryocooler. The cryocooler, the main source of the 2.4 Hz noise, is mounted on a separate support structure that is mechanically decoupled from the STM system [Figure 3.2(b)], and is anchored directly to the floor surface that is direct contact with the underlying bedrock below the laboratory space. The thermal link between the cooler and cold finger is realized using a heat exchange interface consisting partly of a rubber bellows filled with helium gas, with the rubber bellows being the only source of mechanical coupling between the cryocooler and the UHV system. While this does not completely eliminate vibrations, the residual vibrational noise typically registered at the cold finger end is within 5 nanometers, four orders of magnitude lower than the noise level at the cryocooler.[11]

3.2.4. UHV System Design

Several measures were taken to minimize the noise experienced by the STM system. The UHV STM system was assembled on the rigid

concrete floor of the basement. The floor is anchored to the underlying bedrock via six reinforced concrete piers. The UHV chamber sits on an optical table with rigid mount legs without any additional vibrational isolation. The system is located in a "sound proof" room with low-noise ventilation baffles and dampers maintaining laminar air flow. The roughing pumps are located in an isolated pump room. The vacuum backing lines were attached to the chamber via stainless steel bellows, and are routed through sand-filled boxes to damp the mechanical vibrations generated by the backing pumps.

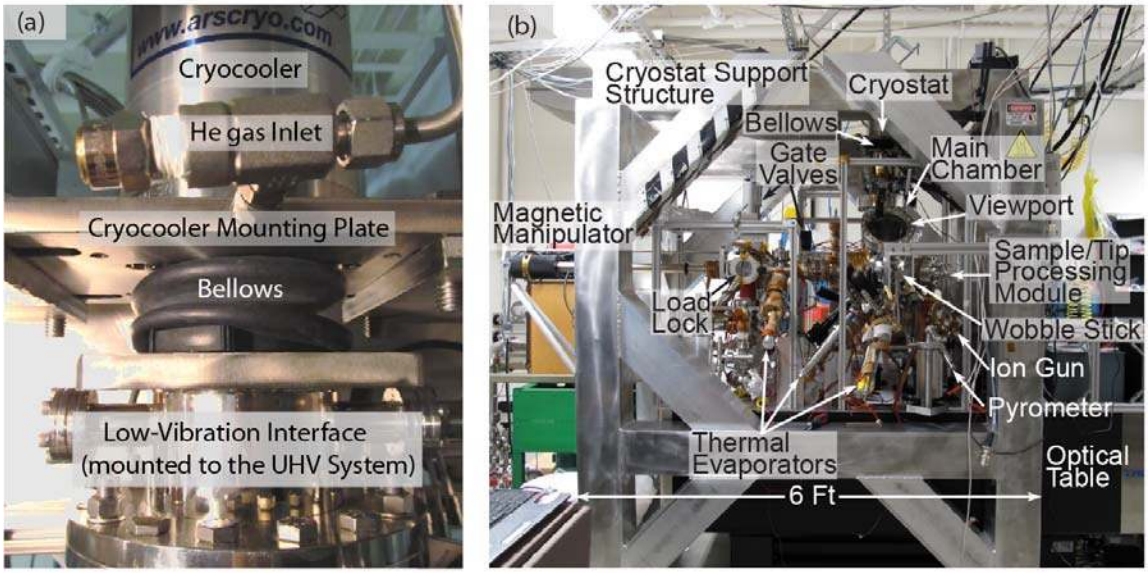

Figure 3.2. Overview of the vacuum and cooling systems. (a) Thermal connection between the Cryocooler and Cold Finger is realized via He-filled volume confined by a rubber bellows. (b) View of the UHV system. The cryostat is mounted above the UHV system to the cryostat support structure. The cryostat support structure has no contact with the UHV system.

The vacuum system is composed of the main chamber, a load-lock chamber for quick tip and sample exchange, and a process gas manifold, each with a dedicated pumping line composed of a 75 L/s turbo pump and a dry scroll pump. In the case of the main chamber, the 75 L/s turbo pump serves as a backing pump for a 300 L/s magnetically-levitated turbo pump mounted directly on the chamber. In addition, the main chamber is pumped by a 300 L/s ion pump integrated with a combination of a titanium sublimation pump and cryogenically-cooled shroud. The baseline pressure in the main chamber is ~4×10^{-11} torr, and at 2×10^{-11} torr during experiments at cryogenic temperatures, due to the cryo-pumping action of the radiation shields/cryostat.

3.2.5. Sample Preparation

In addition to the STM, the main chamber houses the tip- and sample preparation and storage facilities. Samples (mounted on molybdenum sample holders) and tips are stored in a "carousel" module inside the main chamber (Figure 3.3) with nine slots for samples and thirty slots for tips. The samples and tips are exchanged between the load lock and the main UHV chamber by using a precision magnetic manipulator. Inside the main chamber, the samples and tips are manipulated using a wobble-stick allowing three-dimensional translation and rotation around the wobble-stick axis. Tips and samples are prepared in-situ via cycles of annealing and neon-ion-sputtering using a

custom multifunctional processing module (Figure 3.3). The module incorporates a current-carrying filament that can either be used for e-beam or radiation heating of individual samples and tips.[3] During the annealing process, the temperature of the sample is monitored by a pyrometer. An ion gun is used for sample sputtering, while tips are self-sputtered when biased to high voltage in neon pressure.

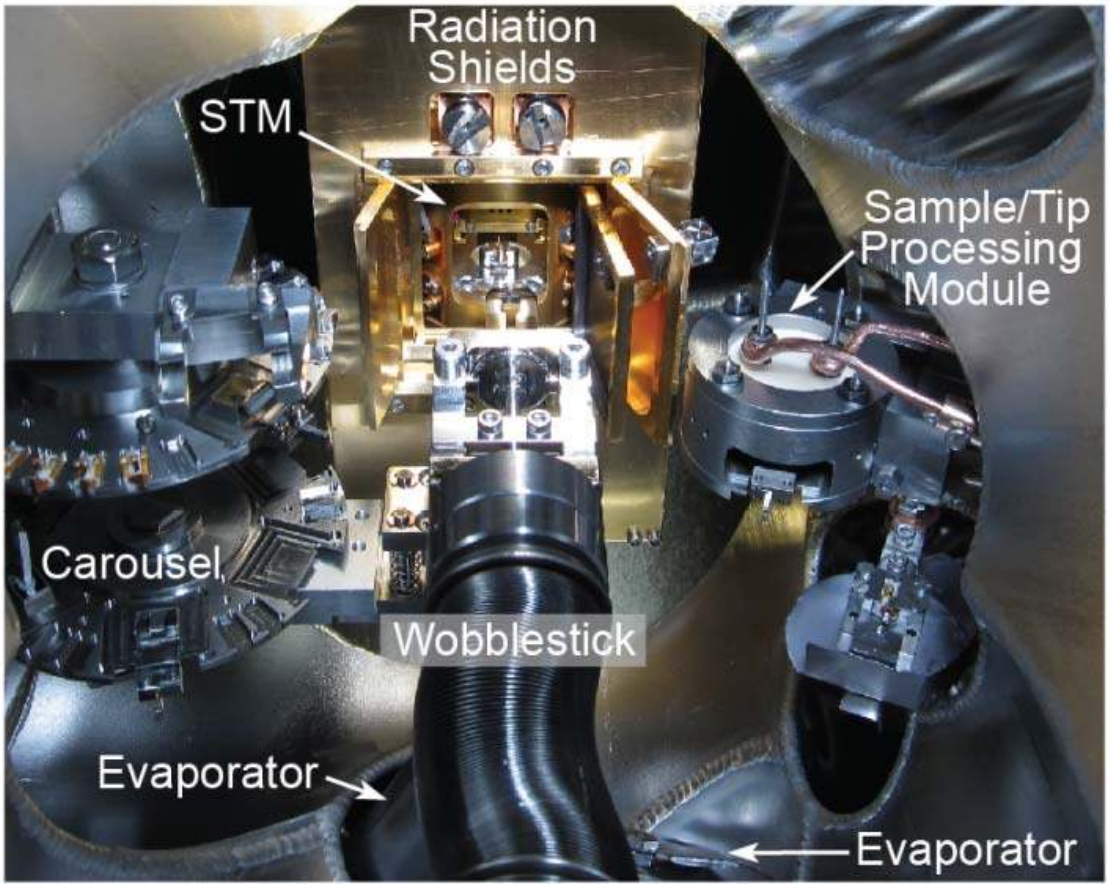

Figure 3.3. View of the main chamber interior looking through the view port. Both the outer and inner radiation shield doors are open, affording a view of the STM.

After an atomically clean sample surface is obtained, a wide variety of materials can be deposited on the surface using several facilities implemented in the system: 1) four different ports are available on the main chamber for mounting either gas/vapor sources or thermal evaporators [Figure 3.2(b)], two of which are aligned into the STM junction. Thus, materials with appropriate vapor pressures can be evaporated in situ. All of these ports have dedicated gate valves, which allow exchange of gas/vapor sources or thermal evaporators without breaking vacuum in the main chamber; 2) a "dry contact transfer"[19] capability is available for deposition of nanoscale materials and molecular materials that do not have sufficient vapor pressures for evaporation, such as carbon nanotubes, graphene flakes, and polymers; 3) a facility for deposition of materials from solution using a pulsed valve[20-21] is implemented in the load-lock, and has been successfully used for deposition of colloidal quantum dots.

3.3. Performance

3.3.1. Cool-down and Operation

Full cool-down of the STM from room temperature to near-liquid helium temperatures takes approximately twelve hours [Figure 3.4(a)], and is typically carried out overnight. During cool down, the STM is clamped to the back plate of the inner radiation shield. Upon reaching the target temperature the STM is unclamped and hangs free. After the

cool-down, the cold-finger temperature is actively stabilized using a heater controlled by a feedback mechanism, such that the STM temperature remains stable for days within +/-1 mK [Figure 3.4(b)]. The high temperature stability enables extremely low lateral and vertical tip-sample drift rates, as described below. So far, we have found no limitation on the duration of individual experiments: we have conducted experiments lasting several weeks without any major changes in operating conditions, except for the need to periodically (every several days) to increase the feedback set-point temperature. This is likely due to condensation of air/water vapor inside the volume filled with exchange He gas.

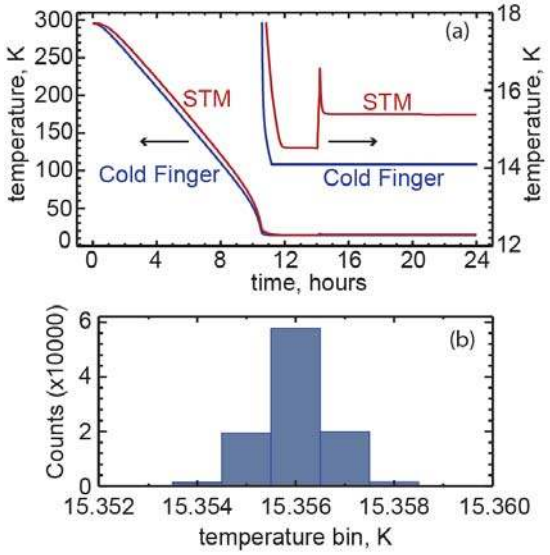

Figure 3.4. (a) Typical cool down curves showing temperatures measured at the STM and at the Cold Finger. The two curves in the upper right corner show the variation of the temperatures after unclamping of the STM (seen as a spike in the top curve). (b) Histogram showing typical variations of the STM temperature when the temperature stabilization feedback mechanism is engaged. Each count corresponds to an individual reading of the temperature by the controller electronics.

3.3.2. Atomic Resolution

The imaging capabilities of the new STM under cryogenic conditions were tested on several different samples with different surface structures. Figure 3.5(a) shows a topography scan of a Au(111) surface (acquired at ~16 K), which displays a clear hexagonal atomic pattern characteristic of the Au(111) surface,[22] with no identifiable features attributable to the CCC noise. Figure 3.5(c), a cross-section of topography from Figure 3.5(a), shows well-defined atomic corrugation of ~30 pm. Another example of atomic-scale resolution, Figure 3.5(b), shows a topography scan of a NaCl(100) monolayer film thermally deposited on the Au(111) surface (image acquired at ~16 K). Figure 3.5(b) shows a square lattice with a lattice constant of 0.40 nm, as expected for the NaCl(100) lattice. Similarly to Figure 3.5(a), no identifiable features attributable to the CCC noise are present in the image. Figure 3.5(d), a cross-section of topography from Figure 3.5(b), shows well-defined atomic corrugation of ~10 pm, suggesting that the CCC noise is significantly less than this number. Atomic-resolution images were also obtained on single-walled carbon nanotubes deposited on the Au(111) surface, with one example shown in Figure 3.5(e).

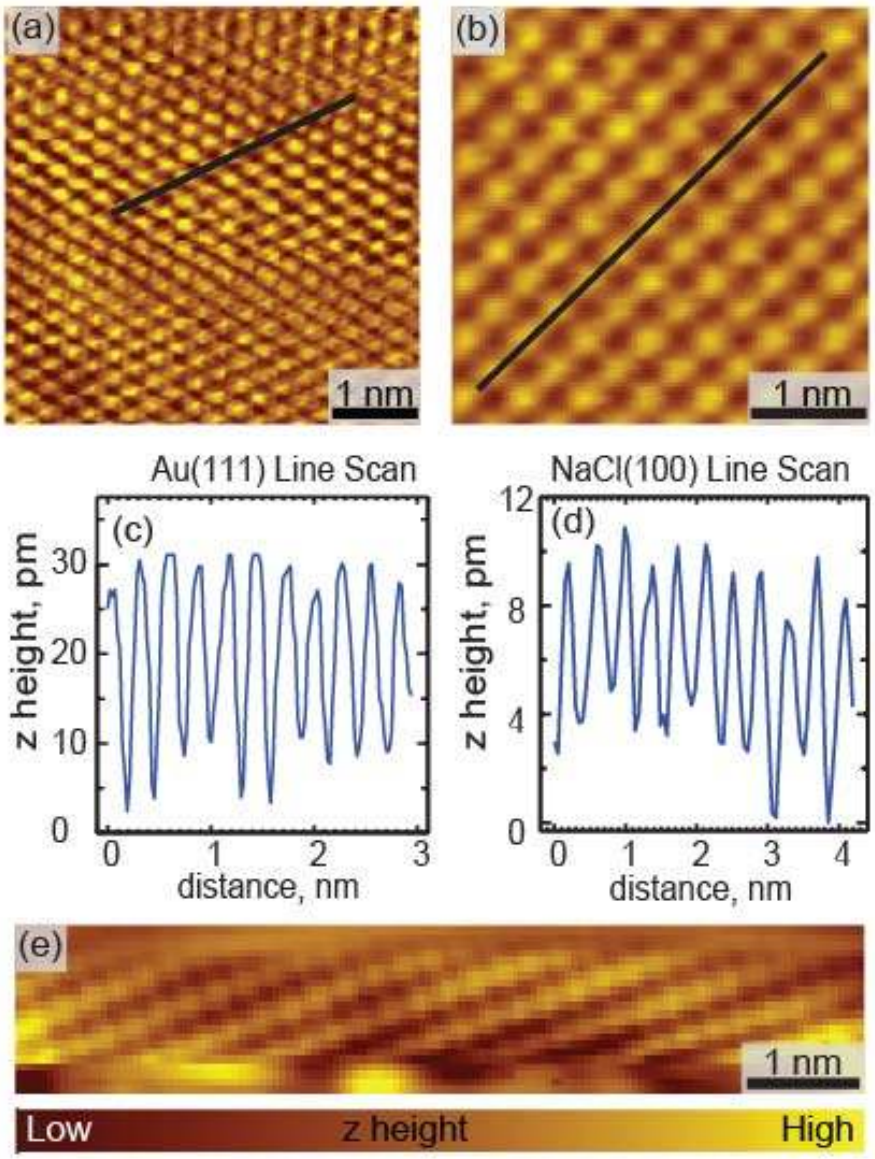

Figure 3.5. Atomic-resolution images acquired with the new STM. (a) Topography scan showing atomic resolution of a reconstructed Au(111) surface [set point: 1.00 V, 100 pA]. The bright peaks represent the Au atoms. (b) Topography scan of monolayer of NaCl(100) thermally evaporated on the Au(111) surface [set point: 1.50 V, 10.0 pA]. The bright peaks represent the Cl atoms. (c) Cross-section of topography from (a) taken along the black line shown in (a). (d) cross-section of topography from (b) taken along the black line shown in (b). (e) Atomically resolved surface of single-wall carbon nanotube [set point: 1.50 V, 5.0 pA].

3.3.3. Noise Analysis

To quantify the noise generated by the CCC more directly, with the STM operating at 16 K, we measured the tunneling current as a function of time (Figure 3.6) after turning off the z-piezo feedback, thus allowing the tip-sample distance z to be modulated by the external mechanical/acoustical noise. The tunneling current in Figure 3.6 clearly shows periodic spikes with a period of ~0.42 s, matching that expected for the fundamental frequency of the CCC (2.4 Hz). The typical amplitude of each spike is on the scale of ~ 16 pA, a ~4% correction to the total current. We can estimate the corresponding noise-induced tip-sample variation, by noting that the change of z by one angstrom changes the tunneling current by approximately a factor of ten. This means that a ~4% variation of the current should produce a 1.7 pm variation in z. This is a small number as compared to the atomic corrugations observed in Figure 3.5, explaining the lack of CCC-induced noise features in our STM images.

3.3.4. Scanning Tunneling Spectroscopy

STS measurements were carried out using the lock-in technique, with the modulation frequency typically in the range from 500 to 1000 Hertz. With typical lock-in time constants being on the scale of at least a few hundred milliseconds, the lock-in signal is not expected to be very sensitive to the small current noise generated by the CCC, due to its low

frequency of 2.4 Hertz, even though higher harmonics (up to 14.4 Hz) are distinguishable in the Fourier spectra of the tunneling current (not shown). This expectation is universally corroborated by the STS spectra measured for several nanoscale and molecular materials including: carbon nanotubes, PbS and CdSe quantum dots, and oligothiophene molecules. As a representative example of STS measurements, here we show a spectrum of a carbon nanotube deposited on the Au(111) surface (Figure 3.7). The STS spectrum of the nanotube clearly shows the first and second Van Hove singularities visible both in the valence and conduction bands, with the bandgap being ~1.3 eV. Both forward and backward sweeps are presented showing reproducibility of the data.

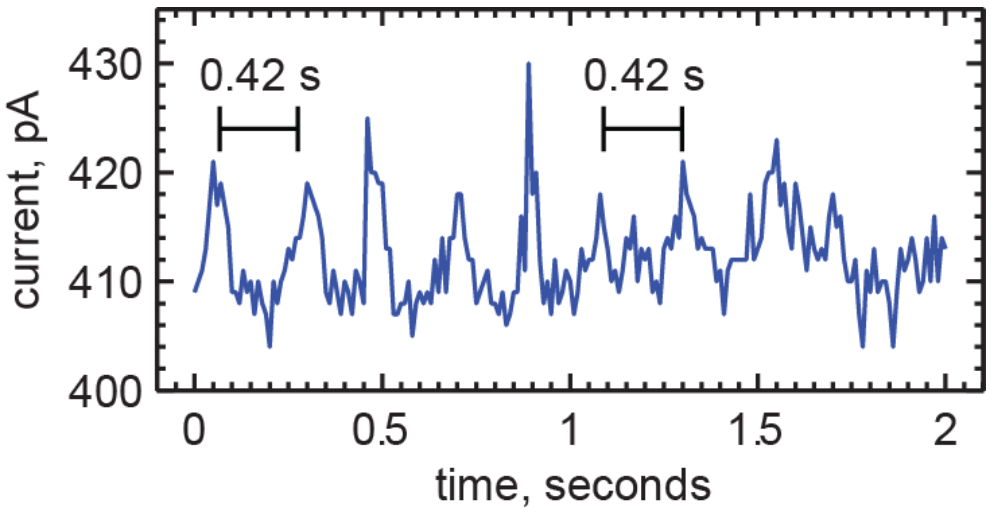

Figure 3.6. Tunneling current as a function of time, with the closed cycle cryostat operating at 15 K. To more clearly show the mechanical component of the CCC-noise, the current was measured with a low-pass filter with a corner frequency of 250 Hz.

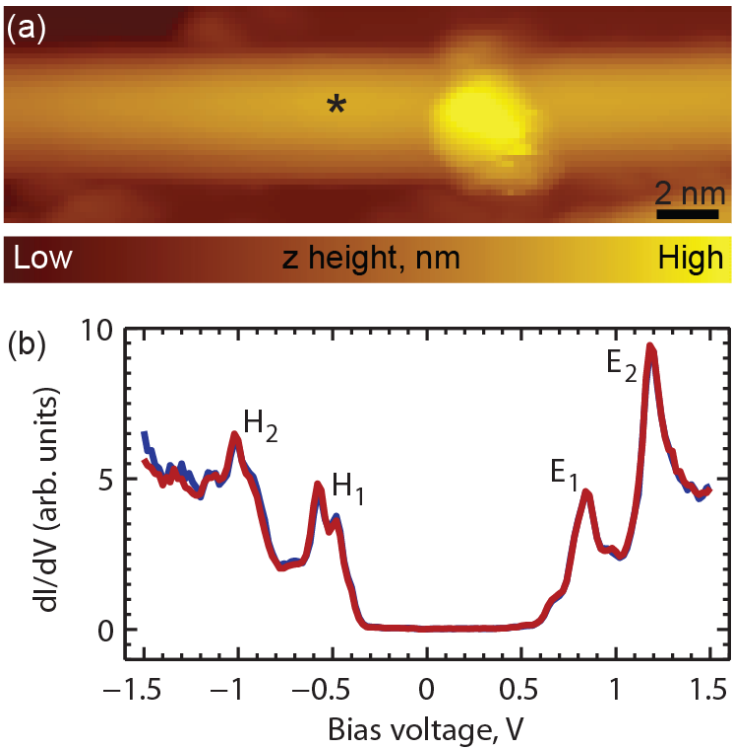

Figure 3.7. STS spectroscopy of a single-wall carbon nanotube. (a) STM image of the nanotube. (b) Two STS spectra measured in one sweep from -1.5 V to 1.5 V (red curve) and back to -1.5 V (blue curve). The spectra were measured in the location shown by an asterisk in (a). The peaks observed in (b) are identified as Van Hove singularities associated with the valence (peak H_1) and conduction (peak E_1) bands. Higher order bands H_2 and E_2 are also observed. The STS spectra were obtained by measuring differential conductance, dI/dV, using the lockin-technique with a modulation of 20 mV. Tunneling set point: 1.5 V, 0.1 nA. Acquisition time: 2 minutes per spectrum.

3.3.5. Spatial Drift Analysis

One of the critical specifications of a spectroscopic STM is its intrinsic rate of spatial drift: many types of STM-based spectroscopic measurements require extended data acquisition, which makes results sensitive to spatial drift on the atomic scale. Examples of such spectroscopic measurements are the Inelastic Tunneling Spectroscopy,[23]

Scanning Tunneling Luminescence,[15] or simply detailed mapping of STS spectra of individual molecules. To quantify the typical rates of spatial drift in our STM, we compared STM images taken over the course of 120 hours (images not shown). Figure 3.8 shows that the lateral drift (caused primarily by the piezo creep after moving by 40 nm into a new area) slows down dramatically over the period of the first 15 hours, and reaches a small steady drift rate of 0.18 Å/hour after the first 30 hours.

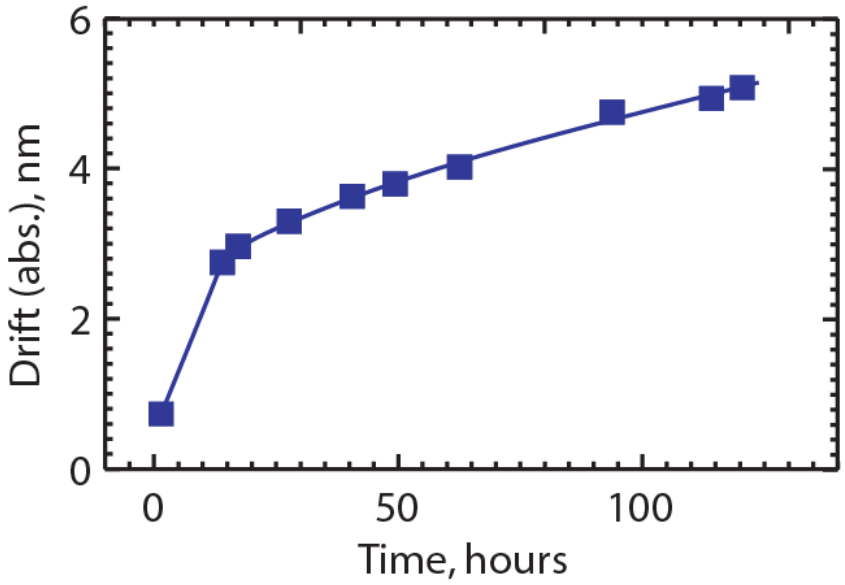

Figure 3.8. X-Y spatial drift as a function of time. The drift was calculated by comparing STM images of the same area.

3.4. Conclusion

The atomically-resolved data collected using the new STM demonstrate, for the first time, the feasibility of combining an ultra-high vacuum STM instrument with a closed-cycle cryostat for achieving near-

liquid helium temperatures necessary for the optimal performance of the spectroscopic mode of STM, Scanning Tunneling Spectroscopy. The use of a closed-cycle cryostat eliminates costs associated with liquid-helium, and removes limitation on the durations of individual experiments. The quality of the collected data shows that the new STM is functionally equivalent to the existing high-performance cryogenic STM systems. Additionally, the STM spatial drift rate may be further reduced by using active stabilization of the scanner temperature with a feedback-controlled heater. The combination of a virtually unlimited experiment duration and reduced spatial drift afforded by the new design will enable significantly more detailed spectroscopic investigations of samples that require extended characterization times. This, for example, includes a wide variety of samples important for nanoscale materials science, because nanoscale materials (quantum dots, carbon nanotubes, nanowires, thin films, etc.) often exhibit pronounced structural or compositional inhomogeneities.

3.5. Bridge to Chapter IV

The concept of coupling a CCC to a PAN-style STM with the expectation of obtaining atomic-resolution has now been shown to be quite feasible, with experimental results showing that our STM can produce results similar to traditional style STMs coupled to flow-type cryostats. Being that atomic-resolution data can be expected, we next

turned out attention to the CNT system. In Chapter IV, the vibronic states of a CNT were mapped. The data will show that because of our high-stability CCC STM design, we were able to see the quantum mechanical effect of the particle in a box vibronic states as a result of a defect within the CNT.

CHAPTER IV

VIBRATIONAL EXCITATION IN ELECTRON TRANSPORT THROUGH CARBON NANOTUBE QUANTUM DOTS

This work was previously published with coauthors Dmitry A. Kislitsyn, Jason D. Hackley, and George V. Nazin in the *Journal of Physical Chemistry Letters*, 5, 3138-3143 (2014), dx.doi.org/10.1021/jz5015967,

4.1. Introduction

Semiconducting single-walled carbon nanotubes (SWCNTs) are a promising material with unique photophysical[1-2] and electronic properties[3-4] which are, however, easily masked by interactions with the nanotube immediate environment. An important example of this environmental sensitivity is electron transport through SWCNTs, where environmental effects have been shown to be responsible for charge carrier scattering,[5-7] localization,[8-9] and random-telegraph-signal noise.[10-11] These effects have been attributed to the existence of charge traps localized in the nanotube vicinity, inferred from the marked spatial

modulations of electrostatic potentials observed using scanning-gate microscopy[12-13] and scanning photovoltage microscopy.[5] Despite the insights obtained using these techniques, their spatial resolution is limited (10 nm for scanning probe techniques), which leaves the effects of shorter-scale disorder largely unexplored. Short-scale disorder is highly relevant to optoelectronic applications because optical excitation can produce photo-ionized charges transiently trapped in the SWCNT vicinity, a scenario suggested by blinking and spectral diffusion of SWCNT photoluminescence,[14] and by scanning photovoltage measurements.[5] Trapped charge would lead to the simultaneous creation of an effective potential barrier for one type of charge carriers (electrons or holes), and a potential well for the other type of charge carriers. While the influence of the former on charge transport is relatively well-understood,[15] the impact of a potential well is difficult to predict. Due to the electron-phonon coupling, the electronic states localized in the well can be expected to produce a manifold of local vibronic states sensitive to the degree of localization. Such local vibronic states would have a direct impact on electron transport because they would mediate charge transfer across the localized electronic states.

Here we use Scanning Tunneling Spectroscopy[16] (STS) to study, for the first time, the electron-phonon coupling for electronic states localized in short segments of semiconducting SWCNTs. STM imaging of SWCNTs deposited on the Au(111) surface (see Experimental Methods) shows

SWCNTs in a variety of environments. STS of SWCNTs adsorbed on Au(111) terraces (Figure A.1; see Appendix A for supplemental figures for this chapter) shows relatively spatially-uniform density of states (DOS) consistent with those reported in literature: the spectra are dominated by Van Hove singularities associated with the electronic band onsets.[17-18] Due to the presence of non-SWCNT material in the SWCNT-containing powder used for deposition, a significant fraction of SWCNTs in our experiments show unidentified material in the nanotube vicinity. This material can locally prevent nanotubes from making extended contact with the surface resulting in height variations such as that shown in Figure A.2(a). The intermittent contact leads to spatially-modulated charge transfer interaction with the Au(111) substrate, capable of producing quantum-confined states.[19] In these conditions, the DOS-peaks found in the STS spectra of such SWCNTs (Figure A.2(b)) contain fine structures with voltage-spacings reproducible for many different nanotubes (Figure A.3). This suggests vibrational nature of these features, but to unequivocally establish their origin, it is useful to study examples of SWCNTs where electronic confinement is more pronounced, and the nanotube adsorption configuration is more well-defined. One such example corresponds to the situation where a SWCNT is suspended across an atomic step on the Au(111) surface, as schematically illustrated in Figure 4.1(a). An STM image of a SWCNT adsorbed in this geometry is shown in Figure 4.1(b). The topographic profiles of the

nanotube and underlying surface (Figure 4.1(c)) show that the height change from point L to point R is identical to the height of an atomic step on the Au(111) surface. This allows us to conclude that the nanotube is in contact with the surface in points L and R assuming that the local electronic structures of the nanotube in these points are similar (this is corroborated by the STS measurements discussed below). The segment of the nanotube between these two points is relatively straight (as seen from Figure 4.1(c)), which suggests that at least a portion of this nanotube segment is not in direct contact with the substrate. As described in the following paragraph, the local electronic structure of this partially suspended nanotube shows the existence of strongly localized electronic states.

Figure 4.1 (next page). Geometry of a SWCNT adsorbed across a gap between two atomic steps on the Au(111) surface. **(a)** A schematic representation of the system under study (not to scale). **(b)** STM topography of the nanotube. Au(111) step edges are marked as g_1 and g_2. To the left of point n_1 and to the right of point n_2 the nanotube contains defects, which manifest themselves as protrusions in the topographical image. Tunneling set point: 1.5 V, 10 pA. **(c)** Height profiles taken along lines L_1 and L_2 in (b). L_1 corresponds to the nanotube top, and L_2 to the gold substrate near the nanotube. The profile of the nanotube shows point L is 2.34 Å, a number identical to the Au(111) step height (2.34 Å), lower than point n_2, which suggests that the nanotube touches the bottom of the Au trench at point L. The nanotube profile between points L and R is relatively straight, which suggests that part of the nanotube is suspended above the substrate between these points.

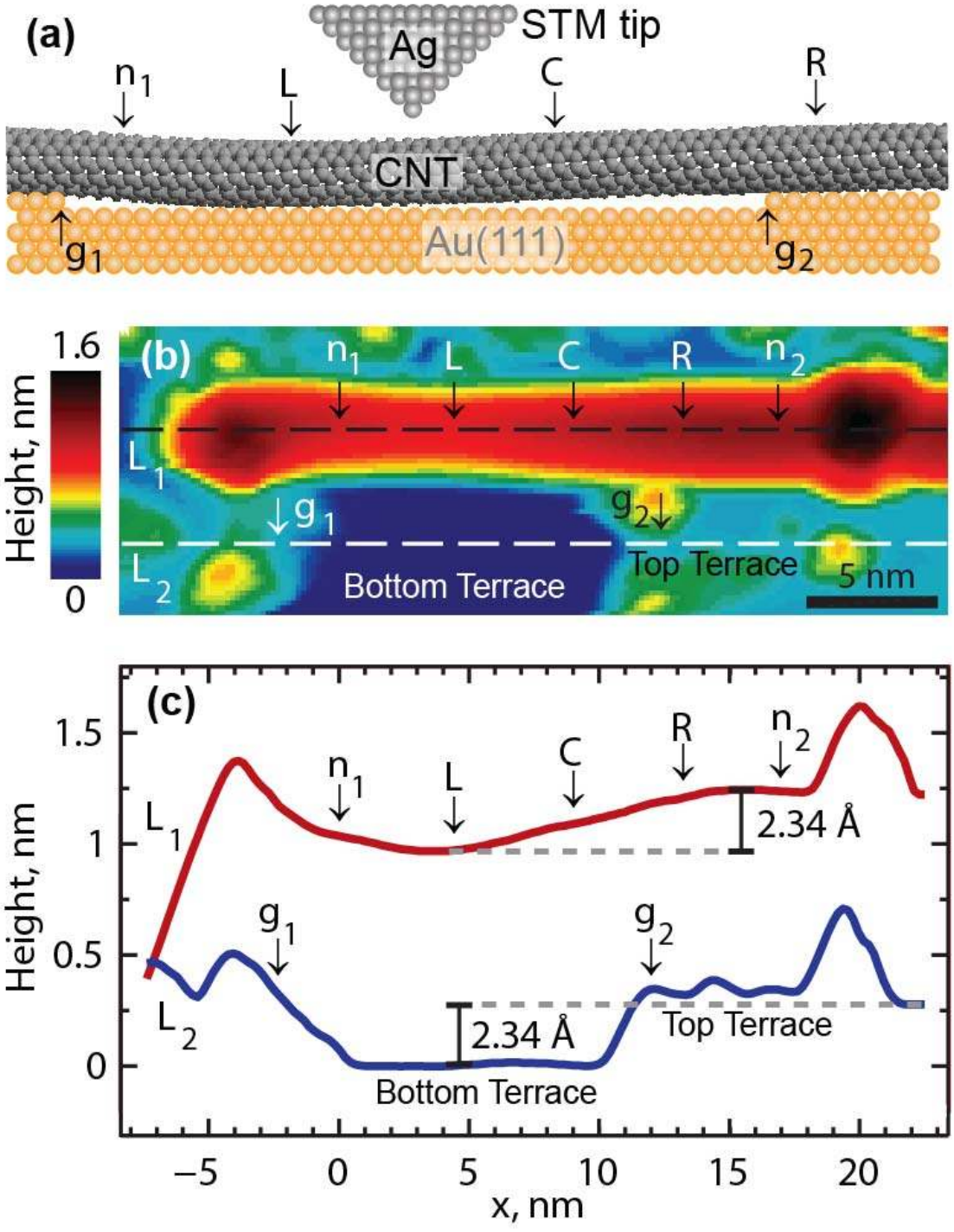
(a)
Ag
STM tip
n1
L
C
R
CNT
Au(111)
g1
g2
(b)
1.6
Height, nm
0
n1
L
C
R
n2
L1
g1
g2
L2
Bottom Terrace
Top Terrace
5 nm
(c)
1.5
1
0.5
0
Height, nm
2.34 Å
2.34 Å
Top Terrace
Bottom Terrace
−5
0
5
10
15
20
x, nm

As shown in Figure 4.2, the voltage-dependent DOS of the nanotube from Figure 4.1(b) is considerably more structured than that of nanotubes on Au terraces (Figure A.2(b)). However, for every spatial location mapped in Figure 4.2, the origins of the observed electronic states can be similarly traced to the same sequence of states, the most visible states being H_1-type (derived from the valence band), E_1-type (derived from the conduction band), and E_2-type (derived from the band immediately above the conduction band). For example, in the center section of the nanotube, these bands correspond to states $H_{1,1}$, $E_{1,1}$ and $E_{2,1}$. In points L and R (where the nanotube makes a contact with the Au surface), the electronic bands (levels E_n^L and E_n^R [these states coalesce with states E_n^{**} in Figure 4.2] together with their valence-band counterparts H_n^L and H_n^R) are rigidly shifted up in energy by 200-250 meV, as compared to states $H_{1,1}$, $E_{1,1}$ and $E_{2,1}$ in the center section of the nanotube. The band bending observed in points L and R is explained in a straightforward manner by the charge transfer[20] between the nanotube and Au substrate caused by the mismatch in their effective workfunctions.[19] This mismatch is clearly seen for the suspended section of the SWCNT, which is not subject to direct charge-transfer interaction with the Au surface. For the suspended section, the bias voltages corresponding to the onsets of conduction are asymmetric (~0.5 V for positive voltages and ~-0.7 V for negative voltages) suggesting that the SWCNT workfunction (4.8 eV[20]) is ~100 meV higher than the effective

workfunction of the Au substrate. (This number is lower than the workfunction of the pristine Au(111) surface [5.3 eV] apparently due to the direct proximity of a Au atomic step running along the SWCNT, as described in Figure A.4).

The upshifts of electronic bands seen at points *L* and *R* are thus explained by partial electron transfer from the Au substrate to the nanotube, compensating somewhat for the mismatch of the workfunctions. Electronic levels E_1^* and H_n^* to the left of point *L*, as well as levels E_n^{**} and H_1^{**} to the right of point *R*, are shifted further up, as expected for a SWCNT section in a more extended contact with the Au surface. Overall, the bandgap of the nanotube does not change appreciably, and no new mid-gap states appear, suggesting that the spatially-dependent DOS in Figure 4.2 results primarily from band-bending.

Electrons propagating along the suspended part of the nanotube are repelled by the potential-barriers caused by local band bending in points *L* and *R*, which results in electron confinement and formation of a quantum dot (QD) in the suspended section of the nanotube. The electron confinement is easily identifiable in Figure 4.2, with three sets of particle-in-a-box states $E_{1,n}$, $E_{2,n}$ and $E_{3,n}$ (n=1, 2) derived from three different electronic bands E_1, E_2 and E_3 (states derived from band E_3 are only visible in the suspended section of the nanotube, apparently due to the enhanced DOS produced by the confinement). The spatial behavior

of these states is further clarified in Figure 4.3: spatial distributions of states $E_{1,1}$, $E_{2,1}$ and $E_{3,1}$ show single maxima in the QD center, whereas states $E_{1,2}$, $E_{2,2}$ and $E_{3,2}$ each show a node in the QD center. This spatial structure identifies states $E_{1,1}$, $E_{2,1}$ and $E_{3,1}$ as ground electronic states of the three progressions, while states $E_{1,2}$, $E_{2,2}$ and $E_{3,2}$ correspond to single-node excited states. Each of the three state progressions is truncated at n=2, because only these states lie lower in energy than the height of the confining potential (~200 meV, estimated from $E_1^R - E_{1,1}$). States E_n^L and E_n^R as well as states H_n^L and H_n^R are more strongly localized than the QD states (the spatial extents of states H_1^L and H_1^R, somewhat exaggerated by the tip-convolution effects, are shown in Figure 4.3, bottom curves), which means that single-node excited states associated with states E_n^L, E_n^R, H_n^L and H_n^R cannot be observed because these states cannot be confined by the band bending observed in Figure 4.2. Indeed, due to their localized nature, such states would have to lie higher in energy than those of $E_{1,n}$ and $E_{2,n}$, above the confining potential barrier.

Close inspection of spectroscopic peaks associated with individual electronic states reveals fine structure, which is particularly pronounced for the localized occupied states, as shown in Figure 4.4(a) (states H_1^*, H_1^L, H_1^R and H_1^{**}). The onset of each spectrum shows a central peak accompanied by two overtones on either side of the peak (these are seen either as peaks or shoulders). For all spectra, the lower energy overtone is ~ 72 mV below the main peak, whereas the higher energy overtone is

~108 mV above the main peak. Similarly to the occupied states in Figure 4.4(a), fine structures are also observed for states $E_{1,1}$ and $E_{2,1}$ (Figure 4.4(b)). The fine structures of the $E_{1,1}$ and $E_{2,1}$ states are less pronounced than those of the occupied states in Figure 4.4(a), but similar overtone spacings are observed, the visibility of these features being somewhat location-dependent: 108±4 meV overtones (seen as a side-peak for $E_{1,1}$ and a shoulder for $E_{2,1}$) are clearly observed on top of the nanotube (Figure 4.4(b), second curve from the top), while the ~72±4 meV overtones are more pronounced slightly away from the nanotube centerline (Figure 4.4(b), top curve). States other than $E_{1,1}$ and $E_{2,1}$ may also possess vibrational structures, which may be obscured by the complex DOS pattern in Figure 4.2.

The similarity in the spacings of the fine features observed at both positive and negative voltages in Figure 4.4 suggests that these fine features are not of electronic origin – in that scenario one would expect the fine structures to be different because of the different extents of localization observed for these states (states from Figure 4.4(a) as contrasted to states $E_{1,1}$ and $E_{2,1}$). Indeed, Figure 4.3 shows that states H_1^L and H_1^R are more strongly localized than the QD states $E_{m,n}$, and the different degree of localization would have produced different electronic splittings. The fine structures observed in Figure 4.4 must therefore be associated with vibrational excitation, analogous to the results reported for the STS spectroscopy of individual molecules.[21-24]

Vibrational patterns typically observed in STS spectroscopy on individual molecules are closely related to the changes in the molecular geometry caused by the transition to a transiently charged molecular state (anionic or cationic, depending on the bias polarity) that occurs during an electron tunneling event.[25] The precise patterns could either follow Frank-Condon patterns for displaced oscillators,[26] or have more complex structures when the transiently charged molecular state shows Jahn-Teller activity.[27-28] Spectra shown in Figure 4.4 can be analyzed analogously, since the electron confinement observed in Figure 4.2 effectively creates localized molecular-sized electronic orbitals inside the SWCNT.

To identify the types of vibrations that can be excited in electron tunneling through the quantum-confined nanotube states, we thus need to identify the nature of structural distortions occurring in the presence of an extra localized charge in the nanotube. Importantly, neutral species of very short (a few nanometers) SWCNTs are predicted to show a variety of structural distortions, the exact structure being sensitive to the nanotube chirality,[29] length,[30] diameter,[31] and termination.[31] In particular, calculations for finite-length armchair nanotubes (possessing finite non-zero bandgaps) have shown structures combining Clar and/or Kekulé patterns.[30, 32] Chainlike distortions appearing as trans-poly-acetylene chains oriented roughly along the nanotube axis were predicted for infinite chiral nanotubes.[29] Similar bond alternations in polycyclic

aromatic hydrocarbon molecules are argued to be related to the "distortivity" of π-electrons working against the stabilizing influence of σ-bonds,[33] which tends to result in Kekuléan distortions.[34] Such distortions can be generally expected to be more pronounced for more strongly localized states, with bond alternation on the scale of ~2 picometers expected for short achiral[35] and chiral[36] tubules (a few to several nanometers in length). In addition to the bond alternation, a short-range rippling-type of distortion of SWCNT surfaces was also found to occur in theoretical calculations.[36]

Figure 4.2 (next page). STS signal (obtained by measuring differential conductance, dI/dV, using the lockin-technique) as a function of the x coordinate [identical to that in Figure 4.1(c)] and sample bias voltage. (STS signal serves as a measure of the local density of electronic states.) The spatial range corresponds to the part of line L_1 contained between points n_1 and n_2 in Figure 4.1(b) and Figure 4.1(c). Positive voltages correspond to unoccupied electronic states, while negative voltages correspond to occupied states. Vertical dashed lines at $x = 4.4\,nm$ and $13.3\,nm$ (corresponding to points L and R in Figure 4.1) indicate positions of the nanotube contact with the Au substrate where the nanotube electronic bands are bent due to the charge transfer between the nanotube and Au. [The charge transfer is caused by a workfunction mismatch.] These points of contact reveal themselves through the appearance of shifted electronic levels E_n^L (and H_n^L) and E_n^R (and H_n^R), as compared to the bands in the region between points L and R. The region in between points L and R ($x = 4.4\,nm$ and $13.3\,nm$) forms a quantum dot (QD) with three sets of particle-in-a-box states $E_{1,n}$, $E_{2,n}$ and $E_{3,n}$ (n=1, 2). All QD energy levels are marked with horizontal dashed lines. Electronic levels E_1^* and H_n^* to the left of point L, as well as levels E_n^{**} and H_1^{**} to the right of point R are shifted further up. All data were measured along the nanotube centerline. Tunneling set point: 1.5 V, 0.1 nA.

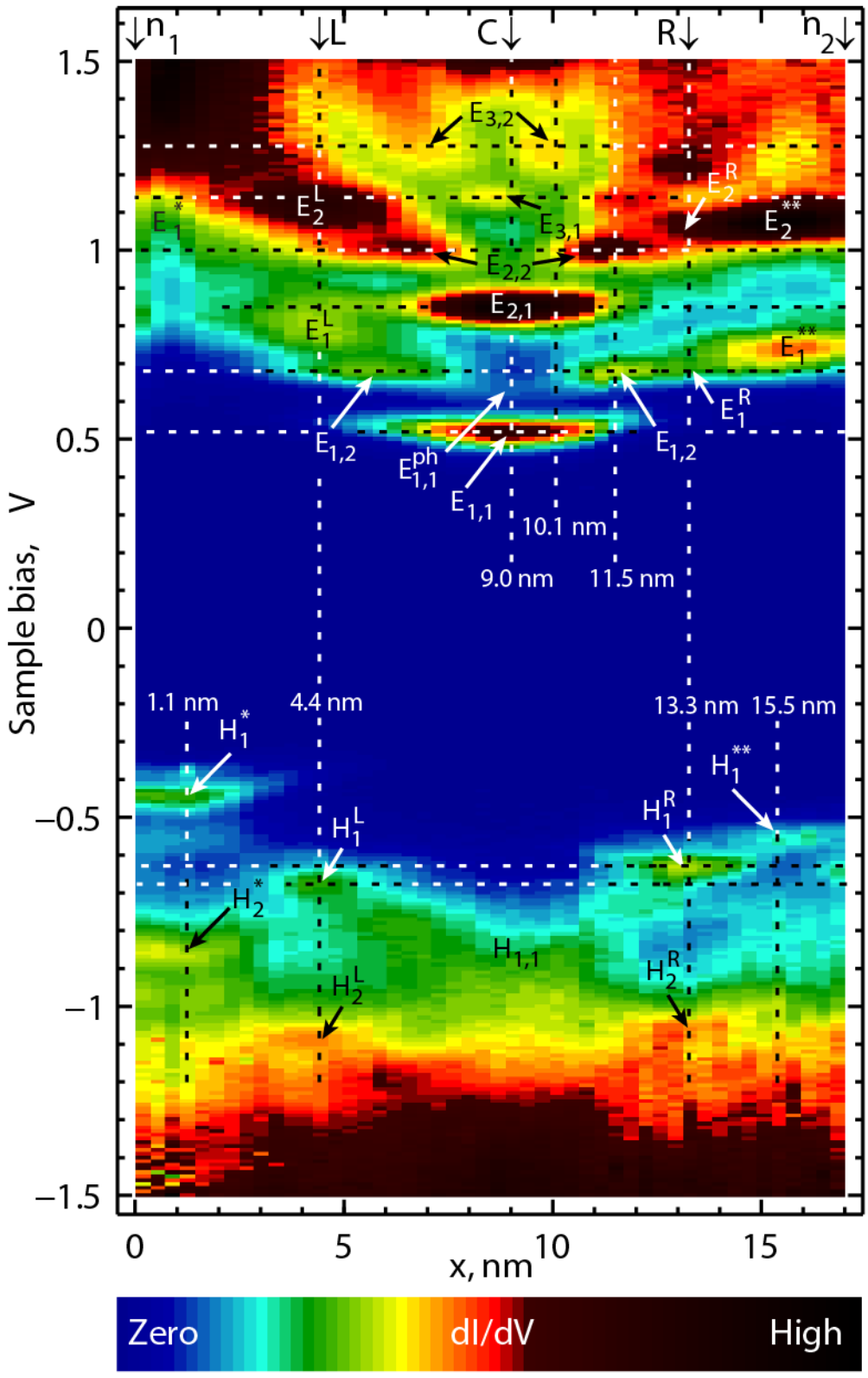
↓n1
↓L
C↓
R↓
n2↓
1.5
1
0.5
0
−0.5
−1
−1.5
Sample bias, V
0
5
10
15
x, nm
E3,2
E2L
E2*
E3,1
E2R
E2**
E2,2
E2,1
E1L
E1**
E1,2
E1ph1,1
E1,1
E1R
E1,2
10.1 nm
9.0 nm
11.5 nm
1.1 nm
4.4 nm
13.3 nm
15.5 nm
H1*
H1L
H1**
H1R
H2*
H1,1
H2L
H2R
Zero
dI/dV
High

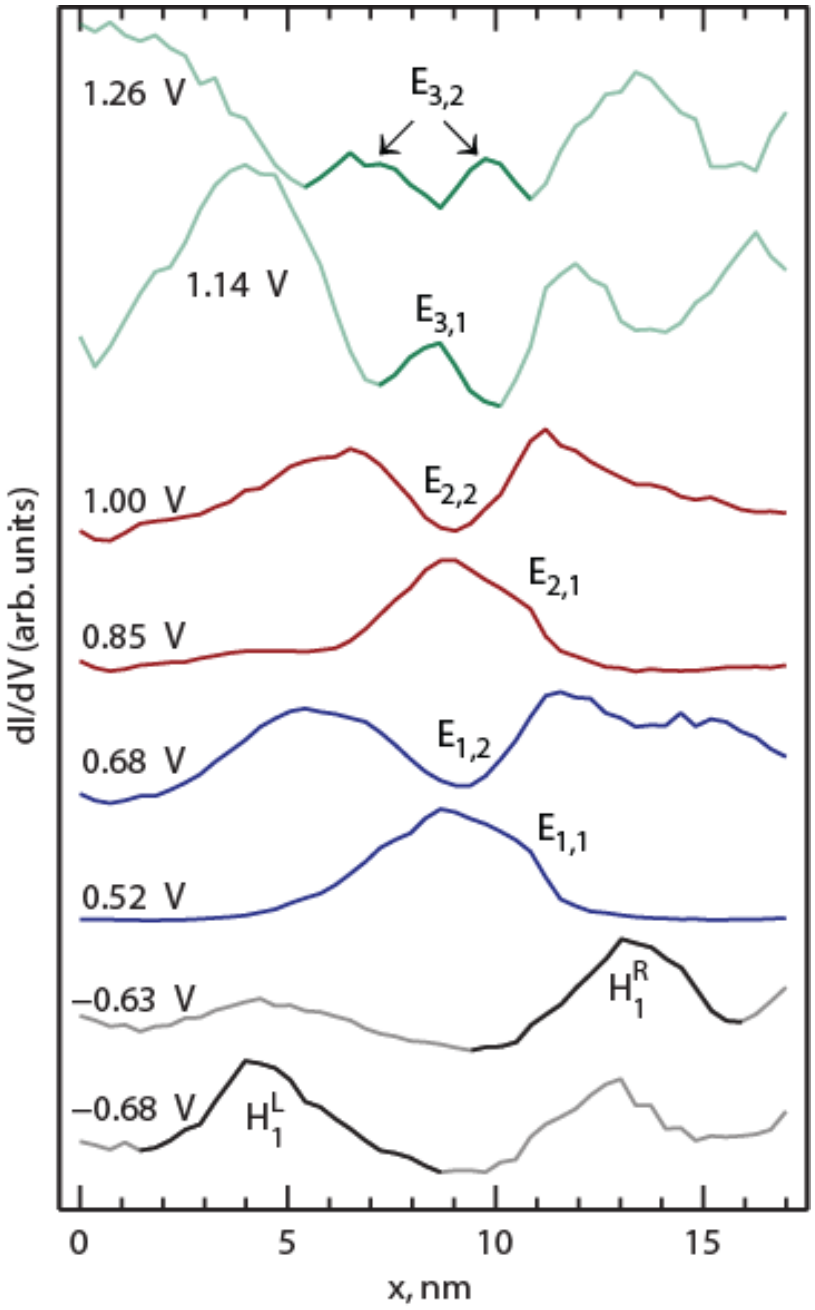

Figure 4.3. Cross-sections of the data from Figure 4.2 along the horizontal dashed lines showing the spatial behavior of $E_{m,n}$ states of the QD from Figure 4.2. Spatial distributions of states $E_{1,1}$, $E_{2,1}$ and $E_{3,1}$ show single maxima in the QD center, whereas states $E_{1,2}$, $E_{2,2}$ and $E_{3,2}$ each show a node in the QD center. States H_1^L and H_2^R are more strongly localized as compared to the QD states $E_{m,n}$. Individual cross-sections are offset for clarity.

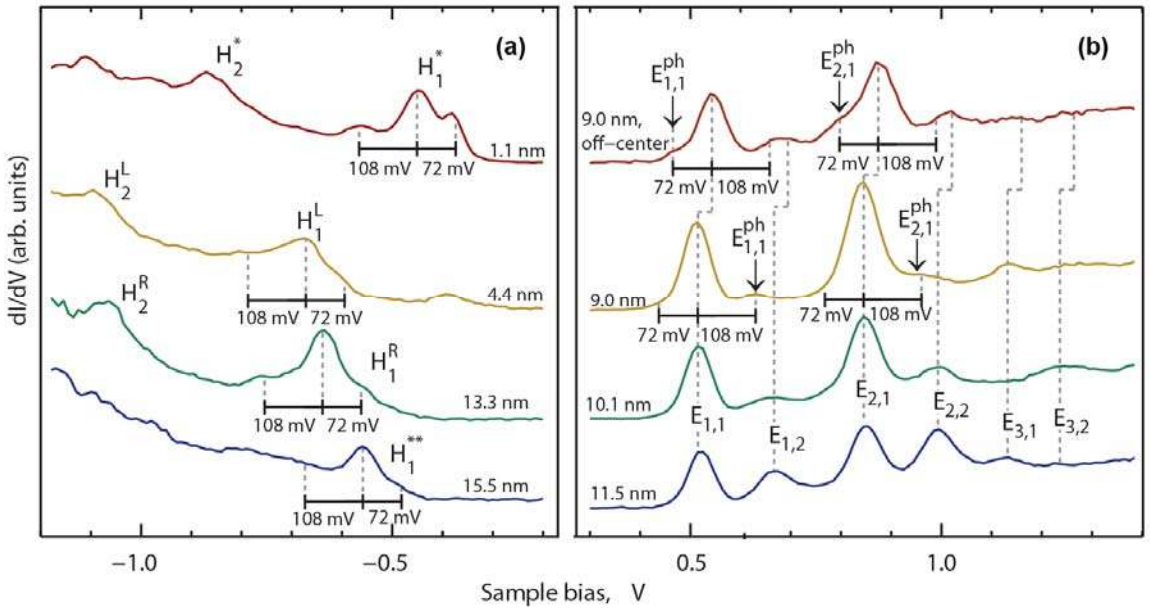

Figure 4.4. Cross-sections of the data from Figure 4.2 taken along the vertical dashed lines in Figure 4.2, showing DOS as functions of the sample bias voltage (the corresponding x-coordinates of these cross-sections are also shown). Individual cross-sections are offset for clarity. All spectra were measured along the nanotube centerline except the top curve in (b).

(a) Occupied states that correspond to several distinct locations where the nanotube makes contact with the Au substrate. The onset of each spectrum shows a peak accompanied by two overtones (seen either as peaks or shoulders). For all spectra, the lower energy overtone is ~ 72 mV below the main peak, whereas the higher energy overtone is ~108 mV above the main peak.

(b) Unoccupied states. In addition to three spectra measured roughly on top of the nanotube, a spectrum measured at $x = 9\,nm$ slightly away from the nanotube centerline is also shown (top curve, all features contained in this curve are upshifted due to the larger fraction of the bias voltage dropped across the nanotube diameter). The manifold of $E_{m,n}$ states is seen at positive voltages as peaks. Similarly to the occupied states in (a), states $E_{1,1}$ and $E_{2,1}$ contain fine structure, which is most clearly seen for the two spectra measured at $x = 9\,nm$: the top curve shows overtones at ~ 72 mV below the corresponding $E_{1,1}$ and $E_{2,1}$ peaks; for the spectrum measured along the nanotube centerline (second from top) the main $E_{1,1}$ and $E_{2,1}$ peaks are accompanied by a side-peak and a shoulder correspondingly, both ~108 mV higher than the corresponding main peaks.

In contrast to neutral SWCNTs, calculations of anionic species for short tubules show significantly reduced bond alternation,[35] which can be interpreted in terms of the reduced "distortivity" of π-electrons in this state. Similar results were also obtained for the excitonic states in chiral nanotubes.[36] We therefore expect a similar behavior in the present case: a reduction of the overall local deformation of the nanotube for the charged state of the QD.

To identify the nature of vibrational modes contained in the spectra of Figure 4.4, we need to convert the voltage scale to the correct energy scale by taking into account the finite voltage drop inside the SWCNT. As shown in the discussion following Figure A.5, the average potential inside the nanotube is ~10±1% of the total bias voltage, so that the correct energy scale is calculated for the present system by multiplying the total applied voltage by a factor of 0.9±0.01. This gives rescaled peak spacings of 65±4 meV and 103±4 meV for the two vibrational overtones. The first energy is equivalent to 518±32 cm^{-1}, which can be explained by the presence of a rippling deformation of the QD-CNT surface, analogously to the short-range rippling deformation found in the calculated geometries of chiral SWCNTs.[36] Indeed, the found energy is close to the 559 cm^{-1} energy of the transverse out-of plane-phonons in graphene at the K-point of the Brillouin zone (nominal optical and acoustical branches intersect at this point),[37] which could

generate rippling with a spatial periodicity determined by the K-point wavevector.

To identify the phonon mode associated with the higher-energy sideband, we calculate the corresponding vibrational energy as 65 + 97 meV = 162±6 meV (assuming that the onsets of conduction in our spectra correspond to zero-phonon peaks). This is equivalent to 1296±48 cm^{-1}, which is close to 1378 cm^{-1}, the energy of the D-band Kekulé modes[31] calculated for the present nanotube, which has a skeletal diameter of ~0.7 nm, based on the measured topographic height of ~1.0 nm (Figure 4.1(c)). Both of the found vibrational energies are red-shifted with respect to the corresponding expected values, which could be partially explained by the reduced bond order of the cationic and anionic states of the nanotube QD observed in the STS spectra of Figure 4.2 and Figure 4.4. The presence of Kekulé modes in our spectra suggests a Kekuléan in-plane dimerization of carbon atoms on the nanotube surface localized on and around the QD section of the nanotube.

In addition to the identified K-point-transverse out-of plane-phonons and Kekulé modes, other unresolved modes are likely present in the spectra of Figure 4.4. In particular, excitation of low energy modes are possible, including the radial breathing mode,[38] and center-of-mass motion perpendicular to the Au(111) surface,[26] which in the present case would involve bending of the nanotube. Excitation of these, as well as other low energy and/or weakly coupled modes, is likely the cause of the

substantial widths of peaks in the spectra of Figure 4.4.[23] Further, the spectra may also be affected by non-adiabatic effects resulting from the vibronic inter-valley coupling, analogously to the Jahn-Teller activity identified recently in STS spectra of porphyrin molecules.[27-28]

The present work sheds light on one of the fundamental mechanisms determining the influence of local disorder on electron transport through SWCNTs: Figure 4.2 suggests that the energetically sparse progression of localized electronic states, created in a short SWCNT segment by a disorder potential, would be out of resonance with the conduction band (or valence band) states of the rest of the nanotube. This means that resonant electron transmission through such SWCNT segments would have to occur through the vibrational overtones of the localized electronic states (or, more generally, vibronic states). The precise structure of the manifold of such vibronic states also determines the rate of energy relaxation for charges traversing the SWCNT segments with localized electronic states, which determines the dynamics of charge trapping/de-trapping.

4.2. Experimental Details

Experiments were carried out in a home-built ultra-high vacuum (UHV) cryogenic STM system. All imaging and spectroscopic measurements were carried out at a temperature of 15 Kelvin using electrochemically-etched silver tips. SWCNTs (obtained from Sigma-Aldrich) were deposited

on Au(111)/mica substrates using the in-vacuum “dry contact transfer” (DCT) method, analogous to the approach demonstrated recently in other STM studies of carbon nanotubes.[39-40] Figure A.1 shows representative STM images of several SWCNTs on a Au(111) surface.

4.3. Bridge to Chapter V

This chapter showed that the novel CCC UHV STM described in this dissertation performed at a level that allowed one to map out the vibronic states of a CNT. In Chapter V, it will be shown that our CCC UHV STM was able to spatially map out the delocalized quantum-confined states and localized sub-bandgap states due to non-stoichiometry in a PbS quantum dots.

CHAPTER V

SPATIAL MAPPING OF SUB-BANDGAP STATES INDUCED BY LOCAL NON-STOICHIOMETRY IN INDIVIDUAL LEAD-SULFIDE NANOCRYSTALS

This work was previously published with coauthors Dmitry A. Kislitsyn, Christian F. Gervasi, Thomas Allen, Peter K.B. Palomaki, Jason D. Hackley, Ryuichiro Maruyama, and George V. Nazin in the *Journal of Physical Chemistry Letters*, 5, 3704-3707 (2014), dx.doi.org/10.1021/jz5019465,

5.1. Introduction

Recently, thin films composed of lead chalcogenide colloidal semiconducting nanocrystals (NCs) have emerged as a promising class of photovoltaic materials that allow great flexibility in controlling their properties by means of tailored synthesis, processing and film deposition.[1-2] Further, quantum confinement effects in NCs can be exploited to control their photoexcitation dynamics in order to achieve multiplication of photo-generated carriers[3-7] and/or hot-electron extraction,[8] which may enable solar cells with efficiencies in excess of the

Shockley–Queisser limit.[9] While substantial progress has been made towards improving the efficiency of NC-based photovoltaic devices, with recent reports of efficiencies above 8%,[10-11] the microscopic picture of the fundamental physical processes of photo-generation and charge transport in NC films remains incomplete. One of the important outstanding questions is the impact of the NC surface chemistry on the electronic properties of NCs. Imperfections in surface passivation or stoichiometry are thought to cause sub-bandgap states, which can have a significant impact on electron–hole recombination.[12] While evidence for such surface states was found in recent photoluminescence studies of as-synthesized lead chalcogenide NCs,[13-14] fabrication of functional photovoltaic devices may introduce further surface imperfections as it often involves a sequence of synthetic and processing steps including surface ligand exchange[15-16] and (in some studies) thermal annealing[17-18] that can both affect the nanocrystal surface chemistry. Indeed, sub-bandgap states have been identified in processed NC films using a variety of techniques, including photoluminescence;[14] a combination of current-based deep level transient spectroscopy, thermal admittance and Fourier transform photocurrent spectroscopies;[19] Scanning Tunneling Spectroscopy (STS);[20] and photocurrent measurements in NC-based field-effect transistor devices.[21] Despite the insights provided by such studies, they do not provide direct information about the local chemical and spatial structures of surface states. This information is critically

important for addressing the remaining uncertainties regarding the nature of such surface states, especially given the diversity of atomic sites present on NC surfaces arising from variations in ligand coverage and the presence of different crystallographic facets.

Here we report, for thfe first time, the spatial mapping of sub-bandgap states in individual PbS NCs using a combination of Scanning Tunneling Microscopy (STM) and Scanning Tunneling Spectroscopy (STS). PbS NCs deposited on Au(111) surfaces were annealed in ultra-high vacuum at 170 °C to remove surface ligands (see Experimental Details). Ligand-free NCs were targeted because they are unaffected by the uncertainties associated with different possible ligand shell configurations, and therefore serve as a useful model amenable to theoretical simulations.[22-24] NCs in devices are also often stripped of ligands to increase inter-particle electronic coupling.[25] In total, we studied 16 individual PbS NCs. The NCs were annealed at progressively higher temperatures until well-defined and reproducible NC topographies consistent with complete removal of ligands were obtained (Figure B.1; see Appendix B for supplemental figures for this chapter). The apparent heights of thus prepared NCs are typically 1-2 nm, while their lateral dimensions are 2-5 nm with width/height ratios being typically 2:1 to 3:1, which suggests that the NC shapes change significantly upon annealing. Importantly, annealed ligand-free NCs display topographic

features, such as crystal facet steps and edges, showing visible angles consistent with different crystallographic directions (Figure B.1).

STS spectra of individual NCs were obtained by measuring the differential tunneling conductance dI/dV as a function of the applied bias voltage (see Experimental Details).[26] The recorded dI/dV signal serves as a measure of the local density of states (DOS). STS spectra of annealed NCs show progressions of occupied and unoccupied states separated by apparent band gaps of different magnitudes (Figure 5.1). All spectra in Figure 5.1 show similar progressions of states H_1 (highest occupied state), $E_{1,1}$ (lowest unoccupied state), $E_{1,2}$ and E_2 (both unoccupied states), with individual state energies varying for different NCs. The STS spectra shown in Figure 5.1 appear to be consistent with the DOS spectra calculated for stoichiometric ligand-free lead-chalcogenide NCs,[22-24] where the DOS was found to be dominated by quantum-confined electronic states derived from the conduction and valence bands. These calculations show that lowest-energy electronic states in such NCs exhibit roughly s and p overall spatial symmetries, modulated on the atomic scale by their corresponding Bloch wave functions.[22] However, as we show below, the nature of states $E_{1,1}$ and $E_{1,2}$ in Figure 5.1 is different.

A common feature of all spectra in Figure 5.1 is that states $E_{1,1}$ and $E_{1,2}$ are separated by ~0.2 V in all cases. Identifying the nature of states $E_{1,1}$ and $E_{1,2}$ is important because the lowest-lying unoccupied

states are primarily responsible for the photophysical and electron transport properties of NC-based materials.[21] We note that overtones $E_{1,2}$ are unlikely to be caused by vibrational excitation of NCs[27] due to their relatively large energetic spacing, inconsistent with the vibrational energy scale of PbS.[28] This energetic spacing also appears too large to be explained by electronic splitting (caused by the NC anisotropy) of the different L-valleys in the Brillouin zone.[29] Similar spectral features observed in STS studies of electrochemically-grown PbS NCs were attributed to particle-in-a-box-like states.[30] According to this interpretation, state $E_{1,1}$ should correspond to the ground state, state E_2 should correspond to the excited state varying along the *z*-direction, and $E_{1,2}$ is attributable to excited states varying in the x-y plane. Spatial mapping of NC DOS shows that the nature of $E_{1,n}$ states in the present case is more complex, as described below.

To understand the nature of the $E_{1,n}$ bands, we have carried out DOS mapping for several NCs. Representative data for one such NC (referred to as NC_1 in the following) are presented below. STM topography of NC_1 shows a series of steps angled at 120° degrees with respect to each other (Figure 5.2(a,b)). This observation suggests that these directions correspond to the <110> crystallographic directions, while the top surface of NC_1 should correspond to the (111) crystallographic orientation, based on the stability of these facets established in TEM studies of restructuring of PbS NCs under similar

temperatures in vacuum.[31-32] A cross-section of the topography for NC_1 (Figure 5.2(c)) shows that the top facet, oriented at ~10° with respect to the Au(111) surface, is relatively flat with corrugation at the angstrom-scale, consistent with complete removal of ligands.

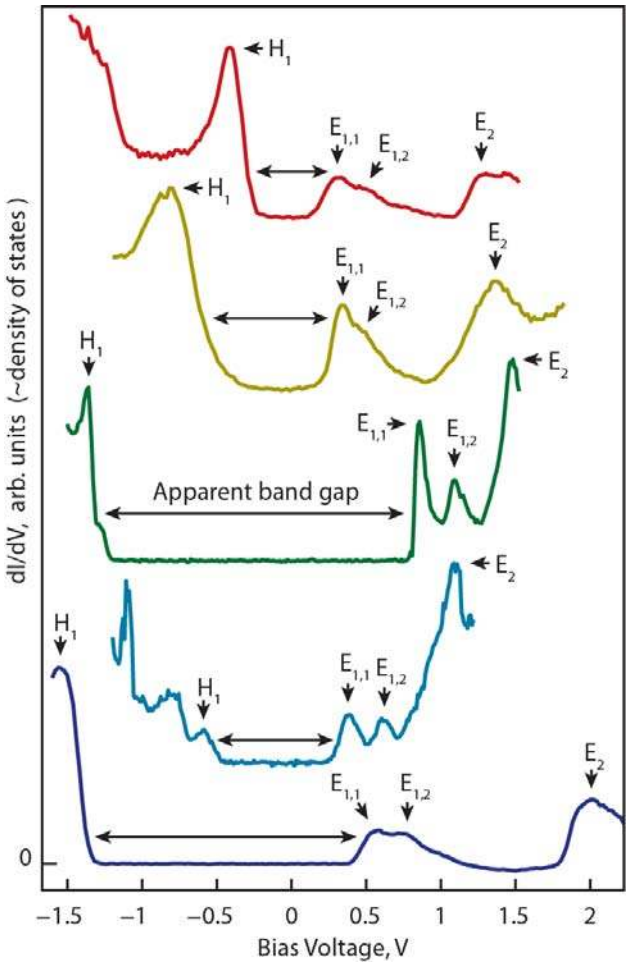

Figure 5.1. Representative dI/dV spectra for five PbS NCs (set point voltages and currents range from 1.2 V to 2.5 V, and 10 pA to 30 pA for the spectra shown). The bias voltage effectively serves as the energy scale (see, however, discussion associated with Figure B.2 for a more complete description of the relationship between the bias voltage and energy). Occupied and unoccupied states are indicated by arrows and marked with an 'H' and 'E' for electrons and holes respectively. The apparent band gaps for each of the NCs are marked with double sided arrows.

A STS spectrum measured on top of NC_1 (Figure 5.2(d)) shows an electronic DOS with a ~0.8 eV bandgap formed by states $E_{1,1}$ and H_1. Additional states E_2 (1.3 eV) and H_2 (-1.4 eV) are found at higher voltages. The lowest unoccupied state $E_{1,1}$ shows a side-peak ($E_{1,2}$), which is observed in most annealed NCs (Figure 5.1). STS spectra measured at different locations on NC_1 show considerable variation in state energies and character. To visualize these variations, we recorded a spatial "cross-section" of the electronic DOS along a linear path across NC_1 (Figure 5.3(a)). The resulting DOS cross-section (Figure 5.3(b)) shows quasi-periodic oscillations in intensity for the electronic DOS of states $E_{1,n}$. The spatial variations of all states $E_{1,n}$ (Figure 5.3(b)) are nearly identical suggesting similar origins for the main peak and its sidebands. The spatial modulation of states $E_{1,n}$ occurs with an average period of ~0.9 nm, a large number as compared to the typical inter-atomic distances along the PbS(111) surface, which means that this modulation is not caused by the elemental contrast between Pb and S lattice sites that could be expected on a defect-free PbS surface.[33] In accordance with this assessment, the highest occupied state H_1, which is expected to be comprised of sulfur 3p atomic orbitals,[24] is not visibly modulated. The only identifiable variation of the H_1 state is a minor change in H_1 energy (from -0.8 V to -0.7 V and back to -0.8 V) as the scan progresses along the path in Figure 5.3(a) from P_1 to P_5.

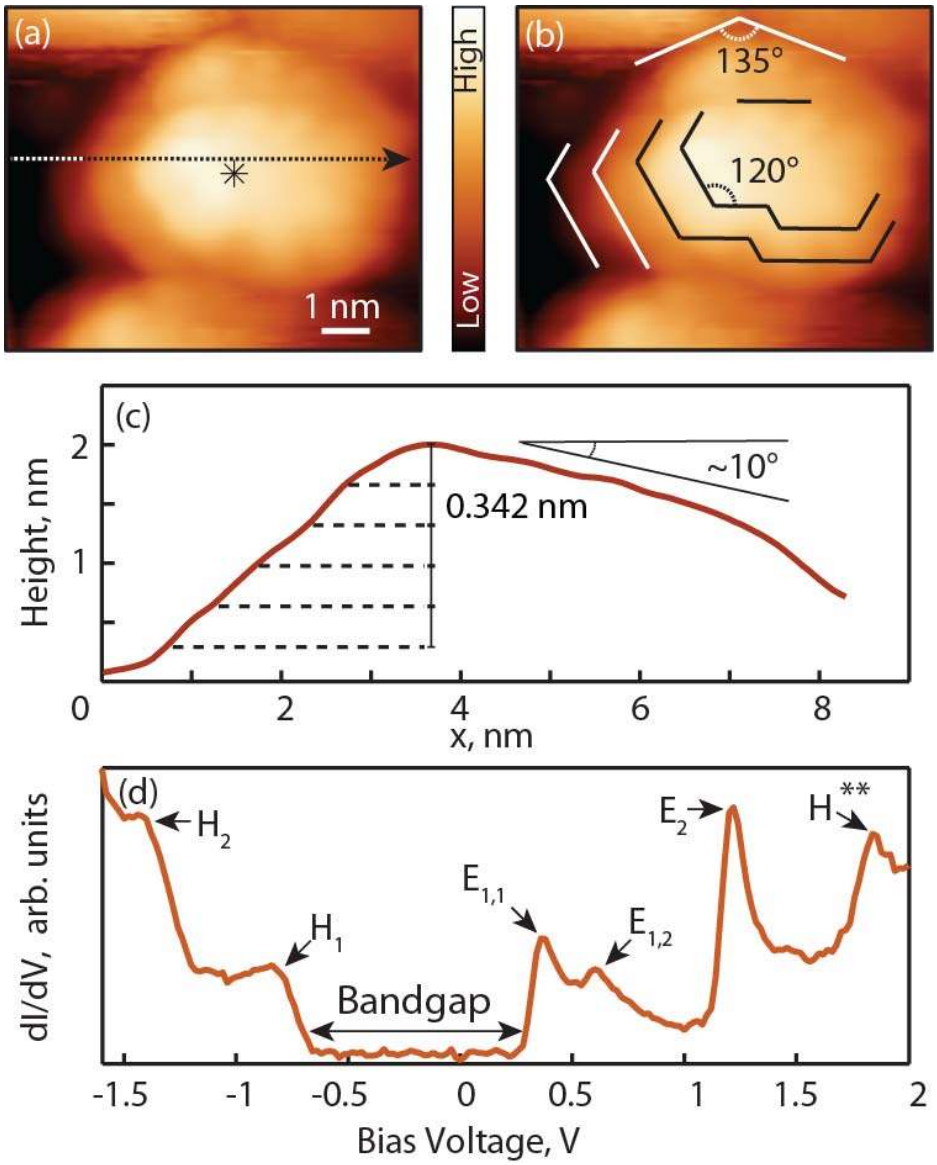

Figure 5.2. STM/STS characterization of a representative nanocrystal NC_1. **(a)** STM topography image of NC_1 [set point 1.0 V, 1.0 pA]. **(b)** Topographical features attributable to step edges oriented along specific crystallographic directions. The majority of features indicate 120° angles, which suggests that the top facet of NC_1 corresponds to a {111} plane. **(c)** A cross-section of the topography [path indicated by the arrow in (a)] showing that the top facet of NC_1 is at a small angle with respect to the Au(111) surface. Individual steps are marked with dashed lines, with the step height (0.342 nm) corresponding to the distance between the sulfur {111} planes. **(d)** A representative STS spectrum [set point 2.0 V, 15 pA] measured at the location marked by the star in (a). Prominent occupied and unoccupied states are marked with an 'H' and 'E', respectively.

The trajectory of the H_1 energy variation roughly follows the NC topography (high topographic locations correspond to the lower (in absolute value of applied voltage) onsets of resonant tunneling through H_1), which is explained by the variation of the voltage drop inside the NC.[36] A smaller variation in the tunneling onset energy is found for the unoccupied states, which is attributable to the different work-functions of the tip and sample, as explained further in the Appendix B. Insight into the nature of states $E_{1,n}$ can be gained from a detailed analysis of their spatial behavior, as discussed in the following.

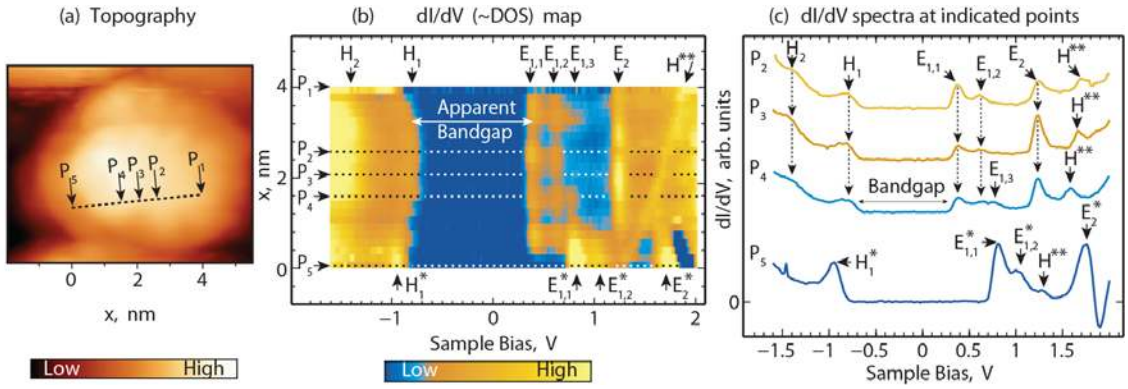

Figure 5.3. Spatial DOS (STS) mapping across nanocrystal NC_1. **(a)** Topographic image [set point 1.0 V, 1 pA] showing the path of mapping (points P_1 through P_5). **(b)** Density of states [set point 2.0 V, 10 pA] as a function of bias voltage and position x along the path shown in (a). **(c)** Individual STS spectra from (b) measured at points P_2 through P_5. Occupied and unoccupied states are marked 'H' and 'E' respectively in both (b) and (c). Spectral feature H^{**} corresponds to "reverse" tunneling[34-35] through a localized occupied state outside of the mapping path.

To characterize the spatial behavior of the NC_1 electronic structure, we recorded STS spectra on a two-dimensional grid of (32 by 32) points covering the spatial range shown by the yellow rectangle in Figure 5.4(a). In the overall bias voltage range sampled in these spectra, several spatial DOS patterns associated with distinct electronic states shown in Figure 5.3 are identified (Figure 5.4). These patterns show that the distributions of individual electronic states across NC_1 are highly inhomogeneous. States $E_{1,n}$ are primarily concentrated in the left and bottom parts of NC_1 (locations 1-9 in Figure 5.4(b), 0.35 V) in the vicinity of the steps observed in the STM topography (Figure 5.4(a)). The DOS intensity corresponding to these states forms stripe-like features running through locations 1-9 in Figure 5.4(b). These four stripes correspond to the four DOS peaks observed along the x-coordinate for the $E_{1,1}$ states in Figure 5.3(b). All states $E_{1,n}$ have very similar two-dimensional spatial distributions of their DOS, as can be seen in Figure 5.4(b), consistent with the one-dimensional scan of Figure 5.3(b). Figure 5.4(b) shows that the "stripes" are localized in the vicinity of the NC_1 step edges (highlighted in the bottom maps of Figure 5.4(b)). In contrast, unoccupied state E_2 is delocalized throughout NC_1, and is primarily concentrated in the upper right part of NC_1 (locations 10-15 in Figure 5.4(b), 1.15 V) where no clear topographic steps exist.

Similar distinction between localized states at the onset of tunneling and delocalized states at higher voltages is found for occupied

states: the highest energy state $H_1^{\dagger}$ appearing at -0.58 V (Figure 5.4(c)), is localized (analogously to states $E_{1,n}$) near the step edges, while states H_1 (-0.7 V) and H_2 (-1.4 V) show relatively uniform distributions. The latter are, in fact, even more homogenous than they appear: their apparent DOS in locations 13-15 is suppressed due to the effect of variable voltage drop across the NC described in the discussion of Figure 5.3(b).

Theoretical calculations show that unoccupied states in PbS are formed predominantly by Pb-derived atomic 6p orbitals, whereas occupied states are formed predominantly by S-derived atomic 3p orbitals.[24] According to these predictions, the DOS of states $E_{1,n}$ and E_2, for unpassivated NCs, is carried by surface Pb-atoms, while the DOS of states $H_1^{\dagger}$, H_1 and H_2 is carried by surface S-atoms. The S- and Pb-character of occupied and unoccupied states correspondingly holds true even in the presence of under-coordinated Pb- or S-atoms, which form localized states split-off from the conduction- and valence-bands.[37] Because Pb- and S-atoms located at step edges lack nearest neighbors, they are in under-coordinated environments compared to other surface atoms, and therefore may form sub-band gap states.[38] Localization of states $E_{1,n}$ and $H_1^{\dagger}$ near the step edges, where atomic coordination is disrupted, suggests that these states correspond to sub-bandgap trap states, while the spatially delocalized states E_2, H_1 and H_2 are identified as quantum-confined states derived from the conduction (E_2) and valence

(H_1 and H_2) bands. Consistent with the identification of states $E_{1,n}$ and $H_1^{\dagger}$ as states primarily localized on Pb- or S-atoms respectively, DOS maps for these states (Figure 5.3(b,c)) show complementary intensities in most of locations 1-15. The differences in the spatial distributions of states $H_1^{\dagger}$ and $E_{1,n}$ are attributable to the different spatial distributions of the under-coordinated Pb- and S-atoms, which is likely a result of the different quantities of Pb versus S atoms, as can be expected based on the fact that as-synthesized PbS NCs typically have Pb-rich surfaces.[39-40] Our spectroscopic data corroborates this expectation: the splitting of non-stoichiometric trap states from the main quantum-confined states has been predicted to be larger for NCs with greater non-stoichiometry,[37] and can thus be used as a measure of the degree of local non-stoichiometry. Specifically, on the energy scale, state $H_1^{\dagger}$ appears only 0.12 eV higher than the onset of band H_1 in Figures 5.3(b,c), which is comparable with calculations for states localized at S-atoms within step edges on the stoichiometric PbS(100) surface.[38] In contrast, the energy difference E_2 - $E_{1,1}$ is relatively large: ~0.8 eV. The same trends are observed in the spectra of most other NCs (Figure 5.1) suggesting that the number of under-coordinated Pb atoms is indeed higher than that of under-coordinated S-atoms in the studied NCs. These trends, and their consistency with the theoretical predictions[37] further reinforce our assignment of states $E_{1,n}$ and $H_1^{\dagger}$ as defect states.

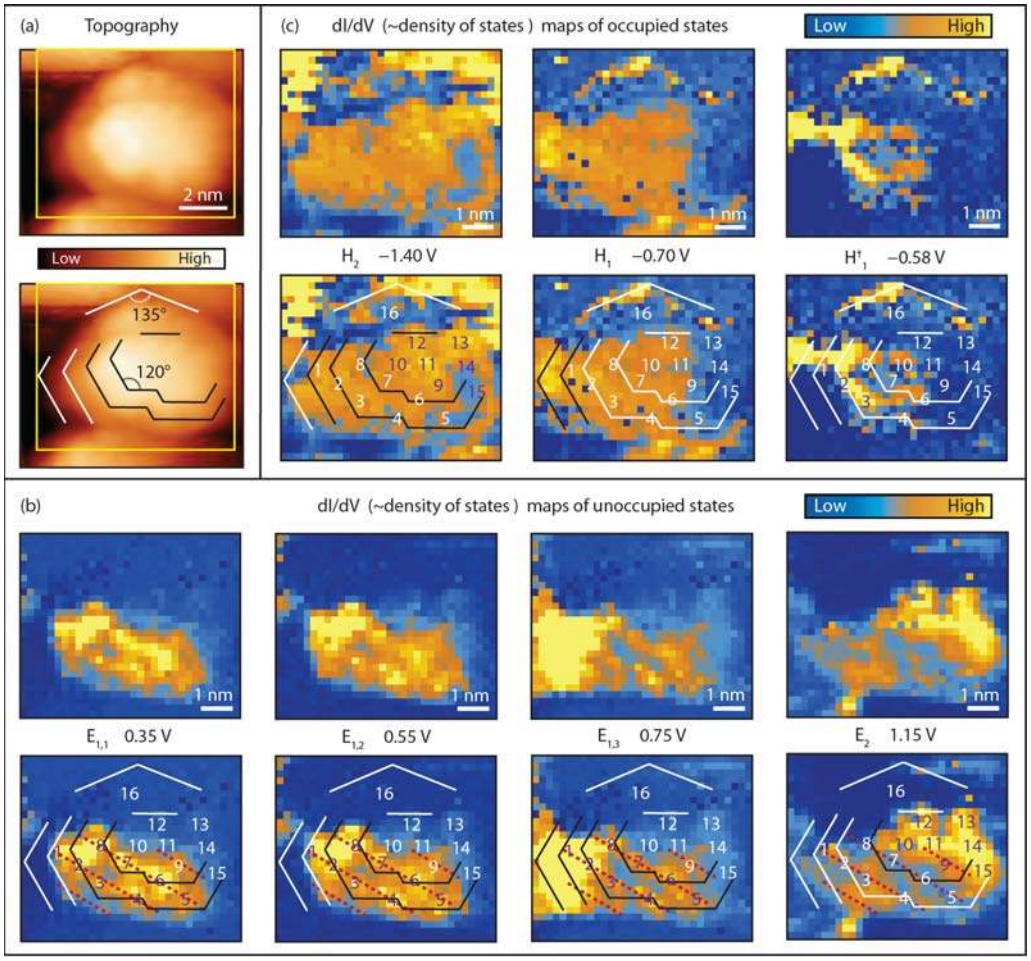

Figure 5.4. **(a)** Topographic images of NC_1 [set point 1.0 V, 1 pA]. Bottom image is marked to indicate step edges with 120° angles oriented along <110> directions, the same set of marks is used in the bottom images of (b) and (c) for reference. **(b)** DOS maps for unoccupied states of NC_1 [set point 2.0 V, 15 pA] measured at the indicated bias voltages. Parallel dashed red lines indicate the apparent orientation of stripe-like features associated with states $E_{1,n}$. **(c)** DOS maps for occupied states of NC_1 [set point 2.0 V, 15 pA] measured at the indicated bias voltages. High intensity signals in the top left and top right of the H_2 map in (c) are attributed to spectral features of nearby NCs. The spatial extent of maps in (b) and (c) corresponds to the yellow rectangle shown in (a). Numbered markers in the bottom images of (b) and (c) [identical for both sets of maps] indicate locations of high DOS intensity for states $E_{1,n}$ (1-9) and E_2 (10-15). Location 16 marks a region with a localized higher energy state [~1.9 V, map not shown], likely corresponding to a smaller NC (with a different crystallographic orientation) that is in the process of merging with NC_1.

Additional support for assignment of states $E_{1,n}$ as trap states is provided by the analysis of their energies in other studied NCs. Inspection of STS spectra of such NCs (Figure 5.1) shows that energy splitting E_2 - $E_{1,1}$ varies among different NCs, but does not show a correlation with their apparent bandgaps $E_{1,1}$ - H_1 (Figure B.3). This is contrary to what would be expected if all states H_1, $E_{1,1}$ and E_2 had quantum-confined nature – in this case, according to STS results obtained on PbS NCs with similar aspect ratios,[30] state E_2 would be attributable to a higher-order particle-in-a-box-like state quantized in the Z-direction, which would mean that both energy differences E_2 - $E_{1,1}$ and $E_{1,1}$ - H_1 would scale with the NC thicknesses, resulting in a linear correlation between them. Since it has been established above that states H_1 and E_2 are delocalized and are of quantum-confined nature, state $E_{1,1}$ must be of different origin.

The origin of states $E_{1,n}$ may be alternatively explained by using the physical picture developed in several recent STS studies of ordered chain-like atomic structures,[41-43] where the linear-combination-of-atomic-orbitals (LCAO) model was applied to describe the observed extended electronic states formed through coupling of orbitals associated with individual adatoms. According to this physical picture, in the present case $E_{1,n}$ bands may correspond to LCAO-like states formed through coupling of the orbitals associated with individual under-coordinated Pb atoms, with individual $E_{1,n}$ states roughly corresponding

to different linear combinations of such orbitals. The model explains the presence of multiple states in STS spectra, as well as the similarity of their spatial DOS maps. The latter may only be different in their (spatial) nodal structures, which could not be resolved in our measurements.

While the precise atomic structure of the NC surface could not be determined from the collected STS data, the obtained maps of $E_{1,n}$ states suggest that the NC surface is reconstructed analogously to the reconstructions of the PbS(111) surfaces predicted by recent density functional theory calculations.[44] These calculations show that PbS(111) surfaces tend to extensively reconstruct beyond the bond-length modifications found at the surfaces of small metal-chalcogenide NCs.[22] Specifically, PbS(111) surfaces were found to reconstruct by forming submonolayer stripe-like patterns of Pb adatoms, thereby reducing the electrostatic energy of the surface. Indeed, our $E_{1,n}$ maps show stripes oriented at ~30° with respect to the step edges. Since the latter are aligned along the <110> crystallographic directions, the $E_{1,n}$ stripes are likely aligned with one of the <211> directions, consistent with self-assembly of surface Pb atoms in patterns defined by surface crystallographic directions, as would be expected on a reconstructed surface. Existence of well-defined patterns of non-stoichiometric Pb adatoms is also consistent with the observation of the well-defined progressions of STS features corresponding to $E_{1,n}$ states. Such STS features can be expected to be smeared out into featureless bands for

less ordered NC surfaces, as was found for NCs annealed at lower temperatures (data not shown).

Our results suggest that self-assembly of non-stoichiometric adatoms on PbS NC surfaces may result in formation of extended LCAO-like sub-bandgap states, which have important implications for the more general case of imperfectly passivated ligand-covered NCs. Even when the density of dangling bonds per NC is small, the tendency of under-coordinated adatoms to co-localize near structural imperfections, as observed in our work, may lead to stronger electronic coupling of dangling bonds resulting in larger modifications of the sub-bandgap electronic structure than that expected for isolated dangling bonds. The atomic-scale spatial structure of these sub-bandgap states should have a strong impact on the photophysical properties of such NCs, and will be a subject of our future studies. Furthermore, we believe that STS-based mapping of electronic states reported in this Letter, may prove to be a useful tool for identifying the nature of defects and impurities occurring on NC surfaces.

5.2. Experimental Details

Experiments were carried out in a home-built ultra-high vacuum (UHV) cryogenic STM system incorporating a STM scanner from RHK Technology.[45] An Au(111)/mica substrate was prepared *in situ* by using multiple sputter/anneal cycles. Thiol-terminated PbS NCs (synthesis of

PbS NCs is described in the Supporting Information) were deposited on the Au(111) substrate in the load-lock section of the vacuum system using an in-vacuum solenoid pulse valve. The deposition parameters were chosen so as to obtain sub-monolayer NC coverage. The Au(111) substrate with deposited PbS NCs was then annealed overnight in ultra-high vacuum at progressively higher temperatures, with the final temperature of ~170°C. This annealing temperature was chosen to achieve removal of residual unstable species remaining after the initial annealing steps. Figure B.1 shows representative STM images of several NCs on a Au(111) surface.

All imaging and spectroscopic measurements were carried out at a temperature of ~15 K using electrochemically etched silver tips. All STS spectra were recorded using the lock-in technique at ~600 Hz, and bias modulations varying from 10 mV (individual spectra, and one-dimensional spatial scans) to 50 mV (two-dimensional DOS maps).

CHAPTER VI

DISSERTATION SUMMARY

In closing, the work contained in this dissertation demonstrated the first ever successful coupling of a closed-cycle cryostat (CCC) to a scanning tunneling microscope (STM) for operation in an ultra-high vacuum (UHV) environment. Specifically, this work showed that is in fact feasible to couple a CCC to a STM, and that the system is capable of atomic-scale resolution. Performance-wise, this dissertation showed:

1. The topography scans had sub-nanometer lateral (x-y plane) resolution under cryogenic conditions (~15-16 K). This was clearly seen in the measured nearest neighbor distance of 0.29 nm for the Au(111) surface, which also displayed a clear hexagonal atomic pattern characteristic of the Au(111) surface, neither of which had any identifiable features attributable to the CCC noise (Figure 3.5a). A second example of sub-nanometer resolution is seen in the nearest neighbor distance of 0.40 nm for the NaCl(100) monolayer film thermally deposited on the Au(111) surface, which showed the characteristic square atomic pattern of NaCl(100); again, without any identifiable features attributable to the CCC noise (Figure 3.5b). As far as the z-direction (height) topography measurements are concerned, the data showed that our

instrument is capable of picometer resolution. The is seen in the cross-section of the Au(111) topography from Figure 3.5a, which showed well-defined atomic corrugation of ~30 pm; and in the cross-section of the NaCl(100) topography from Figure 3.5b, which showed a well-defined atomic corrugation of ~10 pm; both measurements suggesting the CCC noise is significantly less than this number. An atomic-resolution image obtained on single-walled carbon nanotubes (CNT) deposited on the Au(111) surface, showing the carbon atoms of the nanotube along with the CNT chirality (Figure 3.5e).

2. Scanning tunneling spectroscopy (STS) was conducted on a variety of materials, showing that out spectroscopy measurements are not susceptible to the mechanical vibrations of the CCC. For each 0.1 nm increase in the tunneling gap distance, a one order of magnitude decrease of the tunneling current is expected. Our measurements showed that the tunneling current fluctuation corresponds to a z-height difference as a result of CCC mechanical vibrations of 1.7 pm (Chap. III), thus explaining the lack of CCC-induced noise in our images and spectra. The STS spectra for CNTs in Chapters III and IV, and for PbS quantum dots (QDs) in Chapter V, showed that the home-built UHV CCC STM performed as hoped. With the resolution of the data on par with traditional flow- and bath-cryostat STMs.

3. As an unexpected, and quite serendipitous outcome, it was found that the CCC STM piezoelectric motors were resistant to the thermal creep associated with the cryogenic fluid pressure fluctuations of flow-type cryostats. This is a real and tangible benefit to the STM community as it will allow experimentalists to conduct long-term studies of a vast array of systems, without paying the price of helium consumption.

Furthermore, it would seem to be practical and prudent for experimentalists to adopt the in described technique of coupling a CCC to a STM based on the projected helium scarcity of the not-to-distant-future (discussed briefly in Chap. III). Granted, the lowest temperatures obtained by the instrument described in this research is about 10-15 K higher than the lowest temperatures of flow-type cryostat STMs, yet the results described in show that data is not affected by the CCC and that the vibrational isolation system, as designed, is efficient enough to attenuate the CCC mechanical vibrations such that they are nearly imperceptible in the STM data. Thus, it is hoped that this dissertation will serve as a guide to other STM experimentalists, whether as a blueprint, or as a sign post for a new direction of innovation.

APPENDIX A

SUPPORTING INFORMATION TO CHAPTER IV

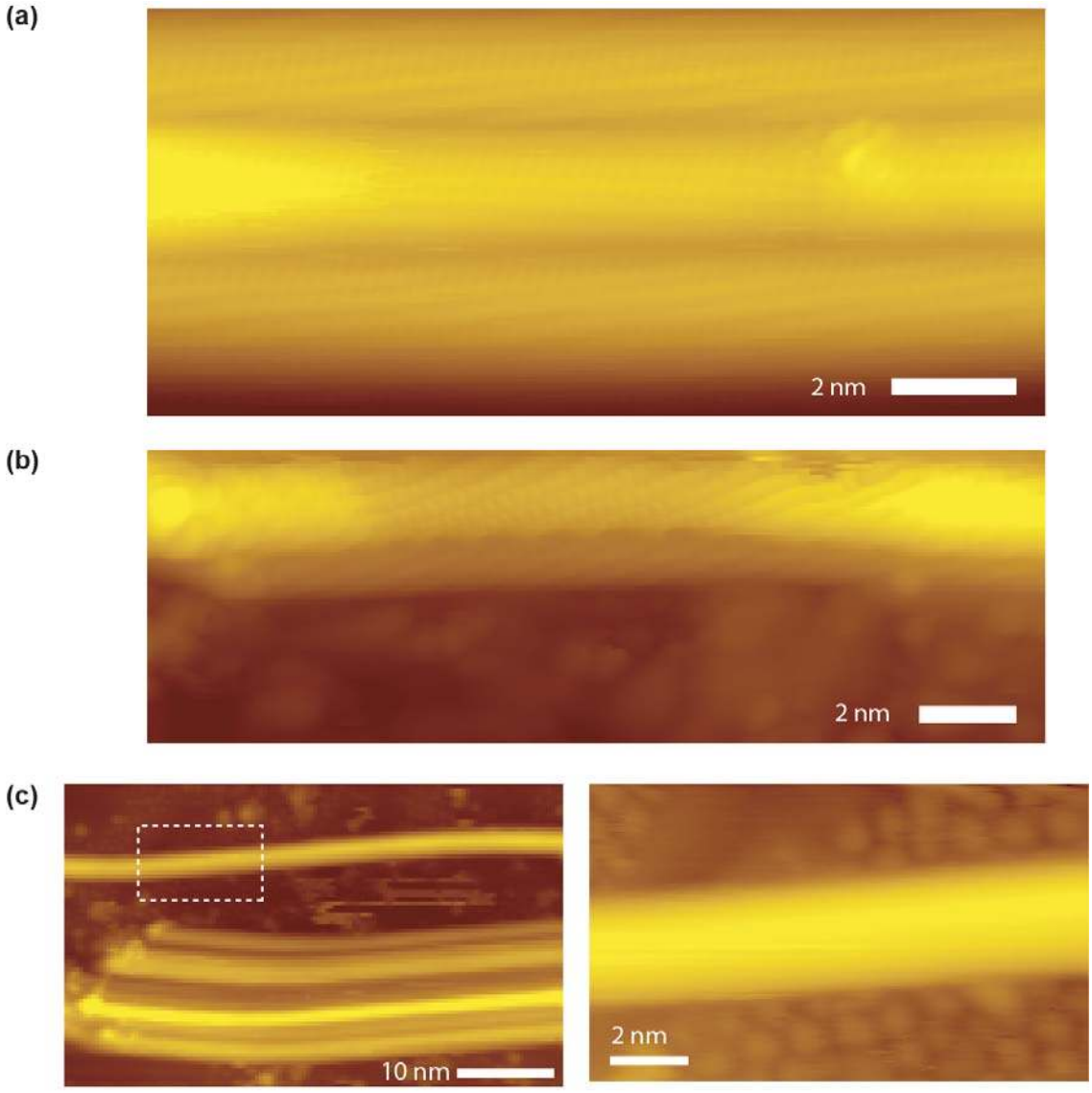

Figure A.1. Representative STM images of several CNTs deposited on the Au(111) surface using the "dry contact transfer" method. Nanotubes constituted ~70% of the SWNT-containing powder obtained from Sigma-Aldrich, which explains the presence of small clusters around the nanotubes in the majority of the STM images.

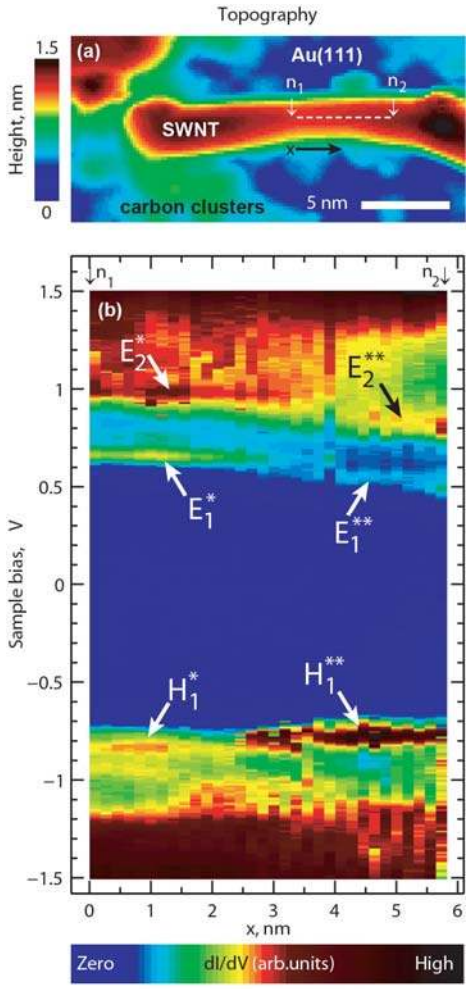

Figure A.2. **(a)** STM topography of a SWNT, different from that of Figure 4.1(b) of the main text. **(b)** STS signal as a function of the x coordinate [as shown in (a)] and sample bias voltage. (STS signal serves as a measure of the local density of electronic states.) The spatial range corresponds to the dashed line between points n_1 and n_2 in (a). Positive voltages correspond to unoccupied electronic states, while negative voltages correspond to occupied states. All data were measured along the nanotube centerline. The spectra show Van Hove singularities, with the most visible states being H_1-type (derived from the valence band), E_1-type (derived from the conduction band), and E_2-type (derived from the band immediately above the conduction band). Some bandgap variation is observed in the STS map shown in Figure A.2(b), with levels E_n^* and H_1^* on the left side of the map, and levels E_n^{**} and H_1^{**} on the right side. The observed bandgap variation is likely a result of the non-uniform environment of the nanotube: the vicinity of point n_2 shows a higher density of impurities located around the nanotube.

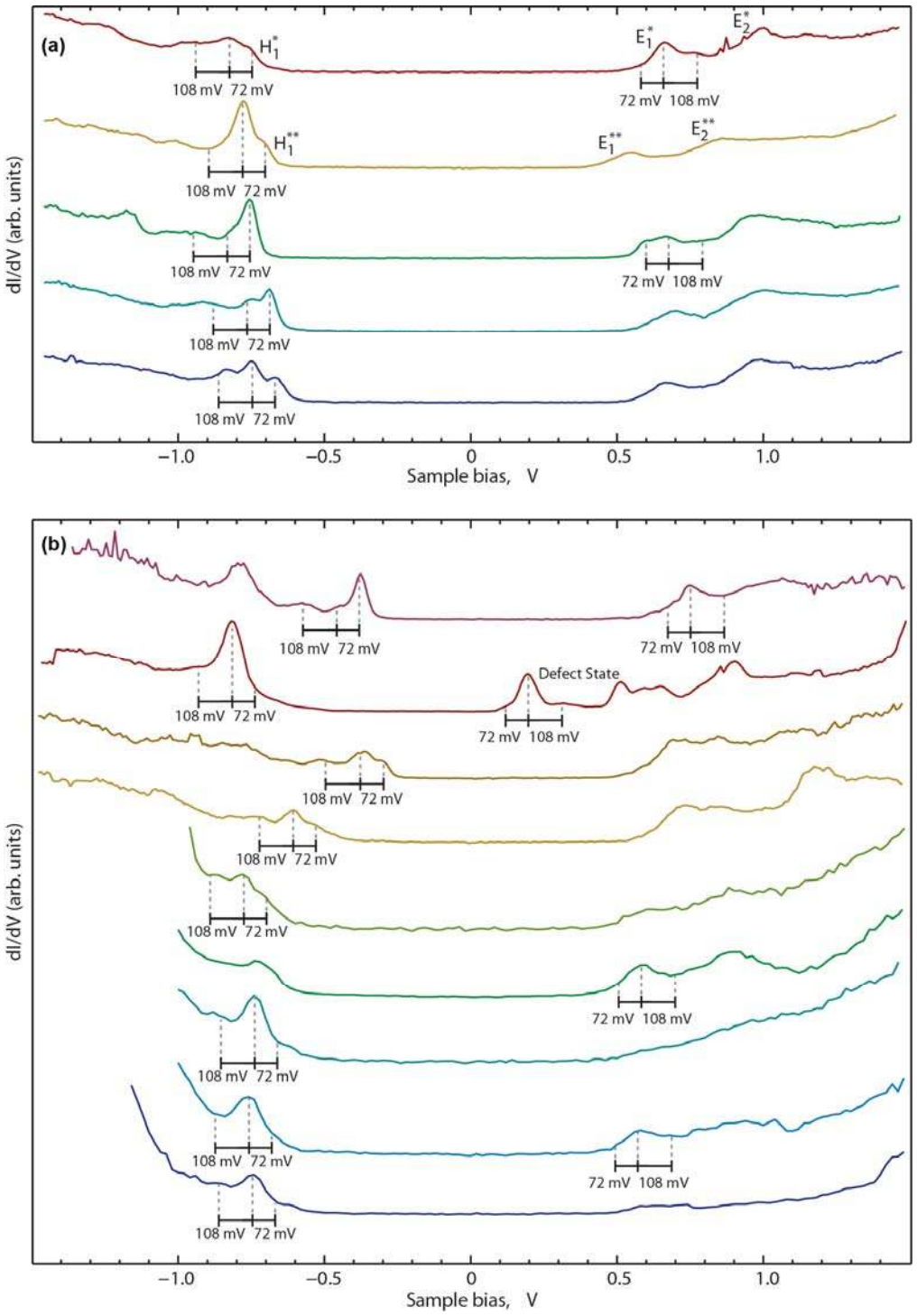

Figure A.3. STS spectra showing fine spectral structures. **(a)** Spectra for the nanotube shown in Figure A.2a, the bottom three spectra measured outside of the region contained between points n_1 and n_2. **(b)** Additional spectra from localized states in other nanotubes.

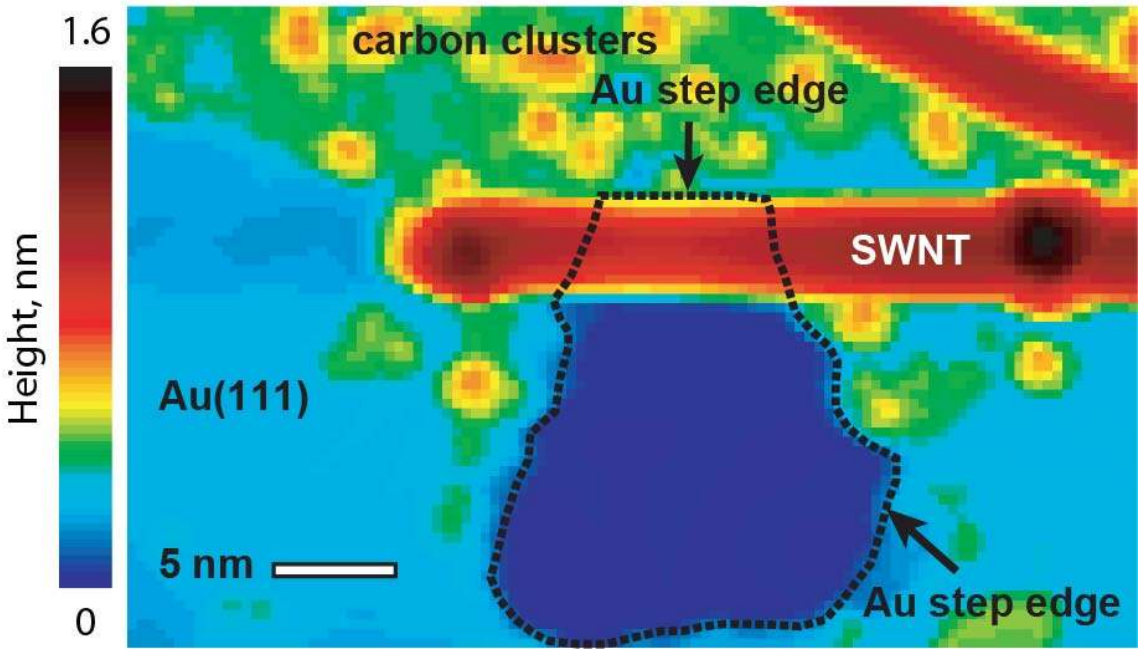

Figure A.4. Zoomed-out view of the SWNT from Figure 4.1(b) showing the geometry of the Au trench straddled by the nanotube.

The band bending observed in points *L* and *R* in Figure A.2 is explained by the charge transfer[1] between the nanotube and Au substrate caused by the mismatch in their effective work-functions.[2] As described in the main text, the SWCNT workfunction is 4.8 eV,[1] which is ~100meV higher than the effective workfunction of the Au substrate. This number is lower than the workfunction of the pristine Au(111) surface, 5.3 eV, apparently due to the direct proximity of a Au atomic step running along the SWCNT, shown in Figure A.4. Indeed, as can be seen from Figure A.4, the Au terrace shown in dark blue does not extend above the nanotube. On the other hand, Figure 4.1c clearly shows that the nanotube touches this Au terrace in point *L*, which is only possible if

the top boundary of this terrace runs roughly along the nanotube, as schematically shown in Figure A.4. The Au step edge carries with it a workfunction-lowering charge redistribution caused by the Smoluchowski effect.[1]

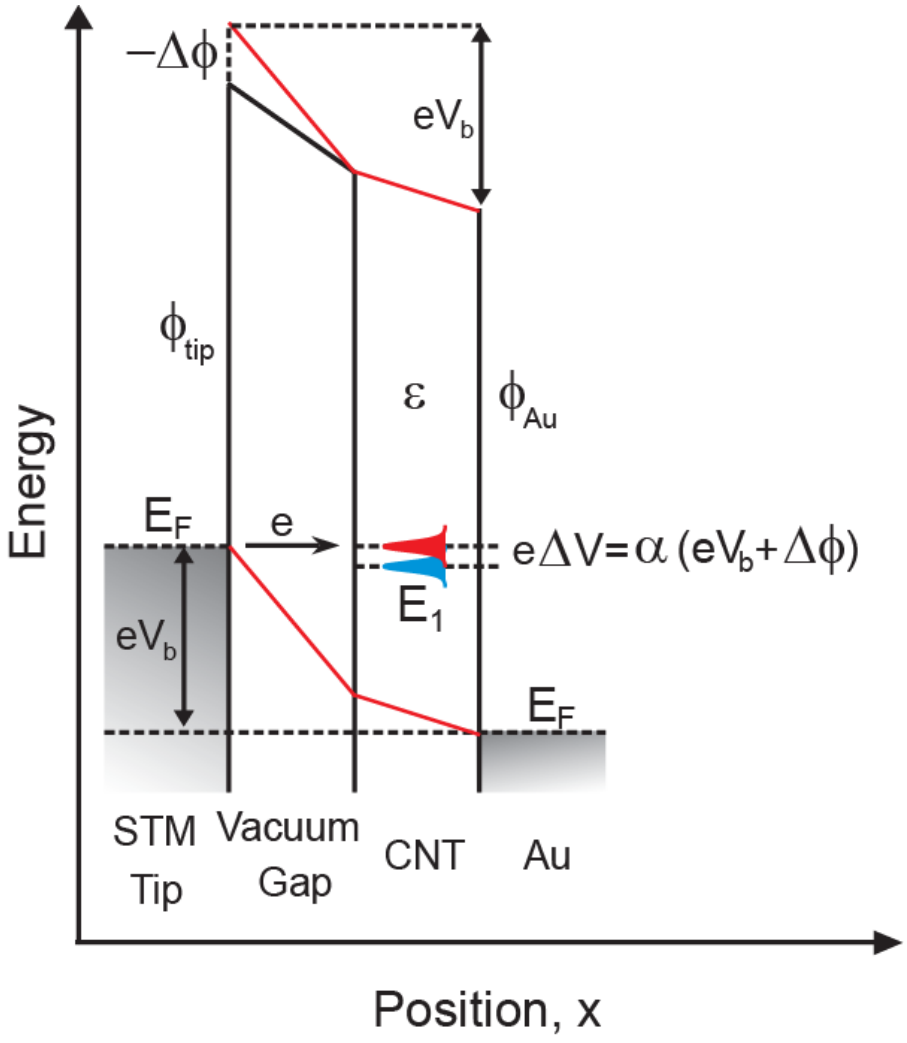

Figure A.5. Voltage drop in a biased STM junction with a SWNT under the STM tip.

Mismatch of workfunctions in the tip ϕ_{tip} and substrate ϕ_{Au}, together with the finite voltage drop ΔV inside the SWNT, lead to a shift of

electronic state E_1 by $e\Delta V = \alpha(\, eV_b + \Delta\phi)$, where V_b is the applied bias voltage, $\Delta\phi = \phi_{tip} - \phi_{Au}$, and e is the electron charge. Parameter α thus relates the average potential inside the nanotube to the external potentials applied across the tunneling gap. Therefore, states E_1 (unoccupied) and H_1 (occupied) are observed at voltages V_E and V_H that are defined by the following equations:

$$E_1 + \alpha\Delta\phi = (1 - \alpha)\, eV_E \tag{A.1}$$

$$H_1 + \alpha\Delta\phi = (1 - \alpha)\, eV_H \tag{A.2}$$

Where E_1 and H_1 are the true energies of states E_1 and H_1 with respect to the substrate Fermi level. Voltages V_E and V_H are determined directly from the STS spectra. Then we can eliminate unknown $\Delta\phi$ so that:

$$E_1 - H_1 = (1 - \alpha)(eV_E - eV_H) \tag{A.3}$$

Quantities appearing on the right side of the equation depend on the relative lateral distance between the tip apex and the "centers of gravity" of the measured localized states E_1 and H_1. Indeed, Figure 4.2 of the main text shows a noticeable "curving" of localized states $E_{1,1}$, H_1^*, H_1^{**}, and other states appearing at onsets of conduction. This is primarily a result of the variation of α with distance Δx to the "center of gravity" of the corresponding state.

Then, when the tip is at a lateral distance Δx away from states E_1 or H_1, we can write

$$E_1 - H_1 = (1 - \alpha_{\Delta x})(eV_{E,\Delta x} - eV_{H,\Delta x}) \tag{A.4}$$

And when the tip is immediately above states E_1 or H_1, we can write:

$$E_1 - H_1 = (1 - \alpha_0)(eV_{E,0} - eV_{H,0}) \tag{A.5}$$

Then unknown difference $E_1 - H_1$ is eliminated, so that:

$$\frac{1 - \alpha_0}{1 - \alpha_{\Delta x}} = \frac{V_{E,\Delta x} - V_{H,\Delta x}}{V_{E,0} - V_{H,0}} = \kappa = 1.045 \tag{A.6}$$

Here, quantities $V_{E,\Delta x}$ and $V_{H,\Delta x}$, as well as $V_{E,0}$ and $V_{H,0}$, were extracted from Figure A.6 using states $E_{1,1}$ and H_1^*, and $\Delta x = 3\,nm$ (offset from the "centers of gravity" of the corresponding states).

Quantity $\gamma = \alpha_{\Delta x}/\alpha_0$ depends primarily on the shape of the tip, and can be measured independently by using spectra showing bipolar transport,[3] which was observed at a SWCNT defect located nearby (Figure A.7). Bipolar transport through a given state E_d (in Figure A.7 the state originates from a defect) can occur either at a positive voltage V_E^+ or a negative voltage V_E^- described by the following formulae:

$$E_d + \alpha_d \Delta\phi = (1 - \alpha_d)\, eV_E^+ \tag{A.7}$$

$$E_d + \alpha_d \Delta\phi = -\alpha_d\, eV_E^- \tag{A.8}$$

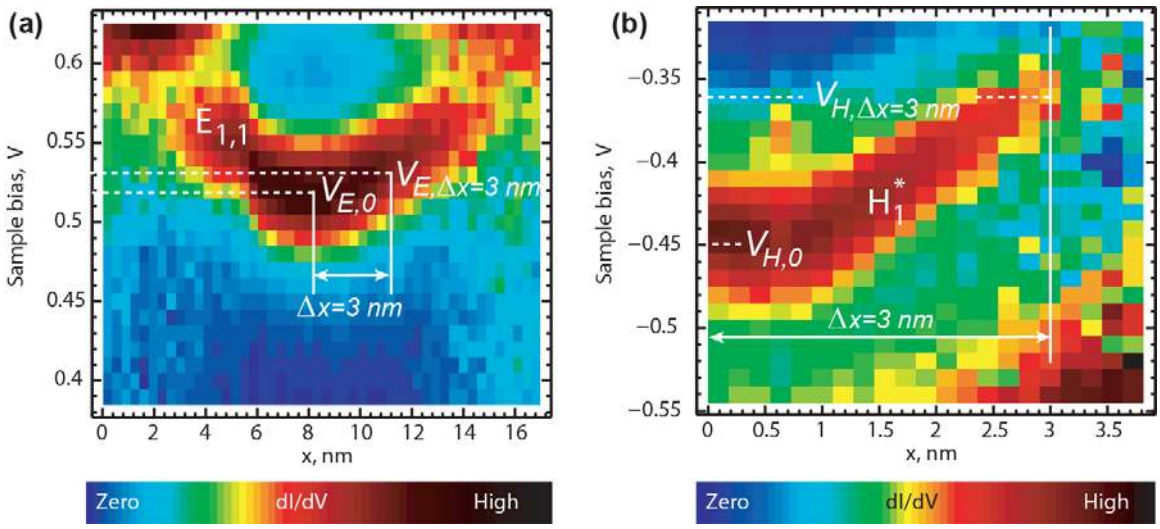

Figure A.6. Spatial dependence of STS peaks corresponding to states $E_{1,1}$ [shown in (a)] and H_1^* [shown in (b)] from Figure A.2. The spatial coordinate x is identical to that used in Figure A.2. The STS signal has been renormalized so as to give constant integral DOS within the ranges shown.

From these we have:

$$(1-\alpha_d)\,V_E^+ = -\alpha_d\,V_E^- \tag{A.9}$$

Which gives for α_d:

$$\alpha_d = \frac{V_E^+}{V_E^+ - V_E^-} \tag{A.10}$$

Here α_d is a function that depends on coordinate x. In principle, α_d may not be equal to α, because the "center of gravity" of the defect state is not necessarily at the same height as that of states $E_{1,1}$ and H_1^*. However, in the limit of a slowly changing tip profile, approximate equality

$$\frac{\alpha_{\Delta x}}{\alpha_0} \approx \frac{\alpha_{d,\Delta x}}{\alpha_{d,0}} \tag{A.11}$$

applies, which can be used for the evaluation of $\gamma = \alpha_{\Delta x}/\alpha_0$. From Figure A.6 we determine V_E^+ and V_E^-, at $\Delta x = 0$ and $\Delta x = 3\,nm$, which give $\gamma \approx 0.6 \pm 0.05$. Then:

$$\alpha_0 = \frac{\kappa - 1}{\kappa - \gamma} \approx 0.10 \pm 0.01 \qquad \text{(A.12)}$$

is the quantity that determines the average potential inside the nanotube of Figure 4.2 of the main text.

Figure A.7 (next page). Spatial dependence of STS peaks corresponding to bipolar transport through state E_d that originates from a defect located on the same nanotube as that shown in Figure A.2. See text for definitions of band onsets V_E^+ and V_E^-.

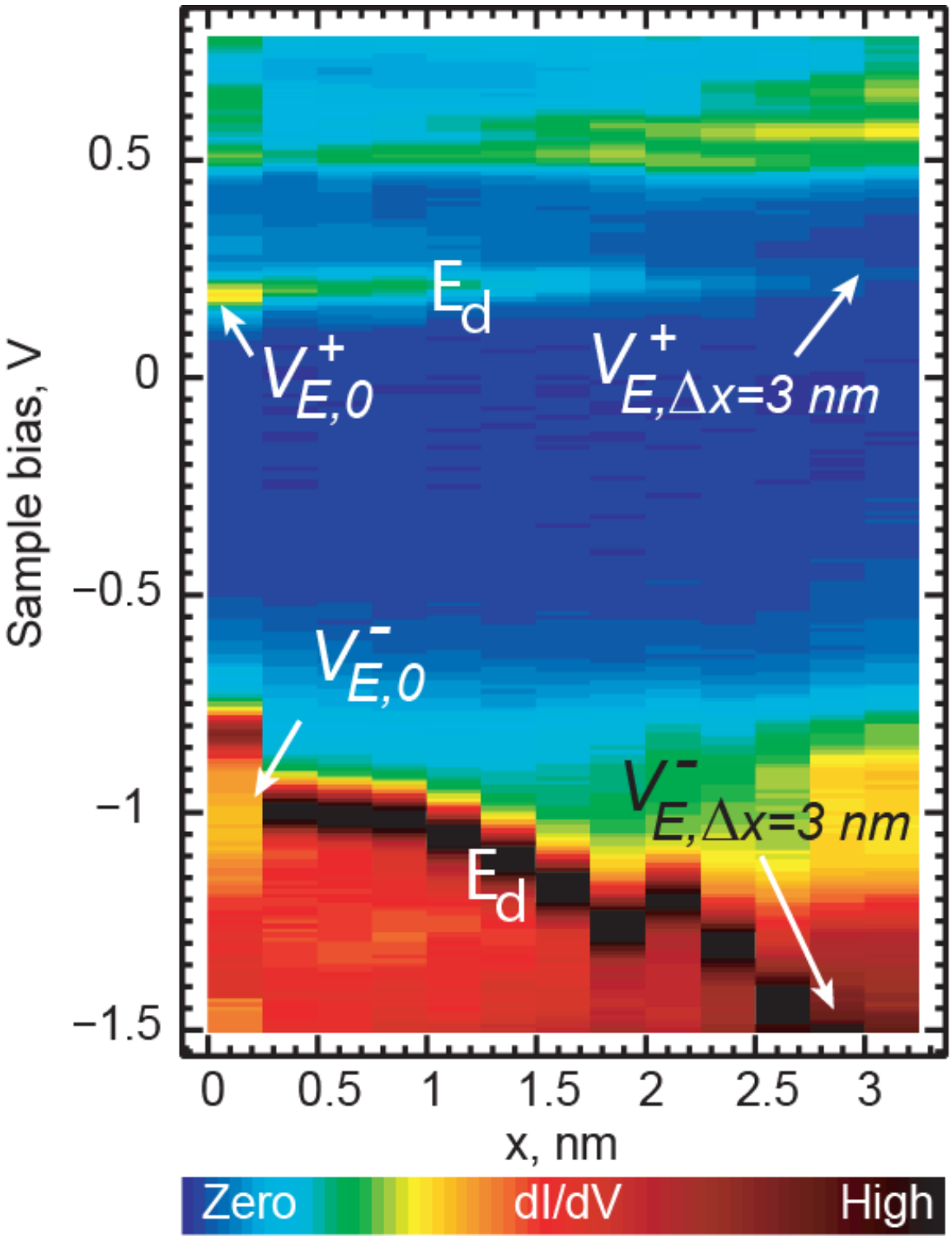
0.5
0
−0.5
−1
−1.5
Sample bias, V
0
0.5
1
1.5
2
2.5
3
x, nm
E_d
$V^+_{E,0}$
$V^+_{E,\Delta x=3\ nm}$
$V^-_{E,0}$
$V^-_{E,\Delta x=3\ nm}$
E_d
Zero
dI/dV
High

APPENDIX B

SUPPORTING INFORMATION TO CHAPTER V

NC Crystallographic Orientation

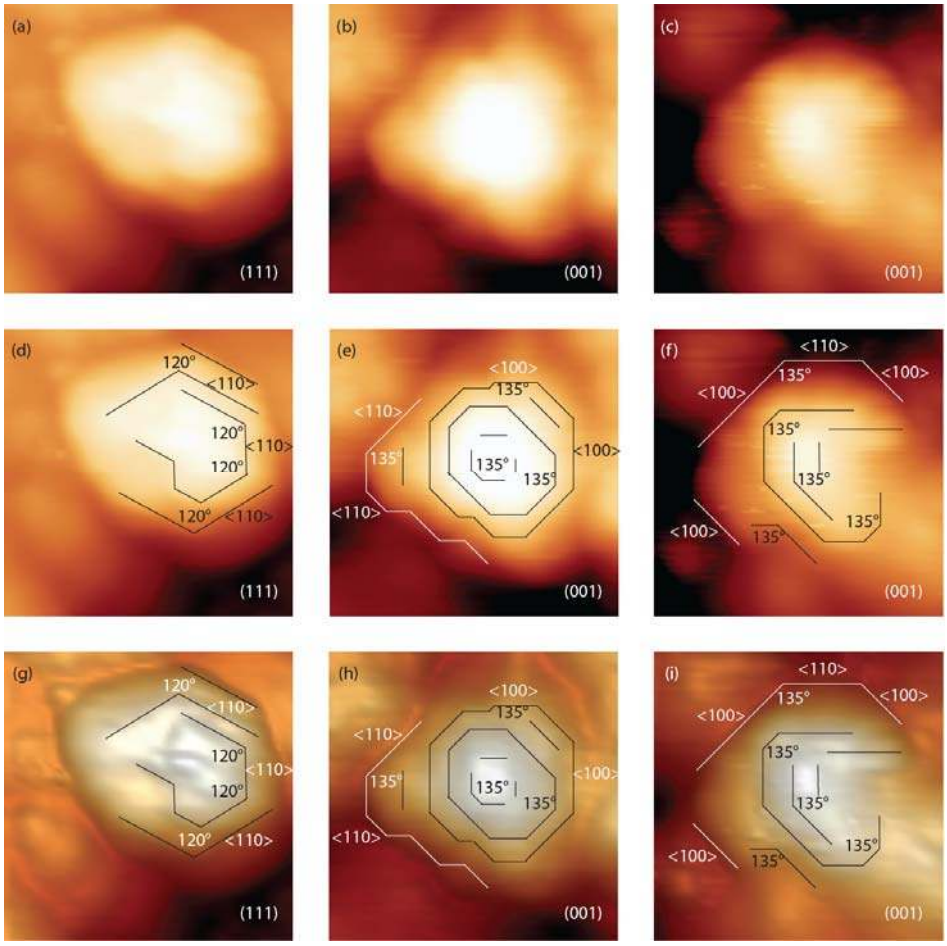

Figure B.1. STM topographic images showing crystallographic features for three PbS NCs. **(a), (b), (c)** Topographies for three representative NCs. **(d), (e), (f)** NC topographies, [same as in (a), (b), and (c) respectively] with lines and relative angles indicating orientations of crystallographic features for each NC. The observed angles suggest that the top NC facets corresponds to crystal planes (111), (100), and (100) respectively. **(g), (h), (i)** Enhanced topographic images [for the same NCs] with same crystallographic markings as in (d), (e) and (f).

NC Band Bending

Mismatch of workfunctions in the tip ϕ_{tip} and substrate ϕ_{Au}, together with the finite voltage drop ΔV inside the NC, lead to a shift of electronic state E_1 by $e\Delta V = \alpha(eV_b + \Delta\phi)$, where V_b is the applied bias voltage, $\Delta\phi = \phi_{tip} - \phi_{Au}$, and e is the electron charge. Parameter α thus relates the average potential inside the nanocrystal to the external potentials applied across the tunneling gap. Therefore, states E_1 (unoccupied) and H_1 (occupied) are observed at voltages V_E and V_H that are defined by the following equations:[1-2]

$$eV_E = \frac{E_1 + \alpha\Delta\phi}{1 - \alpha} \tag{B.1}$$

$$eV_H = \frac{H_1 + \alpha\Delta\phi}{1 - \alpha} \tag{B.2}$$

Where E_1 and H_1 are the true energies of states E_1 and H_1 with respect to the substrate Fermi level. Voltages V_E and V_H are determined directly from the STS spectra. Observations of "reverse" tunneling spectral features[1,3] analogous to H** lead to typical values of α on the scale of a few percent.

The changes in voltages V_E and V_H observed in Figure 5.3b of the main text are caused by the fact that α depends on the relative distance between the tip apex and the "centers of gravity" of states E_1 and H_1. Factor α is higher at the periphery of NC_1, as compared to the center of NC_1's top facet because in the former case the tip is located closer to the

Au surface, which results in a larger electric field inside the NC, leading to higher effective voltage drop inside the NC. Without the $\Delta\phi$ term, this effect would lead to "curving" of V_E and V_H trajectories away from axis V = 0 in Figure 5.3b, as observed for V_H. In the present case, however, $\Delta\phi$ is nonzero and negative. This reinforces the "curving" trend observed for V_H, but counteracts the "curving" of V_E.

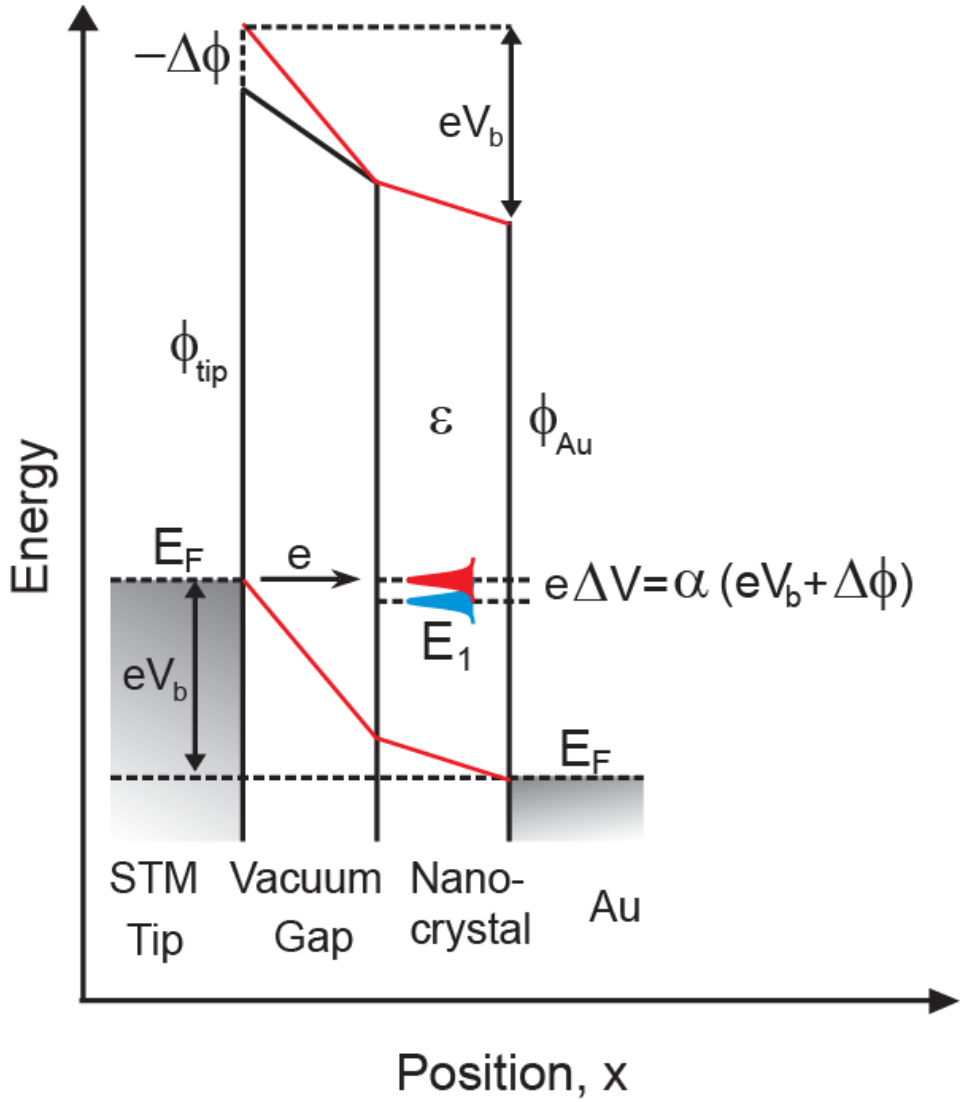

Figure B.2. Voltage drop in a biased STM junction with a NC under the STM tip.

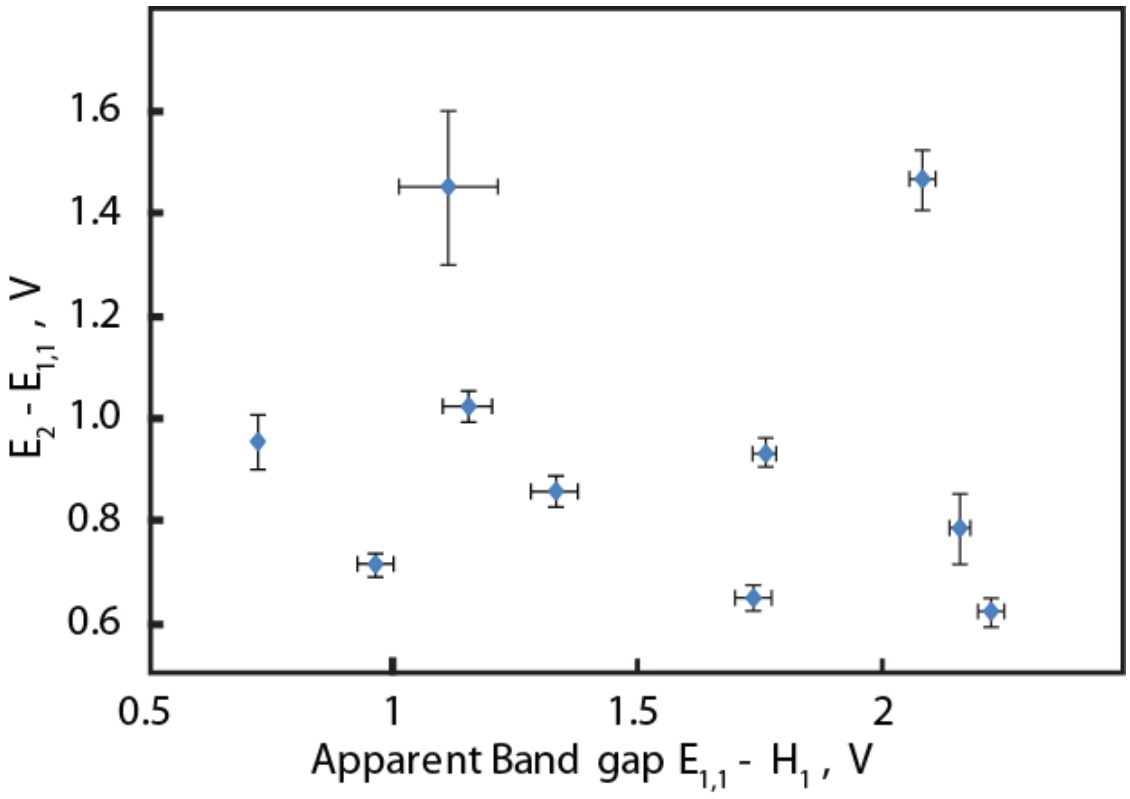

Figure B.3. Plot of the energy difference between the E_2 and $E_{1,1}$ states vs. the energy difference between the $E_{1,1}$ and H_1 states for 10 measured NCs. During this experiment, many of the measured NCs did not exhibit clearly-defined H_1 or E_2 states, and thus were not included here.

PbS nanocrystal synthesis

Synthesis of PbS NCs was performed following a modified procedure from Hines and Scholes.[4] Lead oxide (PbO, 99.0%), oleic acid (OA, technical grade 90%), 1-octadecene (ODE, technical grade 90%, pumped on at 80° C for 8 hours), toluene (99.8%, anhydrous), pentane (anhydrous), methanol (anhydrous), pentanethiol (98%), and pentanedithiol (96%) were purchased from Sigma-Aldrich and used as

received unless otherwise stated. Bis(trimethylsilyl)sulfide ($(TMS)_2S$, synthesis grade) was purchased from Gelest.

All syntheses were conducted using standard Schlenk techniques. In a typical synthesis, 4 mL of ODE and 4 mL of OA were combined with 0.30 g of PbO (1.3 mmol). The mixture was heated, with stirring, to 100° C for 30 minutes, then heated to the injection temperature of 105° C for at least 30 minutes, all under vacuum. A sulfur precursor solution containing 0.167 mL (0.8 mmol) of $(TMS)_2S$ in 4 mL of ODE was prepared in a glovebox under nitrogen atmosphere. The sulfur precursor solution was quickly injected into the flask and held at 95° C for 1 minute, then cooled to room temperature in an ice bath. Removal of excess ligand and 1-octadecene was completed by repeated precipitation in acetone, centrifugation of the particles, and dispersion in small amounts of toluene. Finally, the NC dispersion was filtered through a 0.2 μm syringe filter to remove any insoluble material.

Prior to using PbS NCs in STS experiments, a ligand exchange was performed using a combination of pentanethiol and pentanedithiol in an effort to improve NC adhesion to the gold substrate and remove highly insulating OA ligands. In a typical ligand exchange procedure 0.3 mL of stock solution of PbS NC (15 mg/mL in toluene) was diluted with 5 mL of pentane in a centrifuge tube with an air-tight lid with septum. Several drops of pentanethiol stock solution (9:1 pentanethiol:pentanedithiol, total concentration 0.15 M in pentane) were added via syringe and then

mixed. Pentanethiol capped PbS NCs were precipitated from pentane using methanol and centrifuged at 3500 rpm. Following removal of the supernatant, NCs were redispersed in toluene. This cleaning procedure was repeated two times. Finally, PbS NCs were dispersed in anhydrous pentane to produce a 0.9 mg/mL stock solution. The suspension was centrifuged to remove aggregates, and the remaining dispersed NCs were transferred to a clean tube under N_2 for use in STM experiments.

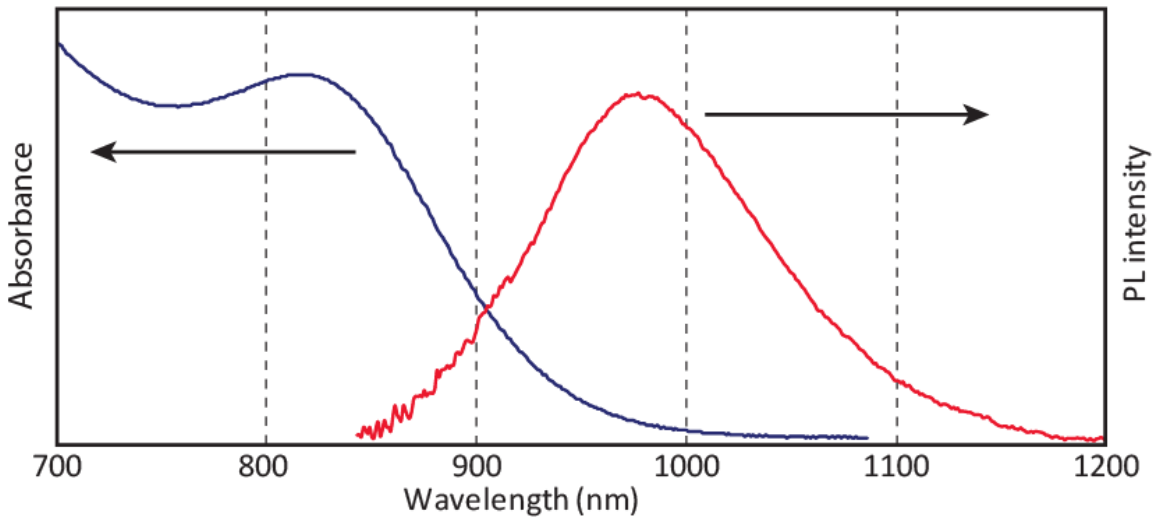

Figure B.4. Absorbance and PL spectra of PbS NCs following thiol-ligand exchange. The emission peak at 977 nm (1.27 eV) corresponds to an approximate diameter of 3.2 nm PbS NC.

REFERENCES CITED

Chapter I

1. Binnig, G., Rohrer, H., Gerber, C. & Weibel, E. Tunneling through a controllable vacuum gap. Appl. Phys. Lett. 40, 178–180 (1982).

2. Binnig, G. & Rohrer, H. Helvetica Physica Acta. **55,** 726–735 (1982).

3. Binnig, G. & Rohrer, H. Scanning tunneling microscopy. *Surf. Sci.* **126,** 236–244 (1983).

4. Binnig, G. & Rohrer, H. Scanning tunneling microscopy—from birth to adolescence. *Rev. Mod. Phys.* **59,** 615–625 (1987).

5. Binnig, G. & Rohrer, H. In touch with atoms. *Rev. Mod. Phys.* **71,** S324–S330 (1999).

6. Moore, A. M. & Weiss, P. S. Functional and Spectroscopic Measurements with Scanning Tunneling Microscopy. *Annu. Rev. Anal. Chem.* **1,** 857–882 (2008).

7. Stipe, B. C., Rezaei, M. A. & Ho, W. Single-Molecule Vibrational Spectroscopy and Microscopy. *Science* **280,** 1732–1735 (1998).

8. Stipe, B. C., Rezaei, M. A. & Ho, W. Localization of Inelastic Tunneling and the Determination of Atomic-Scale Structure with Chemical Specificity. *Phys. Rev. Lett.* **82,** 1724–1727 (1999).

9. Bonnell, D. A. *et al.* Imaging physical phenomena with local probes: From electrons to photons. *Rev. Mod. Phys.* **84,** 1343–1381 (2012).

10. Tao, F. (Feng), Nguyen, L. & Zhang, S. Design of a new reactor-like high temperature near ambient pressure scanning tunneling microscope for catalysis studies. *Rev. Sci. Instrum.* **84,** 034101 (2013).

11. Dovek, M. M., Heben, M. J., Lang, C. A., Lewis, N. S. & Quate, C. F. Design of a scanning tunneling microscope for electrochemical applications. *Rev. Sci. Instrum.* **59,** 2333–2336 (1988).

12. Kambara, H., Matsui, T., Niimi, Y. & Fukuyama, H. Construction of a versatile ultralow temperature scanning tunneling microscope. *Rev. Sci. Instrum.* **78,** 073703 (2007).

13. Karcı, Ö. *et al.* An ultra-low temperature scanning Hall probe microscope for magnetic imaging below 40 mK. *Rev. Sci. Instrum.* **85,** 103703 (2014).

14. Günther, S. *et al.* High-Temperature Scanning Tunneling Microscopy Study of the Ordering Transition of an Amorphous Carbon Layer into Graphene on Ruthenium(0001). *ACS Nano* **7,** 154–164 (2013).

15. Pan, S. H., Hudson, E. W. & Davis, J. C. 3He refrigerator based very low temperature scanning tunneling microscope. *Rev. Sci. Instrum.* **70,** 1459–1463 (1999).

16. Mironov, V. *Fundamentals of Scanning Probe Microscopy*. (THE RUSSIAN ACADEMY OF SCIENCES INSTITUTE FOR PHYSICS OF MICROSTRUCTURES, 2004). at <https://sites.google.com/site/vmironovipm/SPM-textbook>

17. Johnson, K. University of Oregon Helium Liquefier History (Personal Communication). (2014).

Chapter II

1. Chen, C. J. *Introduction to Scanning Tunneling Microscopy*, Oxford University Press New York (2008).

2. Tersoff, J. & Hamann, D. R. Theory and Application for the Scanning Tunneling Microscope. *Phys. Rev. Lett.* **50,** 1998–2001 (1983).

3. Bardeen, J. Tunnelling from a Many-Particle Point of View. *Phys. Rev. Lett.* **6,** 57–59 (1961).

4. Giaever, I. Electron Tunneling Between Two Superconductors. *Phys. Rev. Lett.* **5, 464**–466 (1960).

5. Nicol, J., Shapiro, S. & Smith, P. H. Direct Measurement of the Superconducting Energy Gap. *Phys. Rev. Lett.* **5,** 461–464 (1960).

6. Bonnell, D. A. *Scanning Probe Microscopy and Spectroscopy : Theory, Techniques, and Applications*. (Wiley-VCH, 2001).

7. Tersoff, J. & Hamann, D. R. Theory of the scanning tunneling microscope. *Phys. Rev. B* **31,** 805–813 (1985).

Chapter III

1. Chen, C. J. *Introduction to Scanning Tunneling Microscopy*, Oxford University Press New York (2008).

2. S. Behler, M. K. Rose, J. C. Dunphy, D. F. Ogletree, M. Salmeron and C. Chapelier, Review of Scientific Instruments 68, (1997).

3. B. C. Stipe, M. A. Rezaei and W. Ho, Review of Scientific Instruments 70, (1999).

4. E. T. Foley, N. L. Yoder, N. P. Guisinger and M. C. Hersam, Review of Scientific Instruments 75, (2004).

5. G. Meyer, Review of Scientific Instruments 67, (1996).

6. S. H. Pan, E. W. Hudson and J. C. Davis, Review of Scientific Instruments 70, (1999).

7. B. J. Albers, M. Liebmann, T. C. Schwendemann, M. Z. Baykara, M. Heyde, M. Salmeron, E. I. Altman and U. D. Schwarz, Review of Scientific Instruments 79, (2008).

8. Zhang, S. "United States extends life of helium reserve: Congress moves to head off shortages, but US researchers still face ballooning prices," Nature News, 26 September 2013.

9. CS202PF-X20B Cryostat from Advanced Research Systems, Inc., 7476 Industrial Park Way, Macungie, PA 18062, United States.

10. T. Tomaru, T. Suzuki, T. Haruyama, T. Shintomi, A. Yamamoto, T. Koyama and R. Li, Cryogenics 44, (2004).

11. Cryostat noise specifications are available from Advanced Research Systems, Inc., 7476 Industrial Park Way, Macungie, PA 18062, United States.

12. RHK Technology, Inc., 1050 East Maple Road, Troy, Michigan 48083, United States.

13. H. J. Hug, B. Stiefel, P. J. A. van Schendel, A. Moser, S. Martin and H. J. Guntherodt, Review of Scientific Instruments 70, (1999).

14. X. H. Qiu, G. V. Nazin and W. Ho, Science 299, (2003).

15. C. Chen, P. Chu, C. A. Bobisch, D. L. Mills and W. Ho, Physical Review Letters 105, (2010).

16. G. V. Nazin, X. H. Qiu and W. Ho, Physical Review Letters 90, (2003).

17. S. W. Wu, G. V. Nazin and W. Ho, Phys. Rev. B 77, (2008).

18. Shapal , Precision Ceramics, 86 Lower Tower Street, Birmingham B19 3PA, England.

19. P. M. Albrecht and J. W. Lyding, Applied Physics Letters 83, (2003).

20. Series 99 Pulse Valve, Parker Hannifin Corporation, 26 Clinton Drive, Unit 103, Hollis, NH 03049, United States.

21. Z. Q. Wei, S. Guo and S. A. Kandel, J. Phys. Chem. B 110, (2006).

22. J. V. Barth, H. Brune, G. Ertl and R. J. Behm, Phys. Rev. B 42, (1990).

23. B. C. Stipe, M. A. Rezaei and W. Ho, Science 280, (1998).

Chapter IV

1. Avouris, P.; Freitag, M.; Perebeinos, V. Carbon-Nanotube Photonics and Optoelectronics. *Nat. Photonics* **2008,** *2*, 341-350.

2. Dresselhaus, M. S.; Dresselhaus, G.; Saito, R.; Jorio, A. Exciton Photophysics of Carbon Nanotubes. *Annu. Rev. Phys. Chem.* **2007,** *58*, 719-747.

3. Avouris, P.; Chen, Z. H.; Perebeinos, V. Carbon-Based Electronics. *Nat. Nanotechnol.* **2007,** *2*, 605-615.

4. Charlier, J. C.; Blase, X.; Roche, S. Electronic and Transport Properties of Nanotubes. *Rev. Mod. Phys.* **2007,** *79*, 677-732.

5. Freitag, M.; Tsang, J. C.; Bol, A.; Avouris, P.; Yuan, D. N.; Liu, J. Scanning Photovoltage Microscopy of Potential Modulations in Carbon Nanotubes. *Appl. Phys. Lett.* **2007,** *91*, 031101.

6. Biercuk, M.; Ilani, S.; Marcus, C.; McEuen, P. Electrical Transport in Single-Wall Carbon Nanotubes. In *Carbon Nanotubes*, Jorio, A.; Dresselhaus, G.; Dresselhaus, M., Eds.; Topics in Applied Physics; Springer Berlin Heidelberg: 2008; Vol. 111, pp 455-493.

7. Stokes, P.; Khondaker, S. I. Evaluating Defects in Solution-Processed Carbon Nanotube Devices Via Low-Temperature Transport Spectroscopy. *ACS Nano* **2010,** *4*, 2659-2666.

8. Gao, B.; Glattli, D. C.; Plaçais, B.; Bachtold, A. Cotunneling and One-Dimensional Localization in Individual Disordered Single-Wall Carbon Nanotubes: Temperature Dependence of the Intrinsic Resistance. *Phys. Rev. B* **2006,** *74*, 085410.

9. Bachtold, A.; Fuhrer, M. S.; Plyasunov, S.; Forero, M.; Anderson, E. H.; Zettl, A.; McEuen, P. L. Scanned Probe Microscopy of Electronic Transport in Carbon Nanotubes. *Phys. Rev. Lett.* **2000,** *84*, 6082-6085.

10. Wang, N. P.; Heinze, S.; Tersoff, J. Random-Telegraph-Signal Noise and Device Variability in Ballistic Nanotube Transistors. *Nano Lett.* **2007,** *7*, 910-913.

11. Liu, F.; Bao, M. Q.; Kim, H. J.; Wang, K. L.; Li, C.; Liu, X. L.; Zhou, C. W. Giant Random Telegraph Signals in the Carbon Nanotubes as a Single Defect Probe. *Appl. Phys. Lett.* **2005,** *86*, 163102.

12. Tans, S. J.; Dekker, C. Molecular Transistors: Potential Modulations Along Carbon Nanotubes. *Nature* **2000,** *404*, 834-835.

13. Purewal, M. S.; Hong, B. H.; Ravi, A.; Chandra, B.; Hone, J.; Kim, P. Scaling of Resistance and Electron Mean Free Path of Single-Walled Carbon Nanotubes. *Phys. Rev. Lett.* **2007,** *98*, 186808.

14. Matsuda, K.; Inoue, T.; Murakami, Y.; Maruyama, S.; Kanemitsu, Y. Exciton Fine Structure in a Single Carbon Nanotube Revealed through Spectral Diffusion. *Phys. Rev. B* **2008,** *77*, 193405.

15. Xue, Y. Q.; Ratner, M. A. Scaling Analysis of Electron Transport through Metal-Semiconducting Carbon Nanotube Interfaces: Evolution from the Molecular Limit to the Bulk Limit. *Phys. Rev. B* **2004,** *70*, 205416.

16. Chen, C. J. *Introduction to Scanning Tunneling Microscopy*; Oxford University Press: New York, 2008.

17. Wildoer, J. W. G.; Venema, L. C.; Rinzler, A. G.; Smalley, R. E.; Dekker, C. Electronic Structure of Atomically Resolved Carbon Nanotubes. *Nature* **1998,** *391*, 59-62.

18. Odom, T. W.; Huang, J. L.; Kim, P.; Lieber, C. M. Atomic Structure and Electronic Properties of Single-Walled Carbon Nanotubes. *Nature* **1998,** *391*, 62-64.

19. Shin, H.-J.; Clair, S.; Kim, Y.; Kawai, M. Substrate-Induced Array of Quantum Dots in a Single-Walled Carbon Nanotube. *Nat. Nanotechnol.* **2009,** *4*, 567-570.

20. Clair, S.; Kim, Y.; Kawai, M. Energy Level Alignment of Single-Wall Carbon Nanotubes on Metal Surfaces. *Phys. Rev. B* **2011,** *83*, 245422.

21. Nazin, G. V.; Qiu, X. H.; Ho, W. Vibrational Spectroscopy of Individual Doping Centers in a Monolayer Organic Crystal. *J. Chem. Phys.* **2005,** *122*, 181105.

22. Nazin, G. V.; Wu, S. W.; Ho, W. Tunneling Rates in Electron Transport through Double-Barrier Molecular Junctions in a Scanning Tunneling Microscope. *Proc. Natl. Acad. Sci. U. S. A.* **2005,** *102*, 8832-8837.

23. Qiu, X. H.; Nazin, G. V.; Ho, W. Vibronic States in Single Molecule Electron Transport. *Phys. Rev. Lett.* **2004,** *92*, 206102.

24. Wu, S. W.; Nazin, G. V.; Chen, X.; Qiu, X. H.; Ho, W. Control of Relative Tunneling Rates in Single Molecule Bipolar Electron Transport. *Phys. Rev. Lett.* **2004,** *93*, 236802.

25. Barbara, P. F.; Meyer, T. J.; Ratner, M. A. Contemporary Issues in Electron Transfer Research. *J. Phys. Chem.* **1996,** *100*, 13148-13168.

26. Park, H.; Park, J.; Lim, A. K. L.; Anderson, E. H.; Alivisatos, A. P.; McEuen, P. L. Nanomechanical Oscillations in a Single-C_{60} Transistor. *Nature* **2000,** *407*, 57-60.

27. Lee, J.; Perdue, S. M.; Perez, A. R.; Apkarian, V. A. Vibronic Motion with Joint Angstrom-Femtosecond Resolution Observed through Fano Progressions Recorded within One Molecule. *ACS Nano* **2014,** *8*, 54-63.

28. Lee, J.; Perdue, S. M.; Perez, A. R.; El-Khoury, P. Z.; Honkala, K.; Apkarian, V. A. Orbiting Orbitals: Visualization of Vibronic Motion at a Conical Intersection. *J. Phys. Chem. A* **2013,** *117*, 11655-11664.

29. Harigaya, K.; Fujita, M. Dimerization Structures of Metallic and Semiconducting Fullerene Tubules. *Phys. Rev. B* **1993,** *47*, 16563-16569.

30. Matsuo, Y.; Tahara, K.; Nakamura, E. Theoretical Studies on Structures and Aromaticity of Finite-Length Armchair Carbon Nanotubes. *Org. Lett.* **2003,** *5*, 3181-3184.

31. Yumura, T.; Nozaki, D.; Bandow, S.; Yoshizawa, K.; Iijima, S. End-Cap Effects on Vibrational Structures of Finite-Length Carbon Nanotubes. *J. Am. Chem. Soc.* **2005,** *127*, 11769-11776.

32. Martín-Martínez, F. J.; Melchor, S.; Dobado, J. A. Clar–Kekulé Structuring in Armchair Carbon Nanotubes. *Org. Lett.* **2008,** *10*, 1991-1994.

33. Hiberty, P. C.; Shaik, S. The Distortive Tendencies of p Electronic Systems, Their Relationship to Isoelectronic s Bonded Analogs, and Observables: A Description Free of the Classical Paradoxes. *Phys. Chem. Chem. Phys.* **2004,** *6*, 224-231.

34. Kertesz, M.; Choi, C. H.; Yang, S. J. Conjugated Polymers and Aromaticity. *Chem. Rev.* **2005,** *105*, 3448-3481.

35. Zhou, Z. Y.; Steigerwald, M.; Hybertsen, M.; Brus, L.; Friesner, R. A. Electronic Structure of Tubular Aromatic Molecules Derived from the Metallic (5,5) Armchair Single Wall Carbon Nanotube. *J. Am. Chem. Soc.* **2004,** *126*, 3597-3607.

36. Tretiak, S.; Kilina, S.; Piryatinski, A.; Saxena, A.; Martin, R. L.; Bishop, A. R. Excitons and Peierls Distortion in Conjugated Carbon Nanotubes. *Nano Lett.* **2007,** *7*, 86-92.

37. Dresselhaus, M. S.; Eklund, P. C. Phonons in Carbon Nanotubes. *Adv. Phys.* **2000,** *49*, 705-814.

38. LeRoy, B. J.; Lemay, S. G.; Kong, J.; Dekker, C. Electrical Generation and Absorption of Phonons in Carbon Nanotubes. *Nature* **2004,** *432*, 371-374.

39. Albrecht, P. M.; Lyding, J. W. Ultrahigh-Vacuum Scanning Tunneling Microscopy and Spectroscopy of Single-Walled Carbon Nanotubes on Hydrogen-Passivated Si(100) Surfaces. *Appl. Phys. Lett.* **2003,** *83*, 5029-5031.

40. Clair, S.; Rabot, C.; Kim, Y.; Kawai, M. Adsorption Mechanism of Aligned Single Wall Carbon Nanotubes at Well Defined Metal Surfaces. *J. of Vac. Sci. Technol. B* **2007,** *25*, 1143-1146.

Chapter V

1. Kershaw, S. V.; Susha, A. S.; Rogach, A. L. Narrow Bandgap Colloidal Metal Chalcogenide Quantum Dots: Synthetic Methods, Heterostructures, Assemblies, Electronic and Infrared Optical Properties. *Chem. Soc. Rev.* **2013,** *42* (7), 3033-3087.

2. Tang, J. A.; Sargent, E. H. Infrared Colloidal Quantum Dots for Photovoltaics: Fundamentals and Recent Progress. *Adv. Mater.* **2011,** *23* (1), 12-29.

3. Nozik, A. J. Spectroscopy and Hot Electron Relaxation Dynamics in Semiconductor Quantum Wells and Quantum Dots. *Annu. Rev. Phys. Chem.* **2001,** *52*, 193-231.

4. Nozik, A. J. Quantum Dot Solar Cells. *Physica E* **2002,** *14* (1-2), 115-120.

5. Beard, M. C.; Ellingson, R. J. Multiple Exciton Generation in Semiconductor Nanocrystals: Toward Efficient Solar Energy Conversion. *Laser Photon. Rev.* **2008,** *2* (5), 377-399.

6. Beard, M. C.; Midgett, A. G.; Hanna, M. C.; Luther, J. M.; Hughes, B. K.; Nozik, A. J. Comparing Multiple Exciton Generation in Quantum Dots To Impact Ionization in Bulk Semiconductors: Implications for Enhancement of Solar Energy Conversion. *Nano Lett.* **2010,** *10* (8), 3019-3027.

7. Sandeep, C. S. S.; Cate, S. t.; Schins, J. M.; Savenije, T. J.; Liu, Y.; Law, M.; Kinge, S.; Houtepen, A. J.; Siebbeles, L. D. A. High Charge-Carrier Mobility Enables Exploitation of Carrier Multiplication in Quantum-Dot Films. *Nat. Commun.* **2013,** *4*, 2360.

8. Tisdale, W. A.; Williams, K. J.; Timp, B. A.; Norris, D. J.; Aydil, E. S.; Zhu, X. Y. Hot-Electron Transfer from Semiconductor Nanocrystals. *Science* **2010,** *328* (5985), 1543-1547.

9. Shockley, W.; Queisser, H. J. Detailed Balance Limit of Efficiency of P-N Junction Solar Cells. *J. Appl. Phys.* **1961,** *32* (3), 510-519.

10. Chuang, C.-H. M.; Brown, P. R.; Bulović, V.; Bawendi, M. G. Improved Performance and Stability in Quantum Dot Solar Cells through Band Alignment Engineering. *Nat. Mater.* **2014,** *13* (8), 796-801.

11. Ning, Z. J.; Voznyy, O.; Pan, J.; Hoogland, S.; Adinolfi, V.; Xu, J. X.; Li, M.; Kirmani, A. R.; Sun, J. P.; Minor, J.; Kemp, K. W.; Dong, H. P.; Rollny, L.; Labelle, A.; Carey, G.; Sutherland, B.; Hill, I.; Amassian, A.; Liu, H.; Tang, J.; Bakr, O. M.; Sargent, E. H. Air-Stable N-Type Colloidal Quantum Dot Solids. *Nat. Mater.* **2014,** *13* (8), 822-828.

12. Ip, A. H.; Thon, S. M.; Hoogland, S.; Voznyy, O.; Zhitomirsky, D.; Debnath, R.; Levina, L.; Rollny, L. R.; Carey, G. H.; Fischer, A.; Kemp, K. W.; Kramer, I. J.; Ning, Z.; Labelle, A. J.; Chou, K. W.; Amassian, A.; Sargent, E. H. Hybrid Passivated Colloidal Quantum Dot Solids. *Nat. Nanotechnol.* **2012,** *7* (9), 577-582.

13. Fernee, M. J.; Thomsen, E.; Jensen, P.; Rubinsztein-Dunlop, H. Highly Efficient Luminescence from a Hybrid State Found in Strongly Quantum Confined PbS Nanocrystals. *Nanotechnology* **2006,** *17* (4), 956-962.

14. Gao, J.; Johnson, J. C. Charge Trapping in Bright and Dark States of Coupled PbS Quantum Dot Films. *ACS Nano* **2012,** *6* (4), 3292-3303.

15. Tang, J.; Kemp, K. W.; Hoogland, S.; Jeong, K. S.; Liu, H.; Levina, L.; Furukawa, M.; Wang, X.; Debnath, R.; Cha, D.; Chou, K. W.; Fischer, A.; Amassian, A.; Asbury, J. B.; Sargent, E. H. Colloidal-Quantum-Dot Photovoltaics Using Atomic-Ligand Passivation. *Nat. Mater.* **2011,** *10* (10), 765-771.

16. Hughes, B. K.; Ruddy, D. A.; Blackburn, J. L.; Smith, D. K.; Bergren, M. R.; Nozik, A. J.; Johnson, J. C.; Beard, M. C. Control of PbSe Quantum Dot Surface Chemistry and Photophysics Using an Alkylselenide Ligand. *ACS Nano* **2012,** *6* (6), 5498-5506.

17. Kovalenko, M. V.; Scheele, M.; Talapin, D. V. Colloidal Nanocrystals with Molecular Metal Chalcogenide Surface Ligands. *Science* **2009,** *324* (5933), 1417-1420.

18. Luther, J. M.; Law, M.; Song, Q.; Perkins, C. L.; Beard, M. C.; Nozik, A. J. Structural, Optical and Electrical Properties of Self-Assembled Films of PbSe Nanocrystals Treated with 1,2-Ethanedithiol. *ACS Nano* **2008,** *2* (2), 271-280.

19. Bozyigit, D.; Volk, S.; Yarema, O.; Wood, V. Quantification of Deep Traps in Nanocrystal Solids, Their Electronic Properties, and Their Influence on Device Behavior. *Nano Lett.* **2013,** *13* (11), 5284-5288.

20. Diaconescu, B.; Padilha, L. A.; Nagpal, P.; Swartzentruber, B. S.; Klimov, V. I. Measurement of Electronic States of PbS Nanocrystal Quantum Dots Using Scanning Tunneling Spectroscopy: The Role of Parity Selection Rules in Optical Absorption. *Phys. Rev. Lett.* **2013,** *110* (12), 127406.

21. Nagpal, P.; Klimov, V. I. Role of Mid-Gap States in Charge Transport and Photoconductivity in Semiconductor Nanocrystal Films. *Nat. Commun.* **2011,** *2,* 486.

22. Kilina, S. V.; Craig, C. F.; Kilin, D. S.; Prezhdo, O. V. Ab Initio Time-Domain Study of Phonon-Assisted Relaxation of Charge Carriers in a PbSe Quantum Dot. *J. Phys. Chem. C* **2007,** *111* (12), 4871-4878.

23. Kilina, S. V.; Kilin, D. S.; Prezhdo, O. V. Breaking the Phonon Bottleneck in PbSe and CdSe Quantum Dots: Time-Domain Density Functional Theory of Charge Carrier Relaxation. *ACS Nano* **2008,** *3* (1), 93-99.

24. Kaushik, A. P.; Lukose, B.; Clancy, P. The Role of Shape on Electronic Structure and Charge Transport in Faceted PbSe Nanocrystals. *ACS Nano* **2014,** *8* (3), 2302-2317.

25. Hetsch, F.; Zhao, N.; Kershaw, S. V.; Rogach, A. L. Quantum Dot Field Effect Transistors. *Mater. Today* **2013,** *16* (9), 312-325.

26. Chen, C. J. *Introduction to Scanning Tunneling Microscopy*. Second Edition ed.; Oxford University Press New York, U.S.A., 2008.

27. Sun, Z. X.; Swart, I.; Delerue, C.; Vanmaekelbergh, D.; Liljeroth, P. Orbital and Charge-Resolved Polaron States in CdSe Dots and Rods Probed by Scanning Tunneling Spectroscopy. *Phys. Rev. Lett.* **2009,** *102* (19), 196401.

28. Krauss, T. D.; Wise, F. W.; Tanner, D. B. Observation of Coupled Vibrational Modes of a Semiconductor Nanocrystal. *Phys. Rev. Lett.* **1996,** *76* (8), 1376-1379.

29. Overgaag, K.; Vanmaekelbergh, D.; Liljeroth, P.; Mahieu, G.; Grandidier, B.; Delerue, C.; Allan, G. Electron-Phonon Coupling and Intervalley Splitting Determine the Linewidth of Single-Electron Transport through PbSe Nanocrystals. *J. Chem. Phys.* **2009,** *131* (22), 224510.

30. Hens, Z.; Vanmaekelbergh, D.; Stoffels, E.; van Kempen, H. Effects of Crystal Shape on the Energy Levels of Zero-Dimensional PbS Quantum Dots. *Phys. Rev. Lett.* **2002,** *88* (23), 236803.

31. van Huis, M. A.; Kunneman, L. T.; Overgaag, K.; Xu, Q.; Pandraud, G.; Zandbergen, H. W.; Vanmaekelbergh, D. Low-Temperature Nanocrystal Unification through Rotations and Relaxations Probed by in Situ Transmission Electron Microscopy. *Nano Lett.* **2008,** *8* (11), 3959-3963.

32. Baik, S. J.; Kim, K.; Lim, K. S.; Jung, S.; Park, Y.-C.; Han, D. G.; Lim, S.; Yoo, S.; Jeong, S. Low-Temperature Annealing for Highly Conductive Lead Chalcogenide Quantum Dot Solids. *J. Phys. Chem. C* **2011,** *115* (3), 607-612.

33. Eggleston, C. M.; Hochella, M. F. Scanning Tunneling Microscopy of Sulfide Surfaces. *Geochim. Cosmochim. Acta* **1990,** *54* (5), 1511-1517.

34. Nazin, G. V.; Wu, S. W.; Ho, W. Tunneling Rates in Electron Transport through Double-Barrier Molecular Junctions in a Scanning Tunneling Microscope. *Proc. Natl. Acad. Sci. U. S. A.* **2005,** *102* (25), 8832-8837.

35. Nazin, G. V.; Qiu, X. H.; Ho, W. Vibrational Spectroscopy of Individual Doping Centers in a Monolayer Organic Crystal. *J. Chem. Phys.* **2005,** *122* (18), 181105.

36. Nguyen, T. H.; Habinshuti, J.; Justo, Y.; Gomes, R.; Mahieu, G.; Godey, S.; Nys, J. P.; Carrillo, S.; Hens, Z.; Robbe, O.; Turrell, S.; Grandidier, B. Charge Carrier Identification in Tunneling Spectroscopy of Core-Shell Nanocrystals. *Phys. Rev. B* **2011,** *84* (19), 195133.

37. Kim, D.; Kim, D.-H.; Lee, J.-H.; Grossman, J. C. Impact of Stoichiometry on the Electronic Structure of PbS Quantum Dots. *Phys. Rev. Lett.* **2013,** *110* (19), 196802.

38. Becker, U.; Rosso, K. M. Step Edges on Galena (100): Probing the Basis for Defect Driven Surface Reactivity at the Atomic Scale. *Am. Mineral.* **2001,** *86* (7-8), 862-870.

39. Moreels, I.; Lambert, K.; Smeets, D.; De Muynck, D.; Nollet, T.; Martins, J. C.; Vanhaecke, F.; Vantomme, A.; Delerue, C.; Allan, G.; Hens, Z. Size-Dependent Optical Properties of Colloidal PbS Quantum Dots. *ACS Nano* **2009,** *3* (10), 3023-3030.

40. Moreels, I.; Justo, Y.; De Geyter, B.; Haustraete, K.; Martins, J. C.; Hens, Z. Size-Tunable, Bright, and Stable PbS Quantum Dots: A Surface Chemistry Study. *ACS Nano* **2011,** *5* (3), 2004-2012.

41. Nilius, N.; Wallis, T. M.; Ho, W. Development of One-Dimensional Band Structure in Artificial Gold Chains. *Science* **2002,** *297* (5588), 1853-1856.

42. Folsch, S.; Hyldgaard, P.; Koch, R.; Ploog, K. H. Quantum Confinement in Monatomic Cu Chains on Cu(111). *Phys. Rev. Lett.* **2004,** *92* (5), 056803.

43. Fölsch, S.; Yang, J.; Nacci, C.; Kanisawa, K. Atom-By-Atom Quantum State Control in Adatom Chains on a Semiconductor. *Phys. Rev. Lett.* **2009,** *103* (9), 096104.

44. Fang, C.; van Huis, M. A.; Vanmaekelbergh, D.; Zandbergen, H. W. Energetics of Polar and Nonpolar Facets of PbSe Nanocrystals from Theory and Experiment. *ACS Nano* **2009,** *4* (1), 211-218.

45. Hackley, J. D.; Kislitsyn, D. A.; Beaman, D. K.; Ulrich, S.; Nazin, G. V. High-Stability Cryogenic Scanning Tunneling Microscope Based on a Closed-Cycle Cryostat. *Rev. Sci. Instrum.* **2014,** *85* (10), 103704.

46. Horcas, I.; Fernández, R.; Gómez-Rodríguez, J. M.; Colchero, J.; Gómez-Herrero, J.; Baro, A. M. WSXM: A Software for Scanning Probe Microscopy and a Tool for Nanotechnology. *Rev. Sci. Instrum.* **2007,** *78* (1), 2432410.

Appendix A

1. Clair, S.; Kim, Y.; Kawai, M. Energy Level Alignment of Single-Wall Carbon Nanotubes on Metal Surfaces. *Phys. Rev. B* **2011,** *83*, 245422.

2. Shin, H.-J.; Clair, S.; Kim, Y.; Kawai, M. Substrate-Induced Array of Quantum Dots in a Single-Walled Carbon Nanotube. *Nat. Nanotechnol.* **2009,** *4*, 567-570.

3. Nazin, G. V.; Wu, S. W.; Ho, W. Tunneling Rates in Electron Transport through Double-Barrier Molecular Junctions in a Scanning Tunneling Microscope. *Proc. Natl. Acad. Sci. U. S. A.* **2005,** *102*, 8832-8837.

Appendix B

1. Nazin, G. V.; Wu, S. W.; Ho, W. Tunneling Rates in Electron Transport through Double-Barrier Molecular Junctions in a Scanning Tunneling Microscope. *Proc. Natl. Acad. Sci.* U. S. A. **2005**, 102, 8832-8837.

2. Wu, S. W.; Nazin, G. V.; Chen, X.; Qiu, X. H.; Ho, W. Control of Relative Tunneling Rates in Single Molecule Bipolar Electron Transport. *Phys. Rev. Lett.* **2004**, 93, 236802.

3. Nazin, G. V.; Qiu, X. H.; Ho, W. Vibrational Spectroscopy of Individual Doping Centers in a Monolayer Organic Crystal. *J. Chem. Phys.* **2005**, 122, 181105.

4. Hines, M. A.; Scholes, G. D. Colloidal PbS Nanocrystals with Size-Tunable Near-Infrared Emission: Observation of Post-Synthesis Self-Narrowing of the Particle Size Distribution. *Adv. Mater.* **2003**, 15 (21), 1844-1849.

5. Moreels, I.; Lambert, K.; Smeets, D.; De Muynck, D.; Nollet, T.; Martins, J. C.; Vanhaecke, F.; Vantomme, A.; Delerue, C.; Allen, G.; Hens, Z. Size-Dependent Optical Properties of Colloidal PbS Quantum Dots. *ACS Nano*, **2009**, 3 (10), 3023–3030